博士論文

Silver phosphate microcrystalline film-based photoanodes for photoelectrochemical water oxidation

（微結晶リン酸銀膜光電極を用いた水の酸化反応）

曹　祺

Silver phosphate microcrystalline film-based photoanodes for photoelectrochemical water oxidation

（微結晶リン酸銀膜光電極を用いた水の酸化反応）

曹　　祺

Cao　　Qi

Department of Mechanical Engineering

The University of Tokyo

Supervised by: Assoc. Prof. Dr. Jean-Jacques Delaunay

August 2018

Abstract

Since the first report of electrochemical photolysis of water using a TiO_2 electrode under ultraviolet light irradiation, photoelectrochemical (PEC) water splitting process has captivated tremendous research interest as a promising technology for sustainable production of the clean energy carrier – H_2, from solar light and water. The advances in PEC technology substantially depend on the development of highly stable and efficient photoelectrodes, especially photoanodes, since the oxygen evolution reaction (OER, *i.e.* water oxidation) happening on the anode is usually more thermodynamically complex and dynamically sluggish than hydrogen evolution reaction (HER, *i.e.* water reduction) happening on the cathode. The photoanode allowing the occurrence of water oxidation is thus more dominant for development of overall water splitting technology. Traditional TiO_2-based electrodes usually suffer a lot from the low visible-light absorption induced by their large bandgaps. Meanwhile, sulfides and (oxy)nitrides show poor stability over long-term operation in actual conditions. These have highlighted WO_3, $BiVO_4$, α-Fe_2O_3, and Ag_3PO_4 as novel alternatives to the above-mentioned photoanode materials towards efficient and stable water oxidation. In 2010, as an important benchmark report, Yi *et al.* demonstrated that Ag_3PO_4 as the photoanode material, with the presence of $AgNO_3$ in electrolyte as an electron scavenger, could offer much higher photocatalytic activity for water oxidation than other well-established anodic catalysts including $BiVO_4$ and WO_3. This superior performance could be further improved through the strategies like facet and morphology engineering. However, till now still not much work has been reported on using Ag_3PO_4 as the photoanode material for PEC water splitting due to the difficulty in fabrication of highly adhesive Ag_3PO_4 layers on conductive substrates as membrane

photoanodes. More importantly, the two major intrinsic shortcomings of Ag_3PO_4, *i.e.* the poor structural stability and low bandgap absorption resulted from the native defects of silver vacancy (V_{Ag}), silver interstitial (Ag_i), and simultaneously decomposition-induced precipitation of Ag^0 nanoparticles (NPs) on the surface, have together limited its further usage as photoanode materials for PEC water oxidation.

In this thesis, solution-processed large-area (4.5 × 4.5 cm^2) Ag_3PO_4 microcrystalline films are first prepared *via* a room-temperature, air-exposed immersion reaction. The multiple effects of the native defects in Ag_3PO_4, *i.e.* V_{Ag}, Ag_i, and surface precipitation of Ag^0 NPs, are first demonstrated experimentally. By changing the addition amount of the oxidation agent H_2O_2 during the synthetic reaction, Ag_3PO_4 microcrystalline films with different amounts of Ag^0 NPs on the surface are obtained. It is found that despite the favorable superior conductivity and plasmonic effect having improved the interfacial charge transfer and light absorption of the Ag_3PO_4 film photoanode, the defective film with the largest amount of Ag^0 NPs on the surface finally exhibits the lowest current density, due to the disadvantageous effects involving the decreased crystalline quality, easier decomposition of active material of Ag_3PO_4, decreased electrochemical surface area with a high content of Ag^0 NPs covering the surface of Ag_3PO_4, and also serving as the recombination centers. As a result, even the Ag_3PO_4 microcrystalline film which has achieved the highest photocurrent density fails to demonstrate considerable stability. These results have further highlighted the significance of mitigation of native defects of Ag_3PO_4 fundamentally towards enhanced water oxidation stability and efficiency of the microcrystalline film photoanodes.

Typically, the post-treatment of vacuum annealing at different temperatures (*i.e.* 100,

200, 300, 400 and 500 °C) has been investigated as a strategy for solving the problem of native defects and low light absorption of Ag_3PO_4. It is found that below 400 ºC is the |Recovery| stage for Ag_3PO_4 microcrystals when defect amount decreases and therefore crystallinity increases. From 400 ºC, the |Recrystallization| stage and also precipitation of Ag_3PO_4 bulk crystals start, and afterwards till 500 ºC is the |Recrystallization + Grain growth| stage for Ag_3PO_4, when more faceted and larger bulk crystals of Ag_3PO_4 precipitate extensively. In this series of Ag_3PO_4 film photoanodes, the same variation in $[J_{light} - J_{dark}]$ *vs. E* curves is found as the light absorption profiles, *i.e.* 400 ºC > 500 ºC > 300 ºC > 200 ºC > non-annealed > 100 ºC-annealed Ag_3PO_4 film, indicating that light absorption, especially the bandgap absorption could be the dominant factor to the PEC performance. Particularly, much improved PEC water oxidation stability and efficiency of the 400 ºC-annealed Ag_3PO_4 film photoanode are demonstrated compared with the non-annealed Ag_3PO_4 film, suggesting that the methodology of vacuum annealing could be utilized for improving the PEC performance of Ag_3PO_4 film photoanodes because of its ability to mitigate the unfavorable effects of the native defects like V_{Ag}, remove the Ag^0 NPs on the surface, and substantially increase the bandgap light absorption of these Ag_3PO_4 microcrystalline films.

Next, from the viewpoint of advanced structural design, in consideration that the usage of microcrystalline film photoanode might cause the problem of decreased active surface area despite its relatively higher stability than nanocrystalline powder-deposited photoanode, the possibility of introducing porous structures into these microcrystalline Ag_3PO_4 film photoanodes is also investigated towards further improved photoactivity and stability. Particularly, it is demonstrated that the porous degree of the as-obtained Ag_3PO_4 films could be tuned by changing the reaction time from 1 h to 2 h, 5 h, 9 h, 20

h and 24 h, with the usage of specific reaction parameters. These porous Ag_3PO_4 films, in spite of having left the native defects not recovered and Ag^0 NPs on the surface not removed, finally could demonstrate improved surface areas and light absorption, owing to which improved PEC performance has also been achieved. Specifically, the optimal highly porous 20-h Ag_3PO_4 microcrystalline film photoanode shows superior water oxidation efficiency with a photocurrent density of 4.32 mA/cm^2 which is almost three times higher than that of non-porous 1-h Ag_3PO_4 microcrystalline film (1.48 mA/cm^2) at 1.0 V *vs.* Ag/AgCl. This value of photocurrent density is also higher than that of the 400 °C-annealed non-porous Ag_3PO_4 film photoanode.

Overall, it could be concluded that: a) The instability of the Ag_3PO_4 microcrystalline films is originated from the native defects involving V_{Ag} and Ag^0 NPs precipitated on the surface, thus the methodology of vacuum annealing, typically at 400 °C, turns out to be more favorable for improving the stability because it can fundamentally solve, or at least mitigate the various problems induced by native defects; b) Light absorption is a crucial factor to the PEC performance, whereas the surface area which would largely determine the final process of PEC water oxidation, *i.e.* the surface redox reaction is also important, thus the porous Ag_3PO_4 microcrystalline film photoanodes can achieve even higher efficiency in spite of leaving the defect and absorption issues not solved; c) Trying to make a combination of these two techniques, *i.e.* taking both the fundamental properties of the material (*e.g.*, defects and absorption) and the advanced structural design (*e.g.*, larger surface area) into concern, may provide further possibility towards more stable and efficient Ag_3PO_4 film photoanodes for PEC water oxidation.

Contents

1. Introduction

1.1. Photoelectrochemical water splitting

Since the first report of electrochemical photolysis of water at a TiO_2 electrode under ultraviolet light irradiation,[1] photoelectrochemical (PEC) water splitting has attracted tremendous research interest as a promising technology for sustainable production of clean energy carrier – hydrogen, from solar light and water.[2] Generally speaking, one PEC cell should be composed of three major parts, which are the working electrode, the counter electrode and the electrolyte solution, respectively. One common approach is to utilize the specific semiconductor with desirable photoactivity as the working electrode, for efficient production of photo-excited electron–hole pairs (*i.e.* the photoelectrons and photoholes). In such a traditional system, the oxidation of water (*i.e.* the oxygen evolution reaction, OER) will happen on the surface of the photoanode. Meanwhile, the reduction of water (*i.e.* the hydrogen evolution reaction, HER) will accordingly happen on the surface of the photocathode with the assistance of external bias and under simultaneous light irradiation.[3] Typically, when the semiconducting photoelectrode has been immersed into the electrolyte solution, the process of charge transfer will be happening across the as-formed semiconductor–electrolyte junction (SEJ) in order to keep the electrostatic equilibrium of the PEC system. Consequently, after such an electrostatic equilibrium has been established, the Fermi level (E_F) of the electrons (*i.e.* photoelectrons) of the semiconductor, as well as the redox potential of the electrolyte solution, will be aligned at the as-formed SEJ interface. This will afterwards result in an upward bending of the electronic band in the *p*-type semiconductor for a

p-type SEJ, and accordingly a downward bending of the electronic band in the *n*-type semiconductor for an *n*-type SEJ. In fact, this charge transfer process will lead to the removal of majority charge carriers within a characteristic region near the surface of the semiconductor, termed as depletion layer, where a built-in electric field is generated and therefore the "bending of the electronic band" will takes place. Typically in a PEC cell, depletion layer-induced band bending could reversely help the transfer and separation of photogenerated charge carriers. Hence in this regard, it is of great importance to understand such band bending in PEC process to achieve optimized PEC performance. Typically, the band bending phenomenon is usually generated from the surface states of semiconductors as well as the metal–semiconductor contact (*i.e.* ohmic contact). Particularly in PEC process, the applied bias (V_{app}) and electrolyte molecules absorption will also lead to the occurrence of band bending.[4]

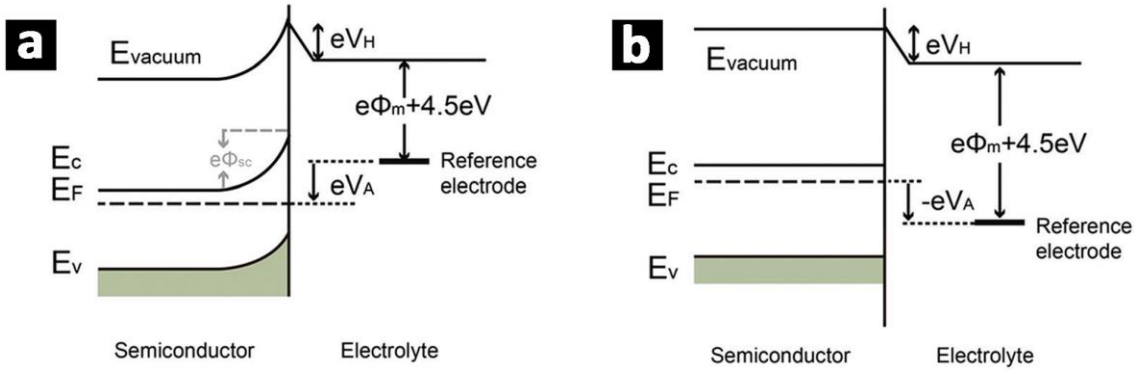

Figure 1.1. Effect of V_{app} (V_A in the figure) on an *n*-type semiconductor photoelectrode. Φ_M is the work function of the metal. Φ_{SC} is the potential drop across the depletion layer. Reproduced with the permission from Ref. 4.

The surface of the semiconducting photoelectrode will absorb the molecules in the electrolyte solution upon contacting each other. The conduction band (CB) of acceptor molecules will consequently shift downwards until equilibrium is established, resulting

in the electron transfer from the semiconductor to absorbed molecules. This will cause the formation of a Helmholtz layer, which is the region between the absorbed ions on the semiconductor surface and closest ions in electrolyte. The potential drop across the Helmholtz layer (V_H) changes by –59 mV per unit pH at 25 °C.[5] Meanwhile, the band bending could also be induced by V_{app} between the semiconductor working electrode and reference electrode. The difference in the potential would be distributed over both the depletion layer and Helmholtz layer. Further, since V_H is constant, any change in the V_{app} will have an influence on the depletion layer. For instance, a positive V_{app} applied on *n*-type semiconductor will lead to an increase in the depletion layer (*i.e.* upward band bending, Figure 1.1a), whereas the band bending degree will be reduced if a negative V_{app} has been applied (Figure 1.1b). In contrast, a negative V_{app} is needed for increasing the depletion layer of a *p*-type semiconductor and a positive V_{app} is needed for reducing the depletion layer.[4]

If an *n*-type semiconductor is immersed into an electrolyte solution which contains H_2O/O_2 redox couples, as has been discussed above, the charge transfer occurs across the SEJ interface until electrostatic equilibration. Then the semiconductor electrode will have an excess of positive charge distributed over the depletion layer, and the electrolyte will have an excess of negative charge distributed over Helmholtz layer. Further, the light irradiation will bring about large quantities of non-equilibrium photogenerated charge carriers, resulting in a built-in electric field near the semiconductor surface, and thus the generation of the photovoltage (*i.e.* open-circuit voltage, V_{OC}). The maximum current generated in this electric field is termed as the short circuit current (J_{SC}). Thus the maximum power point $P_{PA} = V_{OC} \times J_{SC}$. An overall energy diagram of the SEJ of an *n*-type semiconductor is shown in Figure 1.2.[6] Briefly, given that the doped *n*-type

semiconductor has a uniform distribution of donor ions N_D that are balanced by the same quantity of free electrons $n_0 = N_D$ in the neutral region, where the band edge is flat. The doping amount can be indicated as $\zeta_{nb} = E_{cb} - E_{Fn,b}$ and then we can write $\zeta_{nb} = k_B T \ln(N_c/n_0)$ where N_C is the effective density of states in the CB and $k_B T$ is the thermal energy. The potential in the Helmholtz layer is $V_H = \phi_s - \phi_{el}$. The change in V_H produces the modification of the position of the band edge E_{cs}. The potential V_{sc} is related to the height of the barrier in the semiconductor, that is $V_{sc} = \phi_b - \phi_s$, where ϕ_b is the electrostatic potential in semiconductor neutral region, and ϕ_s is the potential at the semiconductor surface. The measured voltage can be expressed as $V_r = (E_0 + \chi + \zeta_{nb})/q + V_{sc} + V_H$. The CB edge at position x in the semiconductor is modified by the local electrostatic potential $E_c(x) = -\chi - q[\phi(x) - \phi_{el}]$. The energy of the CB edge at the surface is $E_{cs} = -\chi - qV_H$. The potential of the CB edge V_{cs} is determined by the expression $E_{cs} = E_0 - qV_{cs}$, therefore $V_{cs} = (E_0 + \chi)/q + V_H$. Hence, the flatband potential can be formulated as $V_{fb} = (E_0 + \chi + \zeta_{nb})/q + V_H$, or $V_{fb} = V_{cs} - \Delta V_H + \zeta_{nb}/q$, indicating that flatband potential directly correlates with the position of the CB edge.

In many situations, the applied bias V_{app} is of central interest for the analysis of PEC performance of a semiconductor electrode. Given that the applied bias V_{app} with respect to an equilibrium initial situation, only modifies the V_H and the semiconductor barrier height V_{sc}, the V_{app} therefore can be stated as $V_{app} = -(E_{Fn,b} - E_{redox})/q$, $V_{app} = V_r - V_{r0}$ or $V_{app} = \phi_b - \phi_{b0}$. The built-in potential V_{bi} is an equilibrium quantity $V_{bi} = \phi_{b0} - \phi_{s0}$, thus the V_{app} can be consequently stated as $V_{app} = V_{sc} - V_{bi} + (V_H - V_{H0})$. Particularly as in the Figure 1.2, a negative V_{app} must be applied to the semiconductor in equilibrium with the electrolyte in order to flatten the bands (*i.e.* reducing the depletion layer).

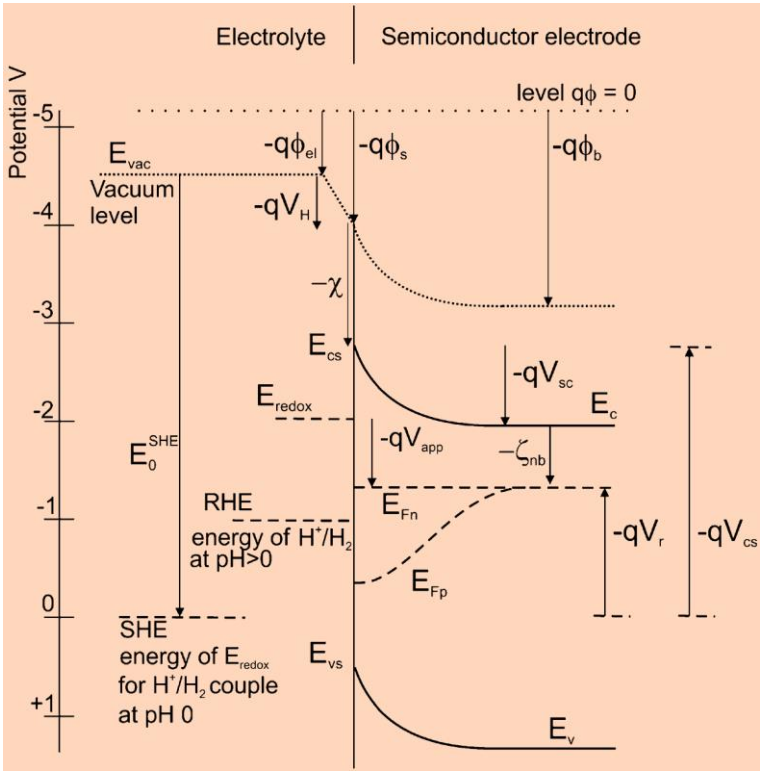

Figure 1.2. The energy diagram of SEJ of an *n*-type semiconductor electrode. V_r is the measured voltage with respect to standard hydrogen electrode (SHE). V_{app} is the applied bias. ϕ is the local electrostatic potential. E_{Fn} is the Fermi level of electrons which is a function of the position. $E_{Fn,b}$ is the Fermi level of electrons at the back contact. E_{Fp} is the Fermi level of holes. E_0 is the energy of SHE (*i.e.* −4.44 eV). E_{redox} is the Fermi level of electrolyte species at redox level. E_c is the energy of CB edge. E_v is the energy of valence band edge. χ is electron affinity. ζ_{nb} is the difference between semiconductor CB energy and the electron Fermi level. V_{sc} is the semiconductor barrier height at depletion layer. V_{cs} is the potential of the CB at semiconductor surface. V_{fb} is the flatband potential, and V_{bi} is the built-in potential. Reproduced with the permission from Ref. 6.

For practical usages, a variety of semiconductors have been investigated for use as cost-effective, highly efficient and stable photoanodes and photocathodes for PEC water

splitting, as summarized in Figure 1.3.[7] Specifically, TiO_2 has been recognized as the favorable light absorber for water splitting towards both HER and OER. Nevertheless, TiO_2 due to its large bandgap of 3.0–3.2 eV, generally could absorb only the ultraviolet light, which is just a small fraction of sunlight energy (3–5%). Sulfides and selenides, on the other hand, suffer a lot from their serious photo-corrosion problem, despite their considerable visible-light absorption capability. Compared with TiO_2, tungsten trioxide (WO_3) possesses a smaller bandgap of 2.4–2.8 eV, making it possible to utilize both the ultraviolet and visible light within the solar spectrum. Nonetheless, WO_3 still displays a low solar energy conversion efficiency because of the relatively low reduction potential for electrons, which determines its quite positive CB position. Besides, hematite (Fe_2O_3) is another well-recognized and widely studied photoanode material attributed to its low cost, high stability, along with superior visible-light absorption. However, despite the tremendous investigations which have been conducted so far on this material, there are still a lot of challenges for further employment of α-Fe_2O_3 towards PEC water oxidation. For example, the flat-band potential of α-Fe_2O_3 is too positive for reduction of hydrogen, and therefore will need a large overpotential for driving the OER to happen. Moreover, the relatively low absorption coefficient and unsatisfactory conductivity for the majority carrier of α-Fe_2O_3 are both unfavorable for the achievement of a superior solar energy conversion efficiency. Hence in this regard, it is still quite challenging for researchers to develop novel photoanode materials of higher solar energy conversion efficiency and better stability towards PEC water oxidation.

1.2. Ag_3PO_4: Photoactivity and drawbacks for PEC water oxidation

The advances in PEC technology substantially rely on the development of highly efficient and stable photoelectrodes, especially photoanodes, considering that the OER happening on photoanodes is usually more complex and dynamically sluggish than the HER happening on the cathodes, and thus is more dominant in the water splitting process: For one thing, the production of one O_2 molecule requires removal of four electrons and two protons from two H_2O molecules, which are twice than those for HER; For another, water oxidation is also an uphill reaction with a positive Gibbs free energy from a thermodynamic standpoint.[8] Traditional TiO_2-based photoanodes suffer a lot from low visible-light absorption induced by the large bandgaps. Meanwhile, sulfides and (oxy)nitrides such as CdS,[9] Ta_3N_5,[10] and TaON[11] demonstrate poor stability over long-term operation in actual conditions. These have highlighted WO_3, $BiVO_4$ and α-Fe_2O_3 as novel alternatives to the above-mentioned photoanode materials towards efficient and stable water oxidation.[3,12–18] The first report of using silver phosphate (Ag_3PO_4) for photocatalytic water oxidation can be traced back to as early as 1988 by Tennakone *et al*..[19] In 2010, as an important benchmark report, Yi *et al.* further demonstrated that Ag_3PO_4 as a photoanode material, with the presence of $AgNO_3$ in electrolyte as an electron scavenger, could display much higher photocatalytic activity for water oxidation than well-recognized visible-light-driven OER catalysts including $BiVO_4$ and WO_3,[20] and this superior performance could be further improved through the strategies like morphology and facet engineering.[21]

Till now, the photocatalytic activity of Ag_3PO_4 for pollutant degradation has been widely investigated and optimized.[22–27] In addition, Ag_3PO_4 is regarded as an ideal

candidate for water photooxidation due to its low toxicity, moderate bandgap with an absorption edge of ~530 nm, highly positive valence band edge position at ~2.85 V *vs.* reversible hydrogen electrode (RHE), which can afford large thermodynamic driving force for photoholes to oxidize water.[28–29]

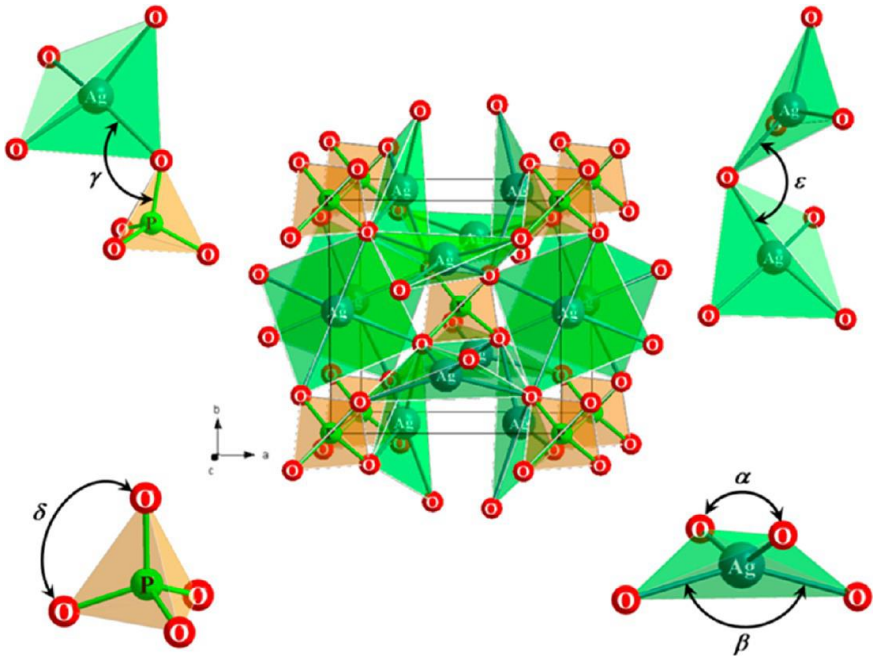

Figure 1.3. Schematic illustration of the Ag_3PO_4 structure, displaying both [AgO_4] and [PO_4] tetrahedral units. Ag_3PO_4 is of BCC structure with the typical lattice parameter of ~6.004 Å, consisting of isolated [PO_4] tetrahedra with the P–O distance of ~1.539 Å, as well as every six Ag^+ distributing among twelve sites of the two-fold symmetry. In the modeled structure, each isolated [PO_4] unit is bonded to three neighboring [AgO_4] units by O atoms, and the existence of two O−Ag−O bond angles (α, β) indicates the [AgO_4] units are highly distorted in the lattice, which is resulted from the inductive effect of the high-electronegativity [PO_4] tetrahedra. Reproduced with the permission from Ref. 30.

In general, the efficiency of PEC water oxidation on the photoanode surface is determined by four fundamental processes: 1) Light absorption (*i.e.* photoexcitation of

charge carriers); 2) Separation of photoexcited electron–hole pairs; 3) Charge migration towards the SEJ interface; 4) Surface redox reaction with water molecules. Particularly for Ag_3PO_4, the fairly higher intrinsic mobility of photoelectrons than photoholes, and the inductive effect of [PO_4] tetrahedron units originated from high electronegativity together facilitate the separation of electron–hole pairs, which provides solid support for its excellent photocatalytic activity.[29] Figure 1.3 presents a schematic illustration of the crystal structure of Ag_3PO_4, where such a unique inductive effect of the [PO_4] units has been discussed.

However, the large numbers of intrinsic point defects [*i.e.* silver vacancy (V_{Ag}) and silver interstitial (Ag_i)] resulted from the high ionic mobility of Ag^+ in silver compounds like Ag_3PO_4 and silver halides will easily trap photogenerated electrons,[30–32] leading to non-negligible precipitation of metallic Ag^0 on the surface. It has been revealed both theoretically and experimentally that such V_{Ag} and Ag_i can exist from room-temperature growth of Ag_3PO_4, and are highly mobile, which is determined by their low formation energy and migration barrier.[33–35] Although this characteristic could be used in some special occasions requiring tunable Ag^+ release for bactericidal activity,[36] it is not good for the photocatalytic or PEC processes because the decomposition of Ag_3PO_4 means the loss of the photoactive semiconductor material, making it unstable during long-time reactions. In addition, the real conditions in PEC water oxidation process (*i.e.* aqueous solution and light irradiation) make it even easier for Ag_3PO_4 to be reduced to Ag^0 due to the high electrode potential of Ag–Ag_3PO_4 (0.45 V *vs.* RHE).[37] Meanwhile, the precipitated Ag^0 sites on the surface, due to their better electron affinity than Ag_3PO_4,[38–39] might easily attract and store electrons, and thereafter become recombination centers for photoholes, lowering the photocurrent density as a result. To

ease this problem, Wu *et al.* incorporated a Ag^0-nanoplate underlayer in their Ag_3PO_4 photoanode to drain the electrons away to the cathode, as shown in Figure 1.4 below.[40] Nevertheless, this couldn't be a fundamental solution since the Ag^0 nanoparticles (NPs) will be continuously precipitated at the Ag_3PO_4/electrolyte interface during long-term OER operation, offsetting such an advantageous draining effect.

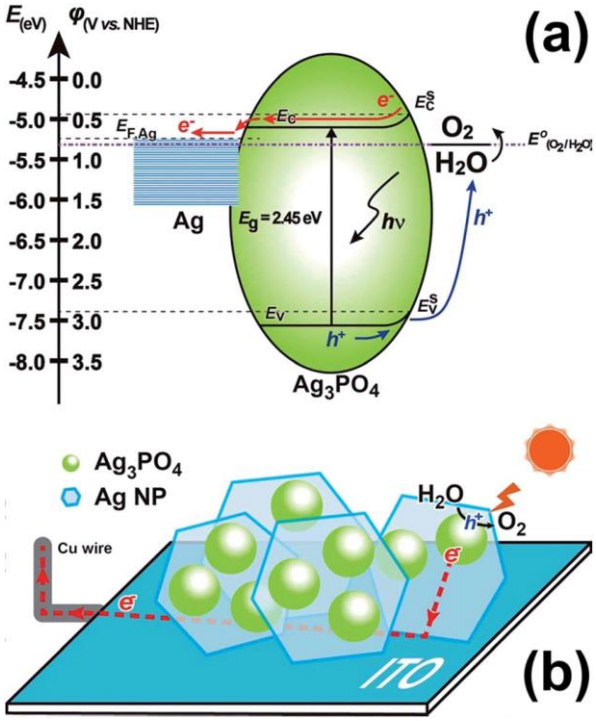

Figure 1.4. Schematic illustrations showing (a) the energy band diagram, as well as (b) the charge-flow direction (*i.e.* draining of photoelectrons) of the Ag–Ag_3PO_4 composite photoanode for PEC water oxidation. Reproduced with the permission from Ref. 40.

Different types of photoelectrodes, at the same time, could have a great influence on the performance, especially the stability. Microcrystalline film photoelectrodes usually demonstrate better structural stability than nanocrystalline powder-deposited electrodes due to the superior anti-aggregation ability and stronger binding force between active material layers and substrates. More importantly, the increased crystallite size leads to

decreased amount of surface defects and dangling bonds, which will easily become self-degradation sites of the active semiconductor materials.[41] Nonetheless, due to the challenges of the poor stability and the difficulties in fabricating Ag_3PO_4 membranes, it is considered to be not easy to obtain highly adhesive Ag_3PO_4 layers on conductive substrates.[42–44] Recently, Cao *et al.* reported direct growth of highly porous Ag_3PO_4 microcrystalline film photoanodes on as-purchased silver foils with large surface areas, which consequently demonstrated enhanced OER stability and efficiency.[45] However, the technical problem of native defects-induced precipitation of Ag^0 NPs on the surface of Ag_3PO_4 was still not solved.

Besides, as another fundamental process determining the PEC conversion efficiency, light absorption of as-reported Ag_3PO_4 photocatalysts is far from satisfactory. Despite its high photoactivity, the bandgap absorbance in the region of ≤ ~530 nm of Ag_3PO_4 powder photocatalyst (fabricated into thick film for measurement) can hardly exceed 0.7 (*i.e.* ≤ 80% absorption of incident light),[34,46–47] which is also much lower than other traditional semiconductors such as $BiVO_4$,[26] WO_3,[48] and Co_3O_4.[49] Specifically for solution-processed Ag_3PO_4 microcrystalline films, although the advantageous highly porous surface structure could help to increase light absorption greatly, the maximum absorption is still below 80% across the ultraviolet–visible region.[45] Overall, despite the arguably highest photoactivity of Ag_3PO_4 among common semiconductors, there are still two big issues, *i.e.* native defects-induced Ag^0 precipitation, and poor bandgap light absorption, which need to be solved for further improvement towards highly stable and efficient photoanodes for PEC water oxidation.

1.3. Experimental demonstration of the multiple effects of Ag^0 NPs

Now that the easy decomposition of Ag_3PO_4 and consequently precipitation of Ag^0 NPs on the surface is a well-recognized but unavoidable problem originated from the intrinsically high ionic mobility of Ag^+ and native defects of V_{Ag} and Ag_i in Ag_3PO_4, as discussed above, it can be meaningful if a more comprehensive understanding could be achieved experimentally, regarding the multiple effects of surface precipitation of Ag^0 NPs on the various physicochemical properties and PEC water oxidation performance of Ag_3PO_4 microcrystalline film photoanodes.

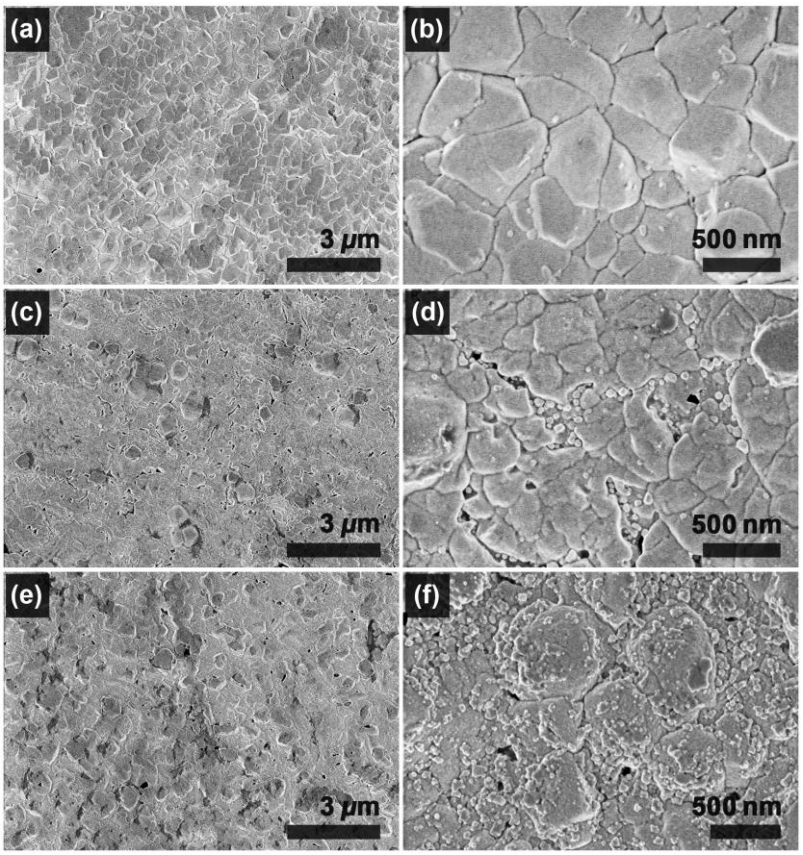

Figure 1.5. SEM images of the Ag_3PO_4 microcrystalline films with different amounts of surface precipitation of Ag^0 NPs: (a–b) very little amount, (c–d) moderate amount, (e–f) large amount, respectively.

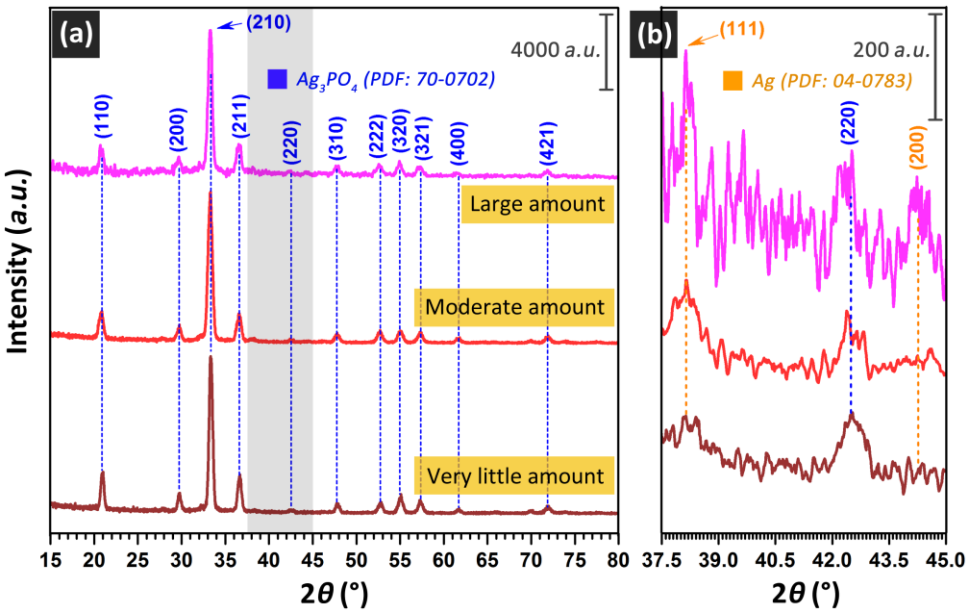

Figure 1.6. Representative XRD patterns of the Ag_3PO_4 films with different amounts of Ag^0 NPs on the surface. Panel (b) is an enlarged view of the region $37.5\ ° \leq 2\theta \leq 45.0\ °$, showing the characteristic diffraction peaks of metallic silver phase.

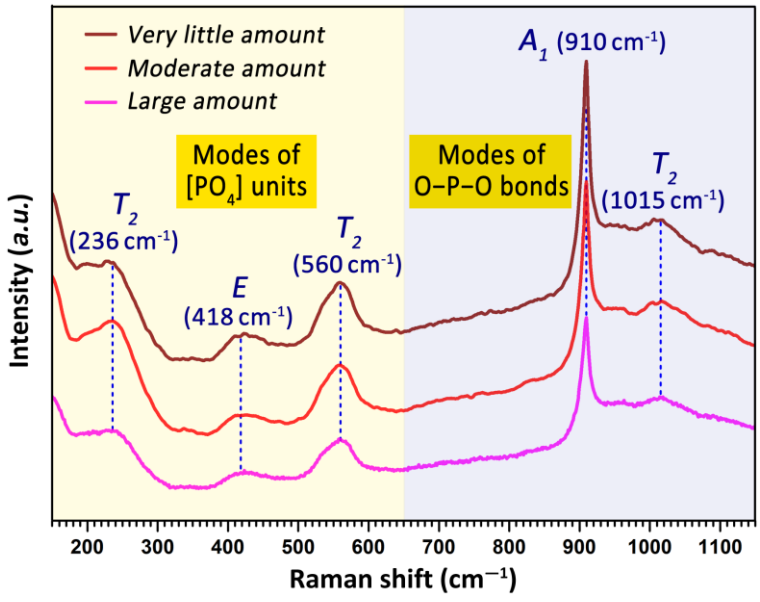

Figure 1.7. Representative Raman spectra of the Ag_3PO_4 films with different amounts of surface precipitation of Ag^0 NPs. The different singly, doubly, and triply degenerate vibrational modes are labelled by A_1, E, and T_2, respectively.

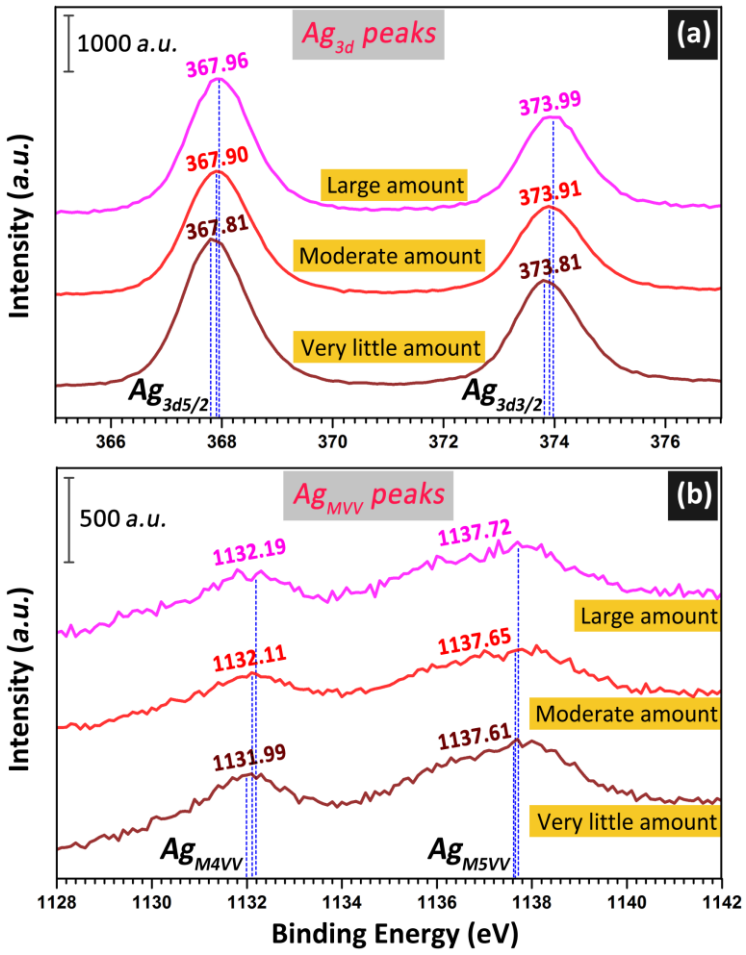

Figure 1.8. Representative high-resolution XPS spectra of the (a) Ag 3d region, and (b) Ag MVV Auger electron region, of the Ag_3PO_4 films with different amounts of surface precipitation of metallic Ag^0 NPs.

Typically, different amounts of metallic Ag^0 precipitation on the surface of Ag_3PO_4 microcrystalline films are intentionally induced by applying different addition amounts of the oxidation agent H_2O_2 during the synthesis experiment. As is shown in Figure 1.5, SEM images demonstrate the different amounts of Ag^0 NPs precipitated on the surface of as-obtained Ag_3PO_4 microcrystalline films, termed as the "very little amount" (Figure 1.5a–b), the "moderate amount" (Figure 1.5c–d), and the "large amount" (Figure 1.5e–f), respectively. The increase in the amount of surface precipitated Ag^0 NPs from the "very

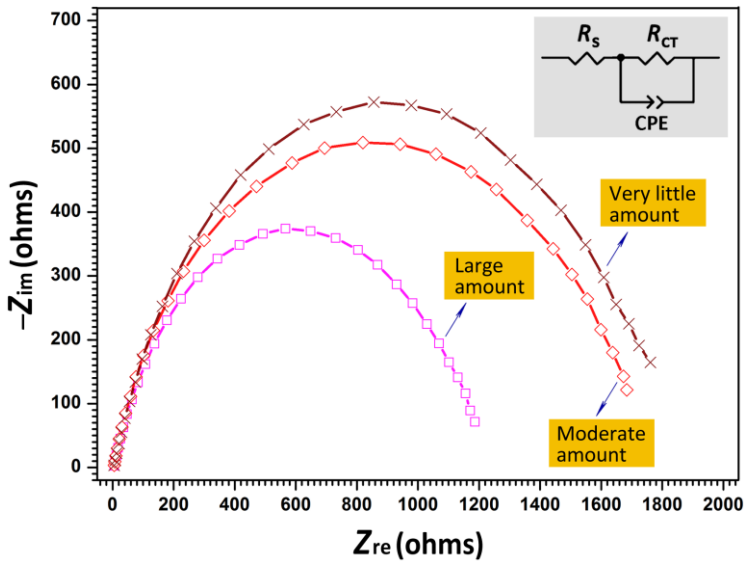

Figure 1.9. EIS Nyquist plots of the Ag_3PO_4 film photoanodes with different amounts of surface precipitation of metallic Ag^0 NPs. The insert displays the equivalent circuit consisting of a serial resistor (R_S), a resistor–capacitor circuit modelling the parallel combination of the interfacial charge transfer resistance (R_{CT}), and constant phase element (CPE) attributed to the SEJ interface.

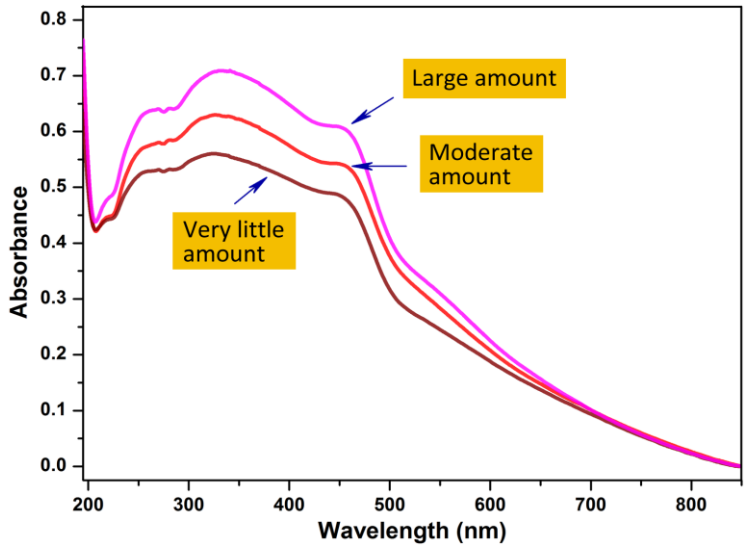

Figure 1.10. Representative diffuse-reflectance spectra (DRS) of the Ag_3PO_4 films with different amounts of surface precipitation of metallic Ag^0 NPs.

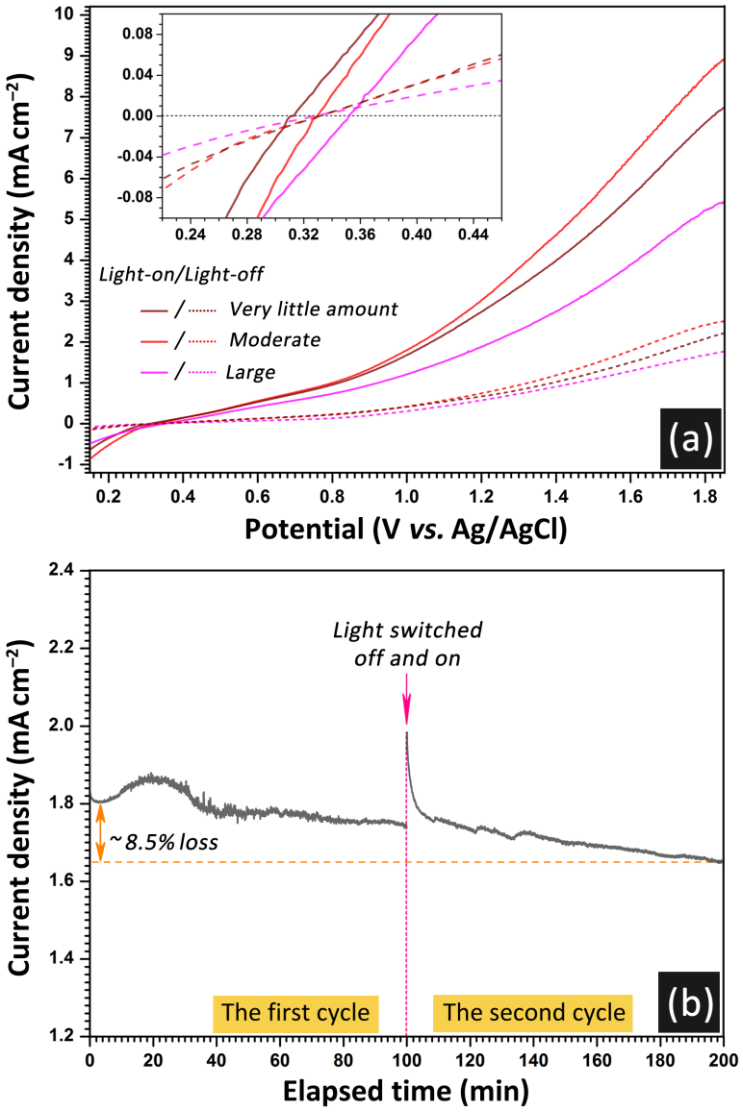

Figure 1.11. PEC water oxidation performance of the Ag_3PO_4 film photoanodes with different amounts of Ag^0 NPs precipitated on the surface: (a) the dependence of current density on applied potential. The solid and dashed lines stand for the photocurrent and dark current densities of each photoanode, respectively. Inset shows an enlarged view of the potential range from 0.22 to 0.46 V *vs.* Ag/AgCl. (b) The current density−time (*J*−*t*) curve of the photoanode fabricated from the Ag_3PO_4 film with the "moderate amount" of Ag^0 NPs on the surface during the stability test at an applied potential of 1.0 V *vs.* Ag/AgCl.

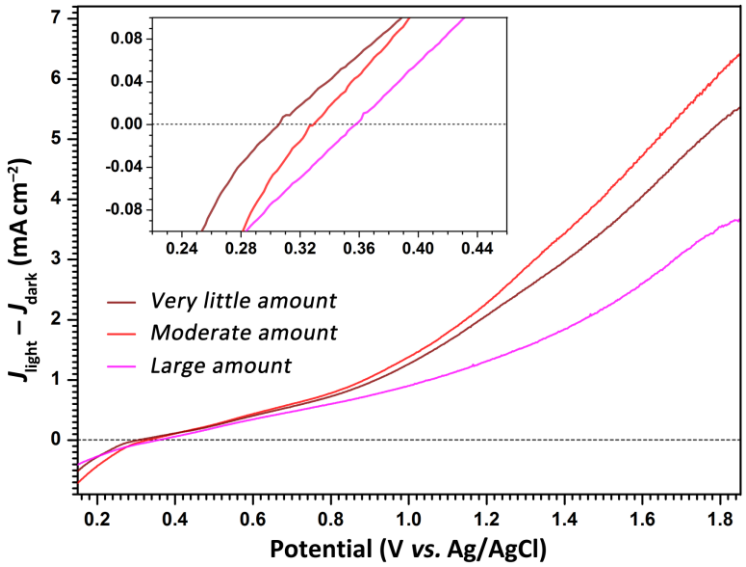

Figure 1.12. The dependence of photocurrent density minus dark current density ($J_{light} - J_{dark}$) on applied potential of the Ag_3PO_4 film photoanodes with different amounts of Ag^0 NPs precipitated on the surface. Inset shows an enlarged view of the potential range from 0.22 to 0.46 V *vs.* Ag/AgCl.

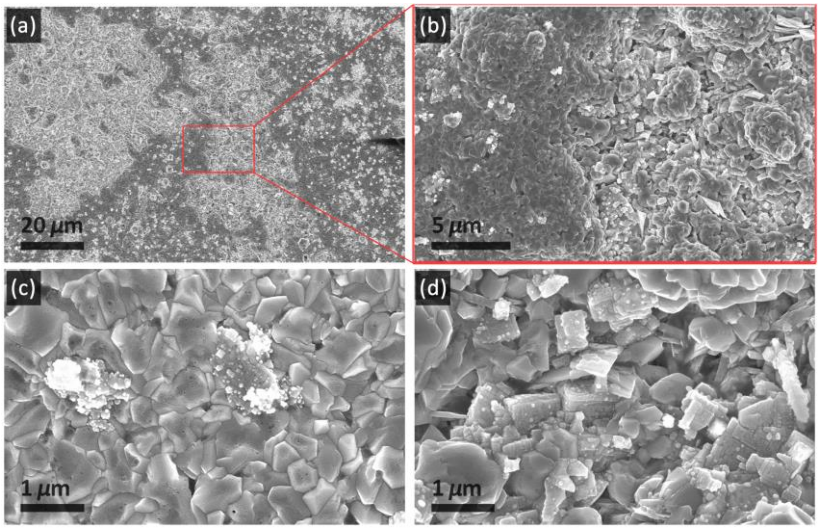

Figure 1.13. SEM images exhibiting the surface morphology after the stability test of the photoanode fabricated from the Ag_3PO_4 film with "moderate amount" of Ag^0 NPs precipitated on the surface: (a) overall morphology; (b) the interfacial area of the eroded and uneroded part; (c−d) typical morphology of an uneroded (c) and eroded (d) area.

little amount" to the "large amount" Ag_3PO_4 film has also been verified by the increased diffraction intensity of the characteristic peaks of metallic Ag^0 phase in XRD patterns (Figure 1.6), as well as the slightly positive shift of peak positions in the XPS narrow scans of the Ag 3d region (Figure 1.8a). Specifically, because the 3d peaks for Ag^+ are at 367.8 and 373.8 eV respectively, while the corresponding peak centers for Ag^0 are at 369.2 and 375.2 eV, such a gradually positive shift could help to confirm the increase in the amount of Ag^0 NPs on the surface of the Ag_3PO_4 microcrystalline films.[47,50−52] The similar phenomenon is also observed in the Ag MVV Auger electron region (Figure 1.8b).[53−54] Meanwhile, it is clear that as the amount of the surface precipitated Ag^0 NPs gets increased, the surface roughness of the Ag_3PO_4 microcrystalline film will also increase (Figure 1.5), accompanied by the decrease in the crystallinity (*i.e.* increase in the amount of native defects involving V_{Ag} and Ag_i) which are revealed by the decreased intensities of the characteristic diffraction peaks of Ag_3PO_4 in the XRD patterns (Figure 1.6), and also the Raman scattering bands in as-recorded Raman spectra (Figure 1.7).

It should be noticed that despite the fact that the Ag^0 NPs on the surface of Ag_3PO_4 may become recombination centers and also decrease the electrochemical surface areas (ECSAs) of the microcrystalline film photoanode, which are both unfavorable for PEC water oxidation performance, these Ag^0 NPs could be advantageous as well from other aspects. For one thing, the increased amount of metallic Ag^0 NPs precipitated on the surface could help to promote the interfacial conductivity, and therefore the interfacial charge transfer rate of the Ag_3PO_4 film photoanodes, as witnessed by the EIS spectra in Figure 1.9. For another thing, these Ag^0 NPs could also help to achieve enhanced light absorption of the Ag_3PO_4 photoanode due to their favorable plasmonic effect.[43,55] It could be seen clearly in Figure 1.10 that as the amount of Ag^0 NPs on the surface of the

Ag_3PO_4 microcrystalline film photoanode increases, light absorption get improved in the region of ≤ ~600 nm. Indeed, this is favorable for improving the PEC performance. However, the maximum light absorbance across the whole ultraviolet−visible light band of ~0.7 which is achieved by the Ag_3PO_4 microcrystalline film having "large amount" of Ag^0 NPs precipitated on the surface, is still far from satisfactory, as has already been discussed in the above section. Moreover, this sample (*i.e.* "large amount" one) and the accordingly fabricated Ag_3PO_4 film photoanode finally shows the lowest photocurrent density (Figure 1.11a and Figure 1.12) and positively shifted onset potential (the inset in Figure 1.11a and Figure 1.12), which should be mainly resulted from the increase in the defect amount.[3,56−57] Besides, it is also noticeable that the microcrystalline Ag_3PO_4 film photoanode with the "moderate amount" of Ag^0 NPs on the surface, despite having achieved the highest photocurrent density among the three different samples, as shown in Figure 1.11a and Figure 1.12, has still failed to demonstrate superior stability due to the non-negligible defect-induced decomposition of the active material of Ag_3PO_4, and thus precipitation of metallic Ag^0 NP aggregations (*i.e.* the while aggregations in Figure 1.13c), as can be known from Figure 1.11b and Figure 1.13. Hence in this regard, there is still much work needed to be done in order to fundamentally reduce the native defects of Ag_3PO_4 towards improved PEC water oxidation stability and efficiency.

References

[1] Fujishima, A.; Honda, K. Electrochemical Photolysis of Water at a Semiconductor Electrode. *Nature* **1972**, *238*, 37–38.

[2] Li, C.; Cao, Q.; Wang, F.; Xiao, Y.; Li, Y.; Delaunay, J.-J.; Zhu, H. Engineering Graphene and TMDs Based van der Waals Heterostructures for Photovoltaic and Photoelectrochemical Solar Energy Conversion. *Chem. Soc. Rev.* **2018**, *47*, 4981–5037.

[3] Sivula, K.; Le Formal, F.; Grätzel, M. Solar Water Splitting: Progress Using Hematite (α–Fe_2O_3) Photoelectrodes. *ChemSusChem* **2011**, *4*, 432–449.

[4] Jiang, C.; Moniz, S. J. A.; Wang, A. Q.; Zhang, T.; Tang, J. Photoelectrochemical Devices for Solar Water Splitting – Materials and Challenges. *Chem. Soc. Rev.* **2017**, *46*, 4645–4660.

[5] Zhang, Z.; Yates, J. T. Band Bending in Semiconductors: Chemical and Physical Consequences at Surfaces and Interfaces. *Chem. Rev.* **2012**, *112*, 5520–5551.

[6] Bisquert, J.; Cendula, P.; Bertoluzzi, L.; Gimenez, S. Energy Diagram of Semiconductor/Electrolyte Junctions. *J. Phys. Chem. Lett.* **2014**, *5*, 205–207.

[7] Gan, J.; Lu, X.; Tong, Y. Towards Highly Efficient Photoanodes: Boosting Sunlight-Driven Semiconductor Nanomaterials for Water Oxidation. *Nanoscale* **2014**, *6*, 7142–7142.

[8] Martin, D. J.; Liu, G.; Moniz, S. J. A.; Bi, Y.; Beale, A. M.; Ye, J.; Tang, J. Efficient Visible Driven Photocatalyst, Silver Phosphate: Performance, Understanding and Perspective. *Chem. Soc. Rev.* **2015**, *44*, 7808–7828.

[9] Kageshima, Y.; Kumagai, H.; Minegishi, T.; Kubota, J.; Domen, K. A Photoelectrochemical Solar Cell Consisting of a Cadmium Sulfide Photoanode and a

Ruthenium–2,2′-Bipyridine Redox Shuttle in a Non-Aqueous Electrolyte. *Angew. Chem. Int. Ed.* **2015**, *54*, 7877–7881.

[10] Zhong, M.; Hisatomi, T.; Sasaki, Y.; Suzuki, S.; Teshima, K.; Nakabayashi, M.; Shibata, N.; Nishiyama, H.; Katayama, M.; Yamada, T.; Domen, K. Highly Active GaN-Stabilized Ta_3N_5 Thin-Film Photoanode for Solar Water Oxidation. *Angew. Chem. Int. Ed.* **2017**, *56*, 4739–4743.

[11] Sahara, G.; Kumagai, H.; Maeda, K.; Kaeffer. N.; Artero, V.; Higashi, M.; Abe, R.; Ishitani, O. Photoelectrochemical Reduction of CO_2 Coupled to Water Oxidation Using a Photocathode with a Ru(II)–Re(I) Complex Photocatalyst and a CoO_x/TaON Photoanode. *J. Am. Chem. Soc.* **2016**, *138*, 14152−14158.

[12] Lee, D. K.; Choi, K.-S. Enhancing Long-Term Photostability of $BiVO_4$ Photoanodes for Solar Water Splitting by Tuning Electrolyte Composition. *Nat. Energy* **2018**, *3*, 53–60.

[13] Kuang, Y.; Jia, Q.; Ma, G.; Hisatomi, T.; Minegishi, T.; Nishiyama, H.; Nakabayashi, M.; Shibata, N.; Yamada, T.; Kudo, A.; Domen K. Ultrastable Low-Bias Water Splitting Photoanodes *via* Photocorrosion Inhibition and *in Situ* Catalyst Regeneration. *Nat. Energy* **2016**, *2*, 16191.

[14] Zhong, M.; Hisatomi, T.; Minegishi, T.; Nishiyama, H.; Katayama, M.; Yamada, T.; Domen, K. Bulky Crystalline $BiVO_4$ Thin Films for Efficient Solar Water Splitting. *J. Mater. Chem. A* **2016**, *4*, 9858−9864.

[15] Zhong, M.; Hisatomi, T.; Kuang, Y.; Zhao, J.; Liu, M.; Iwase, A.; Jia, Q.; Nishiyama, H.; Minegishi, T.; Nakabayashi, M.; Shibata, N.; Niishiro, R.; Katayama, C.; Shibano, H.; Katayama, M.; Kudo, A.; Yamada, T.; Domen, K. Surface Modification of CoO_x Loaded $BiVO_4$ Photoanodes with Ultrathin *p*-Type NiO Layers for Improved Solar Water Oxidation. *J. Am. Chem. Soc.* **2015**, *137*, 5053−5060.

[16] Zhou, Y.; Zhang, L.; Lin, L.; Wygant, B. R.; Liu, Y.; Zhu, Y.; Zheng, Y.; Mullins, C. B.; Zhao, Y.; Zhang, X.; Yu, G. Highly Efficient Photoelectrochemical Water Splitting from Hierarchical WO_3/$BiVO_4$ Nanoporous Sphere Arrays. *Nano Lett.* **2017**, *17*, 8012−8017.

[17] Yuan, K.; Cao, Q.; Li, X.; Chen, H.-Y.; Deng, Y.; Wang, Y.-Y.; Luo, W.; Lu, H.-L.; Zhang, D. W. Synthesis of WO_3@$ZnWO_4$@ZnO-ZnO Hierarchical Nanocactus Arrays for Efficient Photoelectrochemical Water Splitting. *Nano Energy* **2017**, *41*, 543−551.

[18] Yuan, K.; Cao, Q.; Lu, H.-L.; Zhong, M.; Zheng, X.; Chen, H.-Y.; Wang, T.; Delaunay, J.-J.; Luo, W.; Zhang, L.; Wang, Y.-Y.; Deng, Y.; Ding, S.-J.; Zhang, D. W. Oxygen-Deficient WO_{3-x}@TiO_{2-x} Core–Shell Nanosheets for Efficient Photoelectrochemical Oxidation of Neutral Water Solutions. *J. Mater. Chem. A* **2017**, *5*, 14697−14706.

[19] Tennakone, K.; Jayatissa, A. H.; Wijeratne, W. Photocleavage of Water with Silver Phosphate. *J. Chem. Soc., Chem. Commun.* **1988**, 496–498.

[20] Yi, Z.; Ye, J.; Kikugawa, N.; Kako, T.; Ouyang, S.; Stuart-Williams, H.; Yang, H.; Cao, J.; Luo, W.; Li, Z.; Liu, Y.; Withers, R. L. An Orthophosphate Semiconductor with Photooxidation Properties under Visible-Light Irradiation. *Nat. Mater.* **2010**, *9*, 559–564.

[21] Martin, D. J.; Umezawa, N.; Chen, X.; Ye, J.; Tang, J. Facet Engineered Ag_3PO_4 for Efficient Water Photooxidation. *Energy Environ. Sci.* **2013**, *6*, 3380–3386.

[22] Bi, Y.; Ouyang, S.; Umezawa, N.; Cao, J.; Ye, J. Facet Effect of Single-Crystalline Ag_3PO_4 Sub-Microcrystals on Photocatalytic Properties. *J. Am. Chem. Soc.* **2011**, *133*, 6490−6492.

[23] Huang, S.; Xu, Y.; Zhou, T.; Xie, M.; Ma, Y.; Liu, Q.; Jing, L.; Xu, H.; Li, H. Constructing Magnetic Catalysts with *in-Situ* Solid-Liquid Interfacial Photo-Fenton-Like Reaction over Ag_3PO_4@$NiFe_2O_4$ Composites. *Appl. Catal., B* **2018**, *225*, 40−50.

[24] Li, Y.; Wang, P.; Huang, C.; Yao, W.; Wu, Q.; Xu, Q. Synthesis and Photocatalytic Activity of Ultrafine Ag_3PO_4 Nanoparticles on Oxygen Vacated TiO_2. *Appl. Catal., B* **2017**, *205*, 489−497.

[25] Yan, T.; Tian, J.; Guan, W.; Qiao, Z.; Li, W.; You, J.; Huang, B. Ultra-Low Loading of Ag_3PO_4 on Hierarchical In_2S_3 Microspheres to Improve the Photocatalytic Performance: The Cocatalytic Effect of Ag and Ag_3PO_4. *Appl. Catal., B* **2017**, *202*, 84−94.

[26] Chen, F.; Yang, Q.; Li, X.; Zeng, G.; Wang, D.; Niu, C.; Zhao, J.; An, H.; Xie, T.; Deng, Y. Hierarchical Assembly of Graphene-Bridged Ag_3PO_4/Ag/$BiVO_4$(040) Z-Scheme Photocatalyst: An Efficient, Sustainable and Heterogeneous Catalyst with Enhanced Visible-Light Photoactivity towards Tetracycline Degradation under Visible Light Irradiation. *Appl. Catal., B* **2017**, *200*, 330−342.

[27] Xiang, Q.; Lang, D.; Shen, T.; Liu, F. Graphene-Modified Nanosized Ag_3PO_4 Photocatalysts for Enhanced Visible-Light Photocatalytic Activity and Stability. *Appl. Catal., B* **2015**, *162*, 196−203.

[28] Hou, Y.; Zuo, F.; Ma, Q.; Wang, C.; Bartels, L.; Feng, P. Ag_3PO_4 Oxygen Evolution Photocatalyst Employing Synergistic Action of Ag/AgBr Nanoparticles and Graphene Sheets. *J. Phys. Chem. C* **2012**, *116*, 20132−20139.

[29] Ma, X.; Lu, B.; Li, D.; Shi, R.; Pan, C.; Zhu, Y. Origin of Photocatalytic Activation of Silver Orthophosphate from First-Principles. *J. Phys. Chem. C* **2011**, *115*, 4680−4687.

[30] Botelho, G.; Sczancoski, J. C.; Andres, J.; Gracia, L.; Longo, E. Experimental and Theoretical Study on the Structure, Optical Properties, and Growth of Metallic Silver Nanostructures in Ag_3PO_4. *J. Phys. Chem. C* **2015**, *119*, 6293–6306.

[31] Yu, H; Jiao, Z.; Jin, B.; Feng, C.; Lu, G.; Bi, Y. Facile Synthesis of Porous Ag_3PO_4 Photocatalysts with High Self-Stability and Activity. *RSC Adv.* **2016**, *6*, 56166−56169.

[32] Cao, Q.; Liu, X.; Yuan, K.; Yu, J.; Liu, Q.; Delaunay, J.-J.; Che, R. Gold Nanoparticles Decorated Ag(Cl,Br) Micro-Necklaces for Efficient and Stable SERS Detection and Visible-Light Photocatalytic Degradation of Sudan I. *Appl. Catal., B* **2017**, *201*, 607−616.

[33] Reunchan, P; Umezawa, N. Native Defects and Hydrogen Impurities in Ag_3PO_4. *Phys. Rev B* **2013**, *87*, 245205.

[34] Sulaeman, U.; Hermawan, D.; Andreas, R.; Abdullah, A. Z.; Yin, S. Native Defects in Silver Orthophosphate and Their Effects on Photocatalytic Activity under Visible Light Irradiation. *Appl. Surf. Sci.* **2018**, *428*, 1029–1035.

[35] Zhai, H.; Yan, T.; Wang, P.; Yu, Y.; Li, W.; You, J.; Huang, B. Effect of Chemical Etching by Ammonia Solution on the Microstructure and Photocatalytic Activity of Ag_3PO_4 Photocatalyst. *Appl. Catal., A* **2016**, *528*, 104−112.

[36] Buckley, J. J.; Lee, A. F.; Olivi, L.; Wilson, K. Hydroxyapatite Supported Antibacterial Ag_3PO_4 Nanoparticles. *J. Mater. Chem.* **2010**, *20*, 8056−8063.

[37] Teng, W.; Li, X.; Zhao, Q.; Zhao, J.; Zhang, D. *In Situ* Capture of Active Species and Oxidation Mechanism of RhB and MB Dyes over Sunlight-Driven Ag/Ag_3PO_4 Plasmonic Nanocatalyst. *Appl. Catal., B* **2012**, *125*, 538−545.

[38] Cao, Q.; Yuan, K.; Liu, Q.; Liang, C.; Wang, X.; Cheng, Y.-F.; Li, Q.; Wang, M.; Che, R. Porous Au–Ag Alloy Particles Inlaid AgCl Membranes as Versatile Plasmonic Catalytic Interfaces with Simultaneous, *in Situ* SERS Monitoring. *ACS Appl. Mater. Interfaces* **2015**, *7*, 18491−18500.

[39] Cao, Q.; Che, R. Tailoring Au–Ag–S Composite Microstructures in One-Pot for Both SERS Detection and Photocatalytic Degradation of Plasticizers DEHA and DEHP. *ACS Appl. Mater. Interfaces* **2014**, *6*, 7020−7027.

[40] Wu, Q.; Diao, P.; Sun, J.; Xu, D.; Jin, T.; Xiang, M. Draining the Photoinduced

Electrons Away from an Anode: The Preparation of Ag/Ag_3PO_4 Composite Nanoplate Photoanodes for Highly Efficient Water Splitting. *J. Mater. Chem. A* **2015**, *3*, 18991−18999.

[41] Li, C.; Li, Y.; Delaunay, J.-J. A Novel Method to Synthesize Highly Photoactive Cu_2O Microcrystalline Films for Use in Photoelectrochemical Cells. *ACS Appl. Mater. Interfaces* **2014**, *6*, 480−486.

[42] Zhang, S.; Gu, X.; Zhao, Y.; Qiang, Y. Effect of Annealing Temperature and Time on Structure, Morphology and Visible-Light Photocatalytic Activities Ag_3PO_4 Microparticles. *Mater. Sci. Eng., B* **2015**, *201*, 57−65.

[43] Lin, Y.-G.; Hsu, Y.-K.; Chen, Y.-C.; Wang, S.-B.; Miller, J. T.; Chen, L.-C.; Chen, K.-H. Plasmonic $Ag@Ag_3(PO_4)_{1-x}$ Nanoparticle Photosensitized ZnO Nanorod-Array Photoanodes for Water Oxidation. *Energy Environ. Sci.* **2012**, *5*, 8917−8922.

[44] Teng, W.; Li, X.; Zhao, Q.; Chen, G. Fabrication of $Ag/Ag_3PO_4/TiO_2$ Heterostructure Photoelectrodes for Efficient Decomposition of 2-Chlorophenol under Visible Light Irradiation. *J. Mater. Chem. A* **2013**, *1*, 9060−9068.

[45] Cao, Q.; Yu, J.; Yuan, K.; Zhong, M.; Delaunay, J.-J. Facile and Large-Area Preparation of Porous Ag_3PO_4 Photoanodes for Enhanced Photoelectrochemical Water Oxidation. *ACS Appl. Mater. Interfaces* **2017**, *9*, 19507−19512.

[46] Yan, T.; Guan, W.; Xiao, Y.; Tian, J.; Qiao, Z.; Zhai, H.; Li, W.; You, J. Effect of Thermal Annealing on the Microstructures and Photocatalytic Performance of Silver Orthophosphate: The Synergistic Mechanism of Ag Vacancies and Metallic Ag. *Appl. Surf. Sci.* **2017**, *391*, 592–600.

[47] Yan, T.; Guan, W.; Tian, J.; Wang, P.; Li, W.; You, J.; Huang, B. Improving the Photocatalytic Performance of Silver Phosphate by Thermal Annealing: Influence of Acetate Species. *J. Alloy Compd.* **2016**, *680*, 436−445.

[48] Chang, Y.; Yu, K.; Zhang, C.; Li, R.; Zhao, P.; Lou, L.-L.; Liu, S. Three-Dimensionally Ordered Macroporous WO_3 Supported Ag_3PO_4 with Enhanced Photocatalytic Activity and Durability. *Appl. Catal., B* **2015**, *176*, 363−373.

[49] Tang, C.; Liu, E.; Wan, J.; Hu, X.; Fan, J. Co_3O_4 Nanoparticles Decorated Ag_3PO_4 Tetrapods as an Efficient Visible-Light-Driven Heterojunction Photocatalyst. *Appl. Catal., B* **2016**, *181*, 707−715.

[50] Dong, P.; Hou, G.; Liu, C.; Zhang, X.; Tian, H.; Xu, F.; Xi, X.; Shao, R. Origin of Activity and Stability Enhancement for Ag_3PO_4 Photocatalyst after Calcination. *Materials* **2016**, *9*, 968.

[51] Zhang, H.; Wang, G.; Chen, D.; Lv, X.; Li, J. Tuning Photoelectrochemical Performances of Ag−TiO_2 Nanocomposites *via* Reduction/Oxidation of Ag. *Chem. Mater.* **2008**, *20*, 6543−6549.

[52] Katsumata, H.; Hayashi, T.; Taniguchi, M.; Suzuki, T.; Kaneco, S. Highly Efficient Visible-Light Driven AgBr/Ag_3PO_4 Hybrid Photocatalysts with Enhanced Photocatalytic Activity. *Mater. Sci. Semicond. Process.* **2014**, *25*, 68−75.

[53] Hu, C.; Lan, Y.; Qu, J.; Hu, X.; Wang, A. Ag/AgBr/TiO_2 Visible Light Photocatalyst for Destruction of Azodyes and Bacteria. *J. Phys. Chem. B* **2006**, *110*, 4066−4072.

[54] Barreca, D.; Gasparotto, A.; Maragno, C.; Tondello, E. Silica-Supported Ag−Au Bimetallic Nanosystems by XPS. *Surf. Sci. Spectra* **2006**, *13*, 1−8.

[55] Gaidi, M.; Trabelsi, K.; Hajjaji, A.; Chourou, M. L.; Alhazaa, A. N.; Bessais, B.; El Khakani, M. A. Optimizing the Photochemical Conversion of UV−vis Light of Silver-Nanoparticles Decorated TiO_2 Nanotubes Based Photoanodes. *Nanotechnology* **2018**, *29*, 015703.

[56] Li, W.; Da, P.; Zhang, Y.; Wang, Y.; Lin, X.; Gong, X.; Zheng, G. WO_3 Nanoflakes for

Enhanced Photoelectrochemical Conversion. *ACS Nano* **2014**, *8*, 11770−11777.

[57] Wang, Y.; Zhang, Y.-Y.; Tang, J.; Wu, H.; Xu, M.; Peng, Z.; Gong, X.-G.; Zheng, G. Simultaneous Etching and Doping of TiO_2 Nanowire Arrays for Enhanced Photoelectrochemical Performance. *ACS Nano* **2013**, *7*, 9375−9383.

2. The effects of vacuum annealing boosting light absorption and water oxidation stability of novel microcrystalline Ag_3PO_4 film photoanodes

2.1. Supplementary introduction

It should be noted that the generation of native defects, *i.e.* the V_{Ag} and simultaneous precipitated metallic Ag^0 from Ag_3PO_4 photocatalysts, plays a completely different role in the case of photocatalytic dye degradation than PEC water oxidation using Ag_3PO_4 photoanodes. Typically in photocatalytic dye degradation reactions using Ag_3PO_4 as the photocatalyst, the synergistic effect of V_{Ag} and metallic Ag^0 precipitation may contribute to efficient separation of photogenerated electron–hole pairs, and consequently better photocatalytic performance. Unlike the multiple negative effects on the water oxidation performance of Ag_3PO_4 photoanodes, such opposite positive effects may have provided a promising strategy towards enhanced performance of Ag_3PO_4 photocatalysts. Hence in this regard, *in-situ* chemical etching using ethanol during the synthesis of Ag_3PO_4,[1] or post-etching using ammonia solution,[2] as well as post-annealing in air at different temperature and time conditions of the as-obtained Ag_3PO_4 powder photocatalyst,[3–7] have been exploited till now for intentionally introducing the V_{Ag} and metallic Ag^0 NPs on the surface, in order to achieve higher photocatalytic efficiencies and stability.

Light absorption is primarily determined by the bandgap, which in turn could also be modified by morphology, crystalline quality (*i.e.* crystallinity) and crystal structure, *etc*. In view of this, in consideration that annealing is a common method used to

improve the crystallinity and thus light absorption of semiconductor materials,[8–9] whereas it may also cause undesired precipitation of Ag^0 NPs on the surface of Ag_3PO_4 photoanodes, as has been discussed above in the Introduction section, it seems to be a double-edged sword for improving the PEC water oxidation performance of Ag_3PO_4 photoanodes. Herein this chapter, instead of the traditional air annealing methodology, we investigate the novel vacuum annealing on the modification of the crystallinity and properties of microcrystalline Ag_3PO_4 film photoanodes. It is amazingly found that such a vacuum annealing technique could help reduce the native defects, *i.e.* the V_{Ag} and its induced precipitation of metallic Ag^0 NPs on the surface, of the obtained Ag_3PO_4 films, affording substantially promoted bandgap light absorbance to as high as 0.9, and hence significantly improved PEC water oxidation stability and efficiency. Furthermore, the different mechanism of how the vacuum annealing process reduces the native defects of Ag_3PO_4 microcrystalline films, with a comparison to traditional air annealing process, has also been discussed.

2.2. Experimental details

Synthesis and annealing of Ag_3PO_4 microcrystalline films. The as-purchased silver foils (99.98%, 0.1 mm thick, Nilaco) were first cut into pieces (4.5 × 4.5 cm^2) and cleaned using dilute nitric acid solution (Sigma-Aldrich) and acetone (≥ 99.5%, Wako), respectively. Briefly, an aqueous solution was first prepared by mixing 7.2 g of sodium phosphate monobasic (NaH_2PO_4, ≥ 99.0%, Sigma-Aldrich), 482.8 g of hydrogen peroxide (H_2O_2, 30.0−35.5%, Sigma-Aldrich), and 10 g of polyvinylpyrrolidone (PVP, M_W ≈ 55,000, Sigma-Aldrich) under stirring at room temperature till the solution

became transparent. A piece of Ag foil was then immersed into the mixture solution and kept for 90 min. Afterwards, the foil was taken out of the solution and rinsed with ethanol (≥ 99.5%, Wako) and distilled water (resistivity ≥ 18 MΩ·cm) thoroughly, and dried in air naturally. Next, the obtained Ag_3PO_4 film was cut into smaller pieces (1.5 × 1.5 cm^2), loaded onto an alumina boat at the center of a quartz tube, and annealed in vacuum at 100 °C, 200 °C, 300 °C, 400 °C, and 500 °C, respectively for 2 h. Before annealing, the quartz tube was pumped using a mechanical pump for ≥ 20 min. During annealing, the ramp rate was kept at 1 °C/min for all samples, and after annealing, all the resulted Ag_3PO_4 microcrystalline films were cooled down naturally to room temperature for further usage.

Characterization. Scanning electron microscope (SEM) images were recorded using two different field-emission SEMs (FE-SEM, S4700 and S4800, Hitachi, Japan). X-ray diffraction (XRD) data were acquired on a Rigaku Miniflex II-MW (Japan) X-ray diffractometer working with Cu-K_α radiation (1.5406 Å). X-ray photoelectron spectroscopy (XPS) analysis was carried out using a PHI 5000 VersaProbe spectrometer (ULVAC-PHI, Japan) with an Al-K_α X-ray source (1486.6 eV). Raman spectra were collected on a laser confocal Raman micro-spectrometer (in*Via* reflex, Renishaw, UK) equipped with an integrated optical microscope (DM-2500, Leica, Germany). The excitation light source of a 632.8 nm He−Ne laser, laser power of 1.7 mW (10% × 17 mW), grating of 1800 1/mm, exposure time of 5.0 s, and accumulation of three times were applied for all Raman measurements. UV−visible diffuse-reflectance spectra (DRS) were measured on a JASCO V-670 (Japan) spectrophotometer equipped with an integrating sphere setup. Dark-field scattering spectra as well as microscopic images were taken by an Olympus BX61 industrial optical microscope (Japan) equipped with

the dark-field attachment along with Olympus MPLFLN-BD and LMPLFLN-BD objective lenses. This dark-field microscope is also connected with an IsoPlane-160 (Princeton Instruments, United States) spectrometer.

PEC and electrochemical measurements. For evaluation of the PEC water oxidation performance of the Ag_3PO_4 films, a three-electrode cell was assembled and used for all measurements. The Ag_3PO_4 photoelectrode, a Pt wire, an Ag/AgCl electrode, and the aqueous solution of Na_3PO_4 (0.02 M, pH ≈ 11.3) were utilized as the working electrode, counter electrode, reference electrode and electrolyte solution, respectively. Potential applied on working electrode was controlled by a VersaSTAT 4 potentiostat (Princeton Applied Research, United States). Before every measurement, the electrolyte solution was purged with high-purity nitrogen gas for ≥ 20 min under continuous magnetic stirring. During the measurements, the Ag_3PO_4 photoanodes were illuminated with a 500 W xenon lamp delivering an irradiance of 285 mW/cm^2. The scan rate was 10 mV/s from negative to positive potential for recording each current density−potential (*J*−*E*) curve. The electrochemical impedance spectroscopy (EIS) data were acquired under dark conditions at an applied potential of 1.0 V *vs.* Ag/AgCl varying the frequency between 100,000 (*i.e.* start frequency) and 500 Hz (*i.e.* end frequency) of a sinusoidal perturbation with 10 mV amplitude.

2.3. Results and discussion

Large-area (4.5 × 4.5 cm^2) microcrystalline Ag_3PO_4 films were first grown on as-purchased silver foils *via* a facile room-temperature and air-exposed solution process. This solution contained NaH_2PO_4 as the PO_4^{3+} sources, and H_2O_2 as the initial agent for

oxidation from Ag^0 to Ag^+, where the overall reaction could be described as follows:

$$2\ NaH_2PO_4 + 2\ H_2O_2 + 6\ Ag \rightarrow 2\ Ag_3PO_4 + 2\ NaOH + 2\ H_2O + H_2\uparrow$$

The as-obtained Ag_3PO_4 film, as shown in the SEM image in Figure 2.3a, turned out to be microcrystalline with irregular and faceted microcrystals on the surface, indicating that large crystals of Ag_3PO_4 could be generated from the reaction of PO_4^{3-} and Ag^+ at room temperature. The color of as-obtained microcrystalline Ag_3PO_4 film was dark khaki, as shown in Figure 2.1. After vacuum annealing for 2 h at different temperatures, the color of the Ag_3PO_4 film changed gradually. From Figure 2.1, it is clear that when higher annealing temperature was applied, the color of resulted Ag_3PO_4 film would be brighter. The Ag_3PO_4 microcrystalline films annealed at ≥ 300 °C, especially the 400 °C- and 500 °C-annealed films, display an obviously changed color appearance to even bright canary yellow. This drastic color change suggests that the optical properties of the 400 °C- and 500 °C-annealed Ag_3PO_4 films may have also been changed, and could help to exclude the possibility of the existence of a high content of Ag^0 or Ag_2O NPs on the surface of the Ag_3PO_4 film after undergoing a vacuum annealing process, as these may result in darker color (*e.g.*, green yellow or dark khaki) of the films just like the non-annealed one.[2,5]

The decreased amount of Ag^0 NPs on the surface of Ag_3PO_4 is directly confirmed by the dark-field microscopic analysis, as displayed in Figure 2.2. Dark-field imaging technique is widely used for probing Ag^0 nanostructures due to its sensitive response to the surface plasmon resonance (SPR) of silver,[10–11] whereas it is difficult to probe Ag^0 NPs accurately by SEM because many silver-based compounds can be destroyed, or reduced to give non-original Ag^0 NPs by high-energy electron beams during

measurements.[12–13] It is clear that in non-annealed Ag_3PO_4 microcrystalline film (Figure 2.2a), large amount of Ag^0 NPs (*i.e.* brighter white dots) were found to exist originally. This is because a part of Ag^+ in as-formed Ag_3PO_4 film may be reduced by the high-concentration electrons induced by the violet redox reaction, in consideration of the higher ionic mobility of Ag^+ than PO_4^{3-}, as well as the high mobility of electrons in these Ag_3PO_4 materials. In addition, the easy formation of intrinsic defects at room temperature during the solution growth of Ag_3PO_4 might have also contributed to this phenomenon because Ag^0 NPs would generated when interstitial Ag_i was reduced by electrons. It is amazing that after annealing the Ag_3PO_4 films in vacuum, as shown in Figure 2.2b–f, the amount of Ag^0 NPs on the surface decreases significantly. There are hardly any distinct Ag^0 aggregations that could be observed in the films annealed at ≥ 300 °C (Figure 2.2d–f), which is in good consistency with the change in color of the annealed Ag_3PO_4 films.

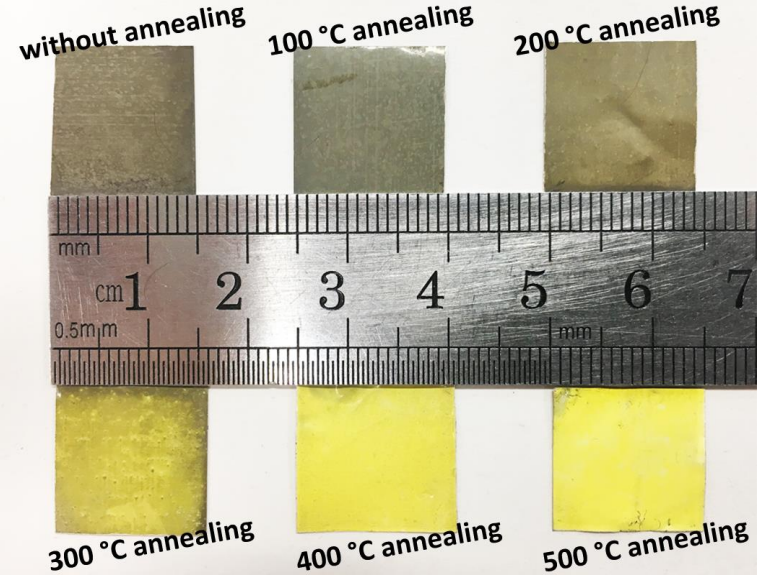

Figure 2.1. Optical images displaying the obvious color change from the non-annealed Ag_3PO_4 film (1.5 × 1.5 cm^2) to the films annealed at different temperatures.

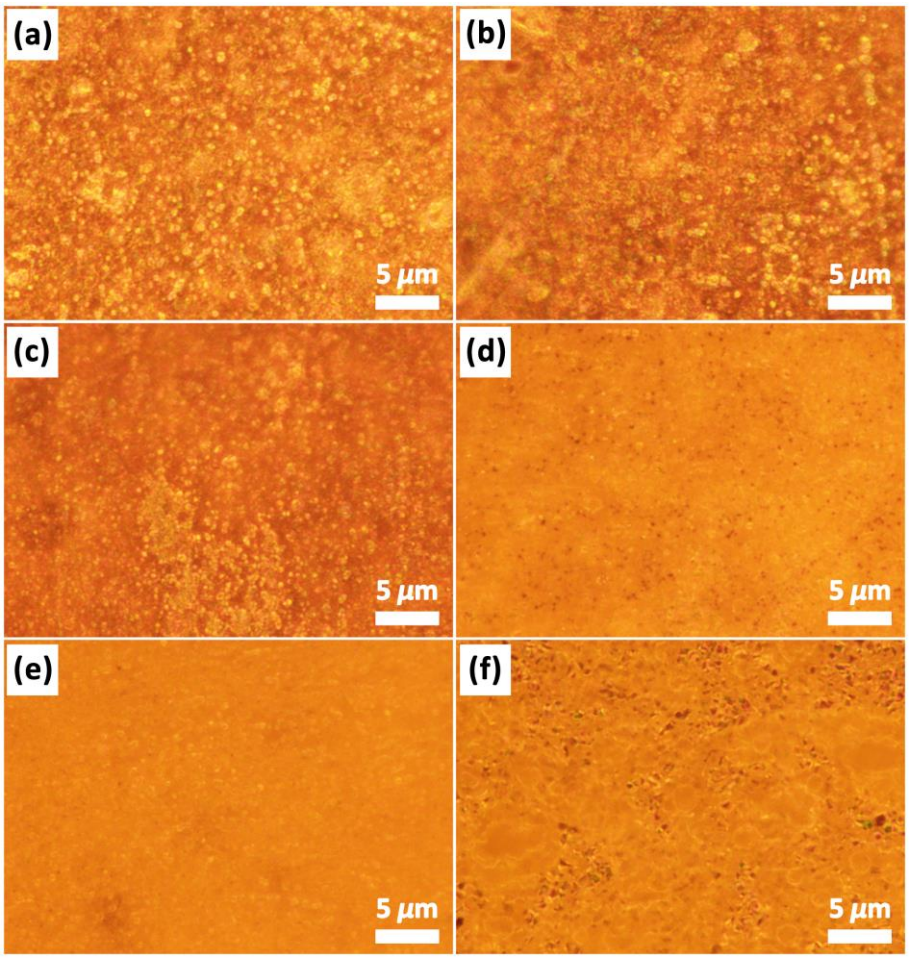

Figure 2.2. Dark-field microscopic images of the (a) non-annealed Ag_3PO_4 film, and the Ag_3PO_4 films annealed in vacuum at the temperature of (b) 100, (c) 200, (d) 300, (e) 400, and (f) 500 °C, respectively.

This unusual result of vacuum annealing that the amount of metallic Ag^0 NPs on the surface of Ag_3PO_4 got reduced as the annealing temperature was increased might be attributed to its different circumstance compared to air annealing. Regarding the traditional air annealing processes of Ag_3PO_4,[3–7] although most reports didn't give detailed explanation for the generation of more Ag^0 NPs after annealing, some researchers proposed that the metallic Ag^0 NPs might come from the reaction between Ag^+ and thermally excited electrons during annealing.[4,7] However, this cannot help to

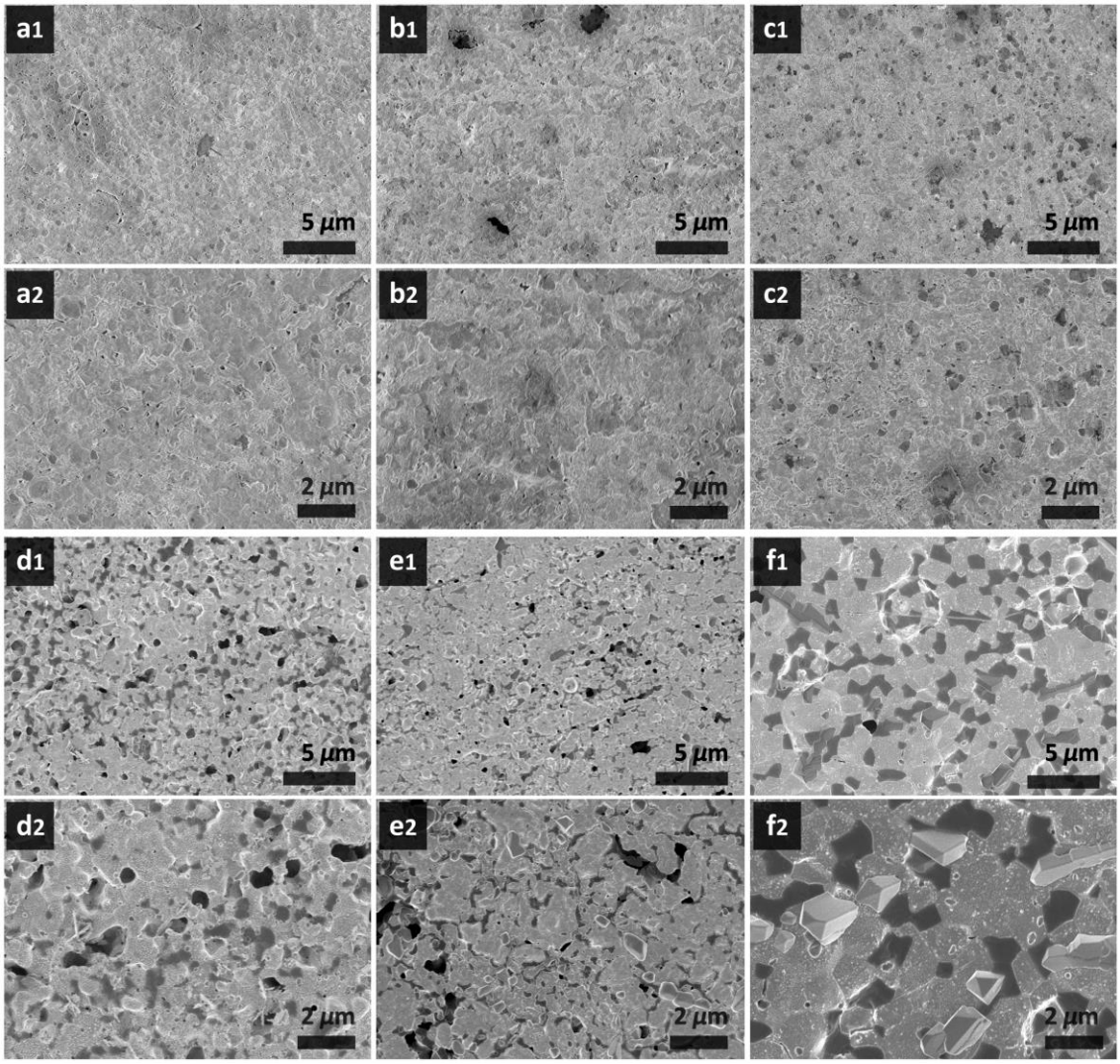

Figure 2.3. SEM images recorded at different magnifications of the (a) non-annealed Ag_3PO_4 film, and Ag_3PO_4 films annealed in vacuum at the temperature of (b) 100, (c) 200, (d) 300, (e) 400, and (f) 500 °C, respectively. For each sample, panels (1) and (2) display the low- and high-magnification SEM images.

understand the reduce in the amount of Ag^0 NPs on the surface when annealing Ag_3PO_4 in vacuum. Therefore, according to our experimental results, it is speculated that the precipitation of more Ag^0 NPs during air annealing is actually originated from the thermal decomposition of intermediate products. Typically, if Ag_3PO_4 is annealed in air

at a high temperature, due to the existence of reactive species in atmosphere involving the H_2O, CO_2 and O_2 molecules, unstable intermediates with low decomposition temperatures, such as AgOH, Ag_2CO_3, AgO and Ag_2O can easily form – after all, Ag_3PO_4 itself tends to be decomposed in a humid environment due to its poor structural stability.[6] For instance, the decomposition of Ag_2CO_3 into Ag^0 NPs, AgO and Ag_2O usually occurs at ~170 °C; the transformation of AgO to Ag_2O occurs in 100–200 °C; the complete thermal decomposition of Ag_2O into Ag occurs at 400 °C.[14–17] In this case, large quantities of Ag^0 NPs could be precipitated on the surface of Ag_3PO_4 films after annealing in air at ≥ 400 °C, due to the complete decomposition of intermediates. In contrast to air annealing, if annealing Ag_3PO_4 in vacuum, no such intermediates could form to generate Ag^0 NPs due to the absence of reactive gas molecules. Moreover, the originally existed Ag^0 NPs from room-temperature growth of the films may be melted, and thus disappear during high-temperature vacuum annealing process. Previous reports have demonstrated that the melting temperature of metallic nanostructures, including Ag^0 NPs depends greatly on the size.[18] The melting point of Ag^0 NPs, which was calculated to be ~480 °C using a classic thermodynamic description, could be lowered to ~400 °C at a decreased size, and can be further decreased to ~100 °C *via* the interaction with an ionic substrate.[19–21] Therefore, in consideration of the well-recognized superionic Ag^+ conductive properties of Ag_3PO_4,[22–23] it is rational that the melting point of Ag^0 NPs supported on Ag_3PO_4 surfaces could be decreased to quite low values, resulting in the reduce of the amount of Ag^0 NPs during annealing in vacuum at elevated temperatures. The melted Ag^0 NPs may become chemisorbed Ag^0 atoms, enter the defective lattices of Ag_3PO_4 *via* diffusion, and finally recover the intrinsic V_{Ag} defects, facilitating for higher crystalline

quality of the annealed Ag_3PO_4 films.

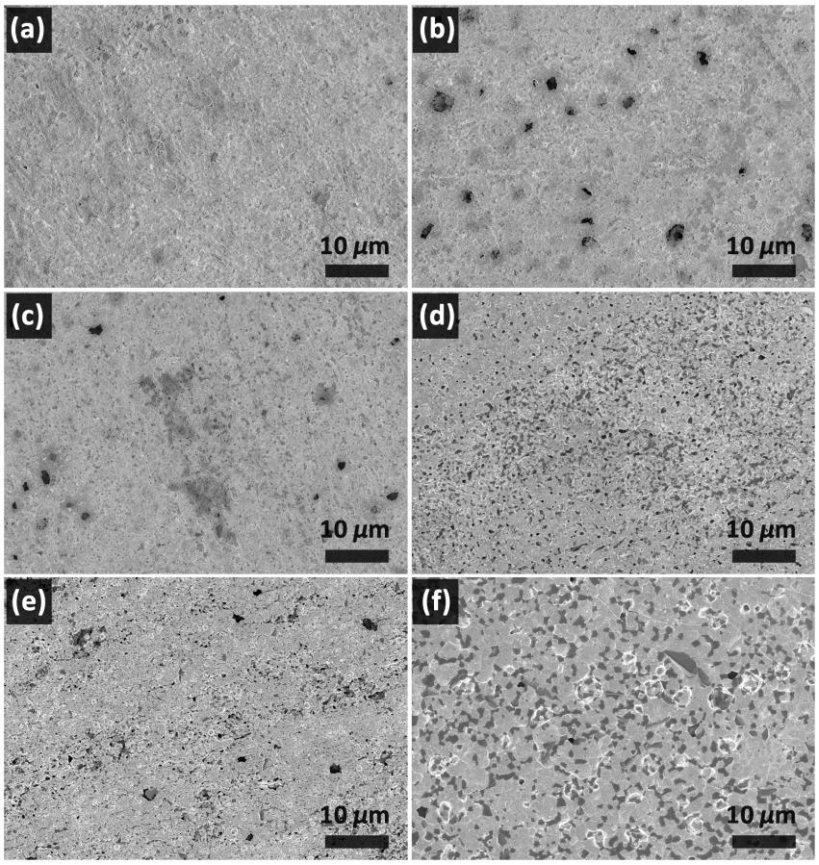

Figure 2.4. Low-magnification SEM images of the (a) non-annealed Ag_3PO_4 film, and the Ag_3PO_4 films annealed in vacuum at the temperature of (b) 100, (c) 200, (d) 300, (e) 400, and (f) 500 °C, respectively.

The morphological evolution of the Ag_3PO_4 microcrystalline films annealed at different temperatures is revealed by SEM images shown in Figure 2.3 and Figure 2.4 (*i.e.* larger-scale images). It is clear that the surface roughness of the Ag_3PO_4 microcrystalline films increases gradually after annealing. Specifically, the surface roughness increases slightly from non-annealed to 200 °C-annealed Ag_3PO_4 microcrystalline films (Figure 2.3a–c), and then increases significantly from 300 °C- to 500 °C-annealed films (Figure 2.3d–f). This should be resulted from the crystal growth

of Ag_3PO_4 during annealing. It is notable that in the films annealed at 400 °C, some faceted bulk crystals could be observed (Figure 2.3e and Figure 2.5a), and when the annealing temperature further goes to 500 °C, as shown in Figure 2.3f and Figure 2.5b, more bulk crystals of Ag_3PO_4 with larger size and more faceted surfaces can be identified. The non-negligible large amount of Ag_3PO_4 bulk crystals could be observed more obviously when the inside of the 500 °C-annealed film has been exposed and shown in Figure 2.6.

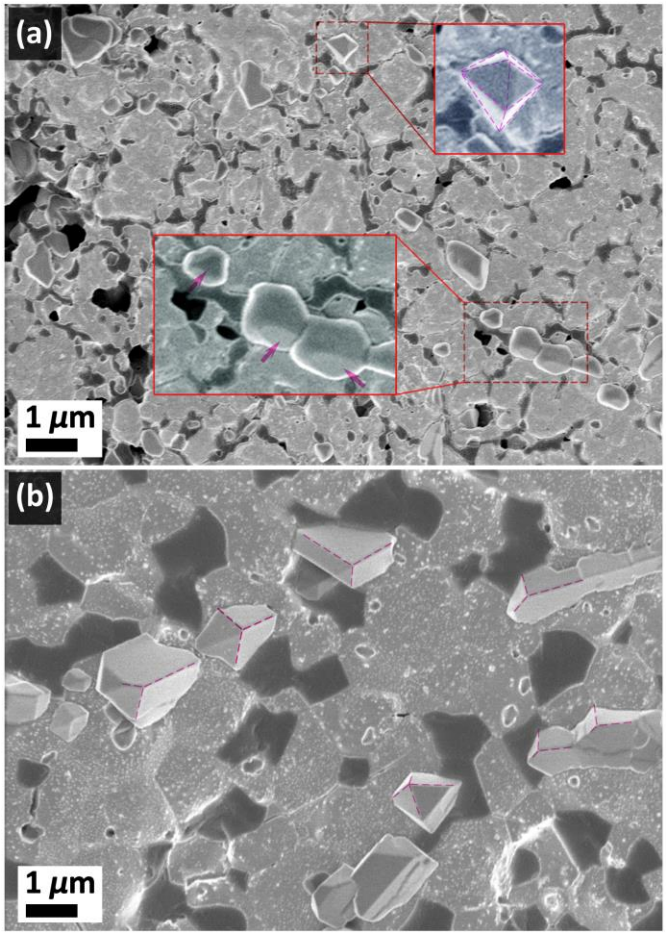

Figure 2.5. Enlarged SEM images and detailed analysis of the precipitated 2nd-phase bulk crystals of Ag_3PO_4 in the resulted films annealed at (a) 400 °C and (b) 500 °C. Panels (a) and (b) correspond to the panels (e_2) and (f_2) of Figure 2.3, respectively.

Based on these results, it could be deduced that the annealing process of the Ag_3PO_4 microcrystalline films could be divided into 3 stages depending on different annealing temperatures: 1) From room temperature (*i.e.* non-annealed) to 300 ºC is the |Recovery| stage, in which the amount of intrinsic defects V_{Ag} and Ag_i decreases, and the crystallinity increases; 2) From 300 ºC to 400 ºC, likely more close to 400 ºC, the |Recrystallization| stage starts, when the precipitation of Ag_3PO_4 bulk starts; 3) From 400 ºC to 500 ºC and higher temperature is the |Recrystallization + Grain growth| stage, when more and larger bulk crystals of Ag_3PO_4 are precipitated.

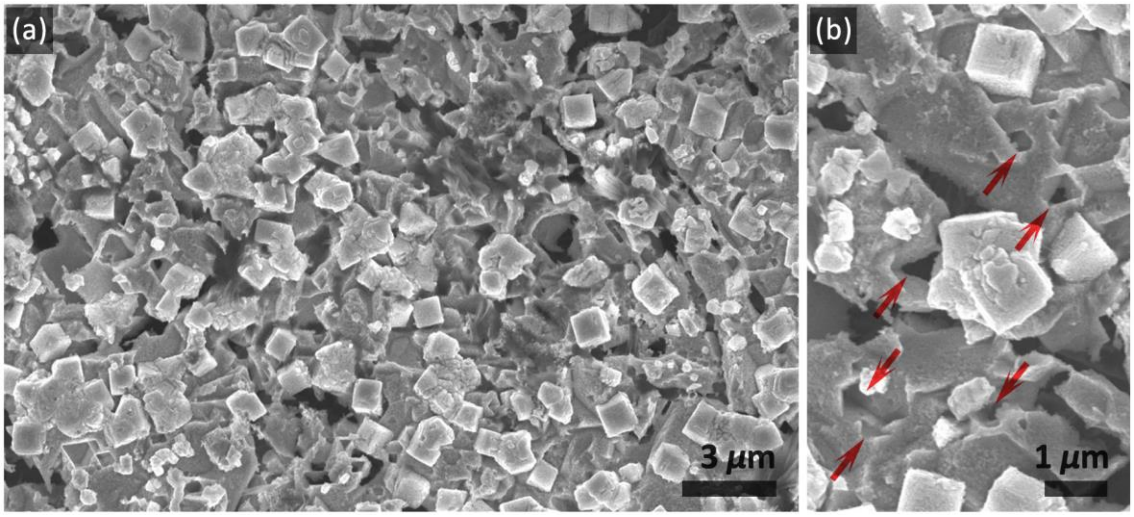

Figure 2.6. SEM images recorded at different magnifications showing the inside of the 500 °C-annealed Ag_3PO_4 film. This sample was prepared by tearing up the Ag_3PO_4 film using a conductive tape to make the inside exposed. Red arrows in panel (b) indicate the resulted potholes when the second-phase bulk crystals of Ag_3PO_4 were moved away.

To verify the component and phase purity of the non-annealed and annealed Ag_3PO_4 microcrystalline films, two X-ray techniques, XRD and XPS have been exploited for analyzing the films, as shown in Figure 2.7. Specifically in the XPS spectra exhibited in Figure 2.7b, for all the non-annealed and annealed microcrystalline film samples, the

characteristic peaks of Ag $3d_{3/2}$, Ag $3d_{5/2}$, P 2p and O 1s are identified to be at 373.2, 367.2, 131.9 and 529.9 eV of the binding energy, which show perfect matches with the literature values for Ag^{+}, as well as P^{5+} and O^{2-} in PO_4^{3-} units in Ag_3PO_4.[24–25] Meanwhile, in XRD patterns of all the non-annealed and annealed films (Figure 2.7a), all distinct diffraction peaks can be well indexed to the cubic *P*(–4)3*n* phase of silver orthophosphate (Ag_3PO_4, PDF#70-0702, labelled in blue in Figure 2.7a). Both these results confirm that the component of the films (*i.e.* pure-phase Ag_3PO_4) was retained essentially after annealing in vacuum at a relatively high temperature (≥ 400 ºC). The relative crystallinity of the Ag_3PO_4 films annealed in vacuum at different temperatures, as presented in Table 2.1, is evaluated from the relative intensity of the strongest (210) diffraction peaks of all samples, using that of non-annealed Ag_3PO_4 film as the reference.[6] It is clear that the Ag_3PO_4 microcrystalline films annealed at elevated

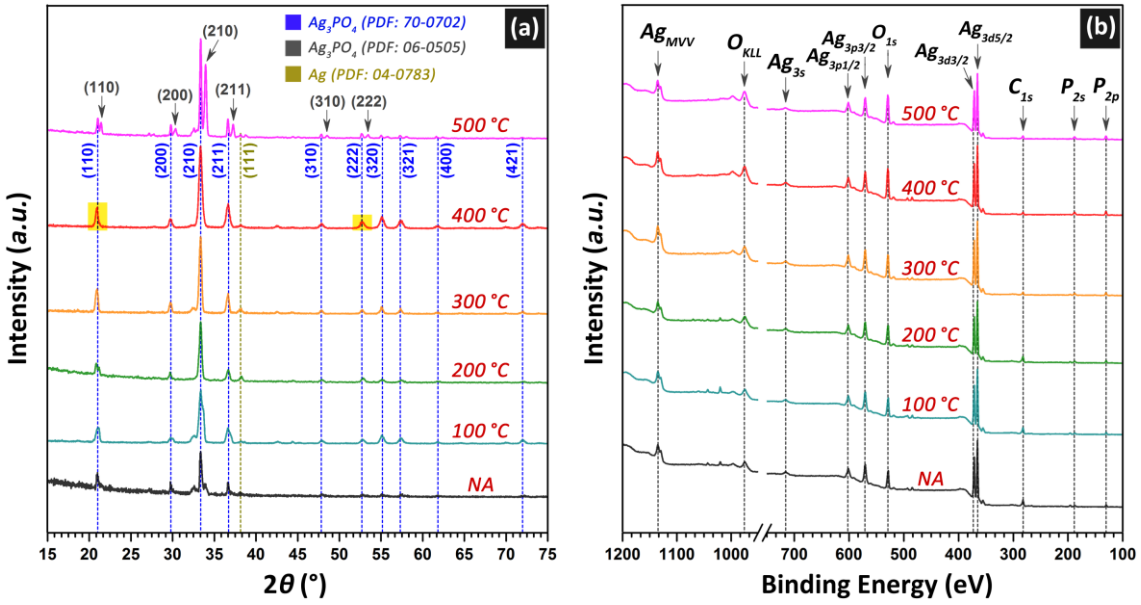

Figure 2.7. Representative (a) XRD patterns and (b) XPS spectra of the as-obtained microcrystalline Ag_3PO_4 films annealed at different temperatures. The abbreviation NA stands for the non-annealed Ag_3PO_4 film.

Table 2.1. Relative intensities of three characteristic diffraction peaks in the measured XRD patterns (Figure 2.7a) of all the obtained Ag_3PO_4 microcrystalline films, using the intensities of non-annealed (NA) Ag_3PO_4 as the reference. The relative intensity of the strongest peak, *i.e.* the (210) crystal plane, is used to indicate the relative crystallinity of all the obtained Ag_3PO_4 films.

Temperature	NA	100 °C	200 °C	300 °C	400 °C	500 °C
(2 1 0)	1.00	1.14	1.42	1.78	2.05	2.35
(1 1 0)	1.00	0.93	0.76	1.51	1.28	0.98
(2 2 2)	1.00	1.92	2.10	1.85	3.28	2.20

temperatures show higher crystallinity, confirming that the intrinsic defects of V_{Ag} and Ag_i could be recovered to afford better crystal quality of Ag_3PO_4 after annealing.

Besides, it should be noted that in the film annealed at 500 ºC, a second cubic *P*(–4)3*n* phase of Ag_3PO_4 (PDF#70-0702, labelled in gray in Figure 2.7a) can be clearly identified, which is supposed to be corresponding to the bulk crystals of Ag_3PO_4 precipitated in high-temperature annealing, as have already been revealed in SEM images in Figure 2.3e–f and Figure 2.5. In the 400 ºC-annealed microcrystalline film, the amount of such second-phase bulk crystals may be still too low for detection by XRD, whereas in the 500 ºC-annealed film, the considerable amount of these bulk crystals (Figure 2.6) is already enough to give distinct X-ray diffraction signals of the new peaks. More importantly, when compared to the original phase of the Ag_3PO_4 microcrystalline film, each characteristic peak of the second Ag_3PO_4 phase shows a

slight shift to a higher 2θ value, indicating that non-negligible lattice contraction must have occurred in these second-phase Ag_3PO_4 bulk crystals. It is assumed that during the high-temperature annealing in the oxygen-free conditions (*i.e.* vacuum) of the Ag_3PO_4 films, a small amount of oxygen vacancies (V_O) may be generated in the lattice, despite the recovery of silver atoms-based intrinsic defects at the same time. It is well recognized that the formation of V_O in oxide lattice would cause lattice contraction,[26–28] and the V_O in Ag_3PO_4 has a much higher formation energy compared to intrinsic V_{Ag} and Ag_i defects because of the strong P−O covalent bond that must be broken to remove O atoms.[29–30] Therefore, it is rational that such V_O can be formed when annealing Ag_3PO_4 in vacuum at ≥ 400 ºC: For one thing, the relatively high temperature could afford the energy to break the strong P−O covalence; For another, the oxygen-free conditions could facilitate the release of lattice oxygen as O_2. Finally, the existence of V_O in the lattice of the recrystallized and precipitated second-phase Ag_3PO_4 bulk crystals has resulted in such contraction. It is sometimes considered that such contraction derived from V_O, might in turn lead to the rearrangement of Ag_3PO_4 cells, along with the disappearance of V_{Ag}.[2] In addition, each characteristic diffraction peak of the second-phase Ag_3PO_4 shows lower intensities than the original phase, implying that the recrystallized Ag_3PO_4 bulk crystals are more defective with relatively low crystallinity than the original Ag_3PO_4 phase, which could also be regarded as an indirect evidence of the V_O in the bulk crystals.

Meanwhile, it is noticeable that the photoactivity of Ag_3PO_4 depends greatly on the exposure of specific crystal planes (*i.e.* facet engineering). Previous studies have pointed out that the {111} and {110} planes, especially the {111} plane of Ag_3PO_4, are the most favorable for photooxidation of water.[31–34] First, the {111} plane possesses

the highest surface energy because of the over-abundance of the dangling P–O bonds, which are designated oxidation sites. Second, the exposure of {111} plane also causes slicing of P–O bonds, which consequently lowers the layer-by-layer distance along the [111] direction. Further, because the photoholes in Ag_3PO_4 possess the smallest mass, and thus greatest mobility along the [111] direction, the exposure of {111} facet could help to achieve more efficient charge separation and faster charge transfer of photoholes for water oxidation reaction on the surface.[31,35] In view of this, relative intensities of the (222) and (110) planes have also been calculated from the XRD patterns (Figure 2.7a), and shown in Table 2.1. Typically, it is found that only the 300 ºC- and 400 ºC-annealed Ag_3PO_4 films show increased intensity of (110) plane than non-annealed Ag_3PO_4 film (300 ºC > 400 ºC), whereas the Ag_3PO_4 film annealed at 400 ºC exhibits much increased diffraction intensity, and thus possibly much enhanced exposure rate of the (222) plane. Overall, it is supposed the facet exposure of the 400 ºC-annealed film might be the most advantageous for photooxidation of water, as highlighted in yellow in Figure 2.7a.

Figure 2.8 displays the Raman spectroscopy analysis of as-obtained Ag_3PO_4 microcrystalline films before and after annealing at different temperatures. Raman spectroscopy is regarded as a powerful methodology for estimating the short-range order of solids.[36–37] It is revealed in Figure 2.8a that for the non-annealed Ag_3PO_4 film (*i.e.* the black curve), five characteristic Raman scattering bands could be identified at 238, 423, 564, 909, and 1015 cm^{-1} of the Raman shift, which can be assigned to the Raman-active vibrational modes of the rotation (238 cm^{-1}), symmetric bending (423 cm^{-1}), and asymmetric bending (564 cm^{-1}) of $[PO_4]$ tetrahedron units, as well as the symmetric stretching (909 cm^{-1}) and asymmetric stretching (1015 cm^{-1}) of O–P–O

bonds, respectively.[38–39] After the Ag_3PO_4 film was annealed at elevated temperature, several bands show obvious red-shifts. Specifically, the three bands located at ~423, 564 and 1015 cm^{-1} shift to 408, 549 and 1001 cm^{-1} respectively for the 400 ºC-annealed Ag_3PO_4 film. This red-shift could be explained by the phonon confinement effect and surface relaxation induced by increased crystal size after annealing at high temperature.[40–41] Meanwhile, the slightly increased intensities of the characteristic Raman bands indicate the improved crystallinity and lattice order of the Ag_3PO_4 films annealed at elevated temperatures, which is in consistency with the above XRD results.

Furthermore, significant difference between the Raman spectra of the non-annealed and 500 ºC-annealed Ag_3PO_4 films may provide more information, as disclosed by a direct comparison of these two samples (Figure 2.8b). It is surprising that the Ag_3PO_4 film after 500 ºC-annealing behaves just like bulk Ag_3PO_4, with nearly no obvious Raman signals ascribed to the modes of $[PO_4]$ units being detected (*i.e.* the yellow background region). In Ag_3PO_4 lattice, O–P–O bonds (*i.e.* the blue background region) are basic units, while the $[PO_4]$ tetrahedrons could be regarded as advanced combinations of O–P–O bonds. Naturally, due to the inductive effect of $[PO_4]$ units, the $[AgO_4]$ tetrahedrons are highly distorted in the lattice with two different O−Ag−O bond angles (α, β) being found. The native defect of V_{Ag} generated from the separation of interior silver atoms from the supercell further makes such distortion of the $[AgO_4]$ units even more severe, contributing to the flexibility of the $[PO_4]$ units as a result.[29] Such flexibility finally brings about the distinct signals of the vibrational modes of the $[PO_4]$ units in the non-annealed, defective Ag_3PO_4 film. On the contrary, the disappear of the modes of $[PO_4]$ units in the 500 ºC-annealed film suggests the recovery of defects and consequently increase in lattice order that make $[PO_4]$ units more fixed and difficult

to generate Raman vibrational signals, and can also help to confirm that the rearrangement of structural units and consequent recrystallization of Ag_3PO_4 bulk crystals do not involve the linking of $[PO_4]$ tetrahedra.[42]

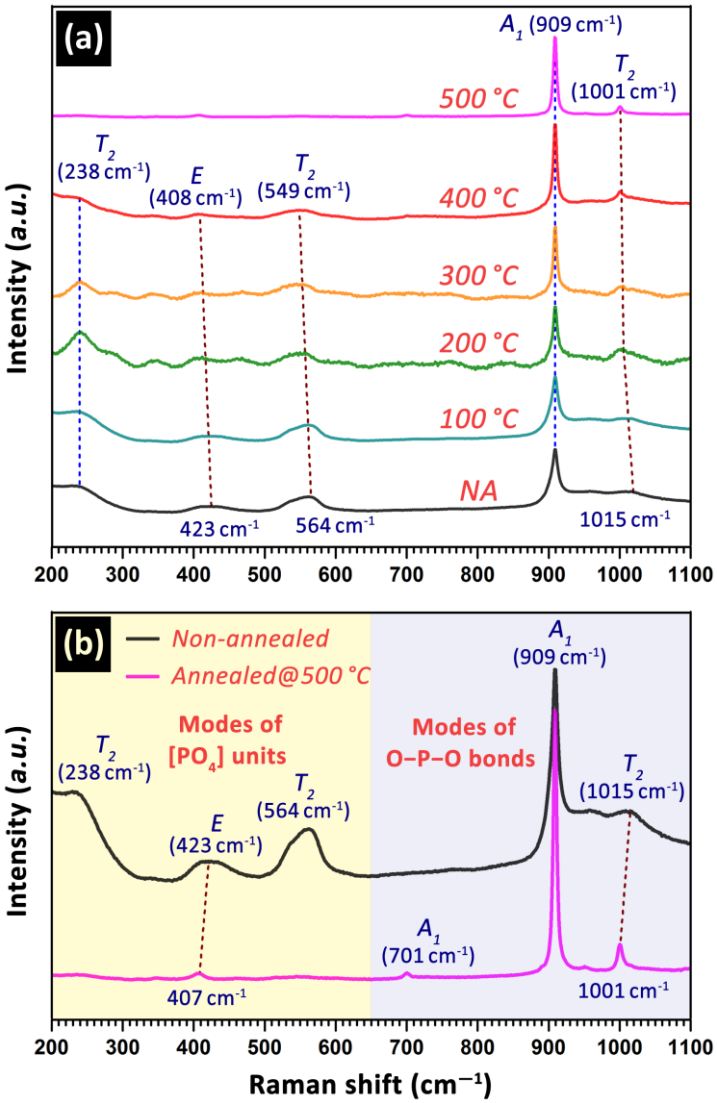

Figure 2.8. Room-temperature Raman spectra of (a) all the obtained Ag_3PO_4 films, and (b) a more detailed comparison of the non-annealed and 500 °C-annealed Ag_3PO_4 films. The abbreviation NA in panel (a) stands for the non-annealed Ag_3PO_4 film. The different singly, doubly, and triply degenerate vibrational modes are labelled by A_1, E, and T_2, respectively.

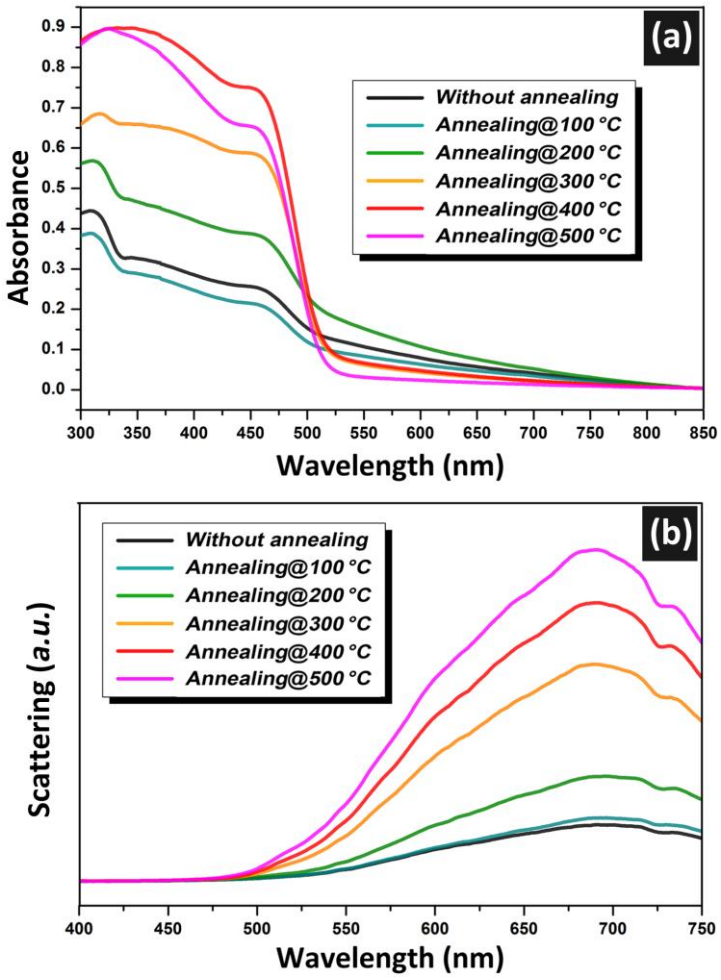

Figure 2.9. Room-temperature (a) DRS spectra and (b) dark-field scattering spectra of the obtained Ag_3PO_4 films before and after annealing at different temperatures.

Poor light absorption of the pristine Ag_3PO_4 films, as has been already discussed in the Introduction section, is an essential issue needed to be addressed. DRS spectra of the Ag_3PO_4 films before and after annealing at different temperatures, as exhibited in Figure 2.9a, have been recorded to unveil their substantially different light absorption profiles. It could be known that the absorption edges attributed to the charge transfer response of Ag_3PO_4 from its valence band to the conduction band, of the non-annealed Ag_3PO_4 film, as well as the films annealed at ≤ 200 °C appear at 560−570 nm, while the

absorption edges of the films annealed at ≥ 300 °C show up at 520−530 nm, which are quite near the standard value (~530 nm). Such a distinct red-shift in the absorption edge of the non-annealed and low-temperature annealed Ag_3PO_4 films should be resulted from the large amount of native defects, especially V_{Ag} originally existed in the lattice. Previous first-principles calculations have disclosed the influence of V_{Ag} on the electronic properties of Ag_3PO_4.[29−30,43−45] Ideally, intrinsic V_{Ag} in Ag_3PO_4 would act as defect states near the valence band edge to extend the absorption edge of Ag_3PO_4 in visible light band, typically from 530 nm to 560 nm.[29] Further, it is clear that for Ag_3PO_4 films annealed ≤ 200 °C, including the non-annealed film, non-negligible broad absorption in the sub-bandgap region of ≥ ~560 nm could be identified. This may come from three aspects: 1) The plasmon-enhanced visible light absorption arising from extensively existed Ag^0 NPs[46−47] on the surface of these defective Ag_3PO_4 films, as can be seen in Figure 2.2a−c; 2) Defect-state absorption from the large numbers of native V_{Ag} and Ag_i defects, as such a phenomenon has been widely discussed in other semiconductors like TiO_2 and $SrTiO_3$;[48−49] 3) Lower light scattering in the sub-bandgap region, as confirmed by the dark-field scattering spectra in Figure 2.9b. Therefore, after annealing the Ag_3PO_4 films at ≥ 300 °C, the recovery of native defects like V_{Ag}, decrease in the amount of Ag^0 NPs on the surface, as well as increased light scattering in the sub-bandgap region (Figure 2.9b) in the resulted Ag_3PO_4 films, have together decreased the sub-bandgap absorption to a relatively lower level.

More importantly, it is noticeable that the bandgap absorption of these Ag_3PO_4 microcrystalline films get greatly improved after annealing. The bandgap absorption of the Ag_3PO_4 film essentially increases if increased annealing temperature was applied, following the variation of the 400 ºC-annealed film > 500 ºC > 300 ºC > 200 ºC >

non-annealed > 100 ºC-annealed Ag_3PO_4 film. Particularly for the Ag_3PO_4 films annealed at ≥ 400 ºC, the light absorbance exceeds 0.7 across the whole bandgap region with sharp onset slopes near the absorption edge, and can even reach as high as ~0.9 in the ultraviolet band. Overall, this substantial improvement could be ascribed to the improved crystalline quality as has been confirmed by XRD and Raman results.[5] Meanwhile, the possibly existed small amount of V_O in the recrystallized Ag_3PO_4 bulk crystals in 400 ºC- and 500 ºC-annealed Ag_3PO_4 films might have also made contributions to achieving the superior absorbance, since the capability of V_O to enhance the light absorption and redox reactivity of photocatalysts has been widely reported in literature.[6,50–52]

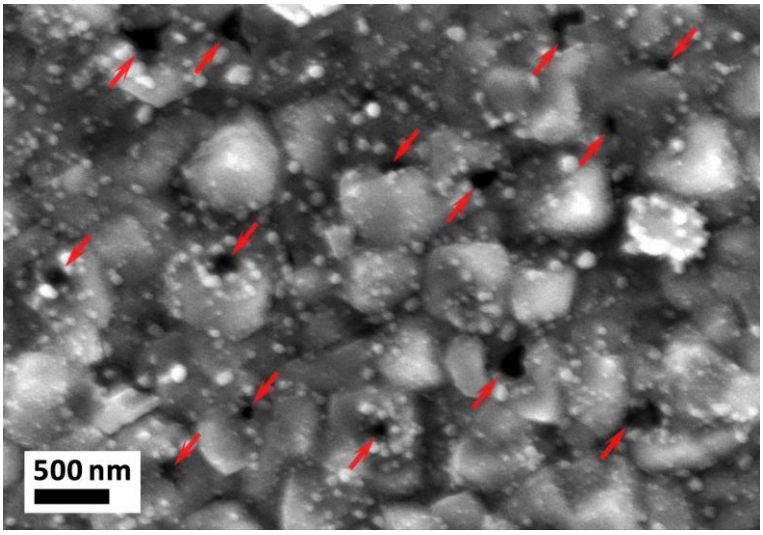

Figure 2.10. High-magnification SEM image of the 100 °C-annealed Ag_3PO_4 film. Red arrows indicate the positions where pores generated by gas (*e.g.*, water molecules) release or desorption.

Besides, the reason why the 100 ºC-annealed Ag_3PO_4 film shows lower absorption than non-annealed film is maybe because such a low annealing temperature has introduced more defects along with pores into the film *via* the release of adsorbed gas

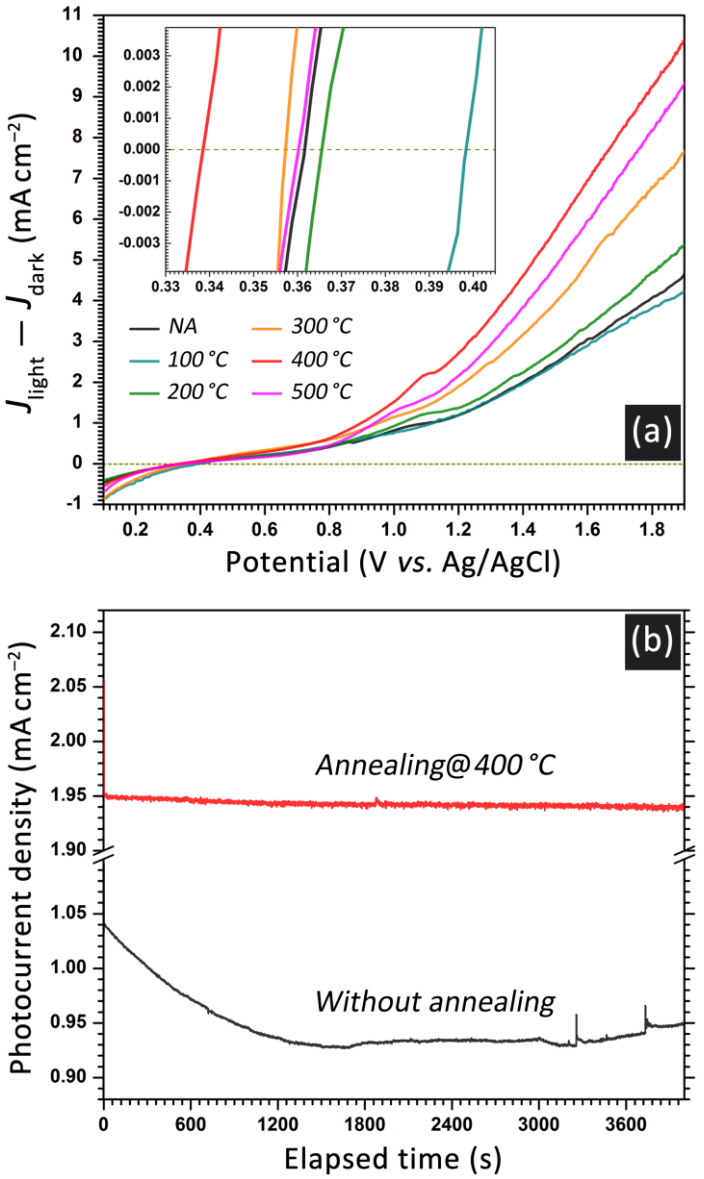

Figure 2.11. PEC water oxidation performance of the Ag_3PO_4 microcrystalline film photoanodes: (a) the dependence of photocurrent density minus dark current density ($J_{light} - J_{dark}$) on applied potential. Inset shows an enlarged view of the potential range from 0.330 to 0.405 V *vs.* Ag/AgCl. NA stands for the non-annealed Ag_3PO_4 photoanode. (b) Current density−time (J–t) curves of the photoanodes fabricated from non-annealed and 400 °C-annealed Ag_3PO_4 films during the stability test at an applied potential of 1 V *vs.* Ag/AgCl.

(*e.g.*, water desorption), while is still not high enough for the recovery of native defects, as witnessed by the high-magnification SEM image displayed in Figure 2.10. In addition, the slightly lower light absorption of the 500 ºC-annealed Ag_3PO_4 film than the 400 ºC-annealed one is maybe because the extensively distributed bulk crystals on the surface of the 500 ºC-annealed Ag_3PO_4 microcrystalline film, as revealed in Figure 2.3f and Figure 2.4f, may have decreased the surface area and also increased undesired light reflection of the film. In generally, it is considered that the 400 ºC-annealed Ag_3PO_4 film shows the most appealing light absorption profiles among all the obtained microcrystalline films.

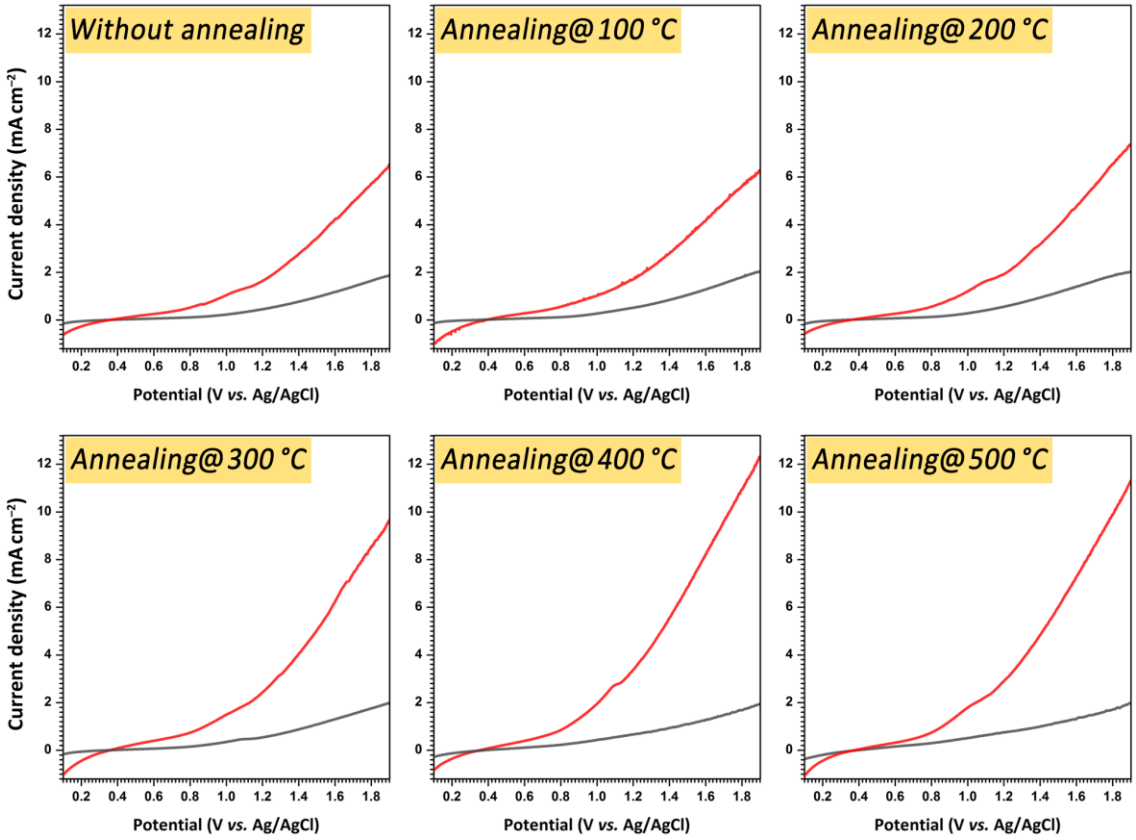

Figure 2.12. Comparisons of the photocurrent density (red curves) *vs.* dark current density (black curves) of different Ag_3PO_4 microcrystalline film photoanodes.

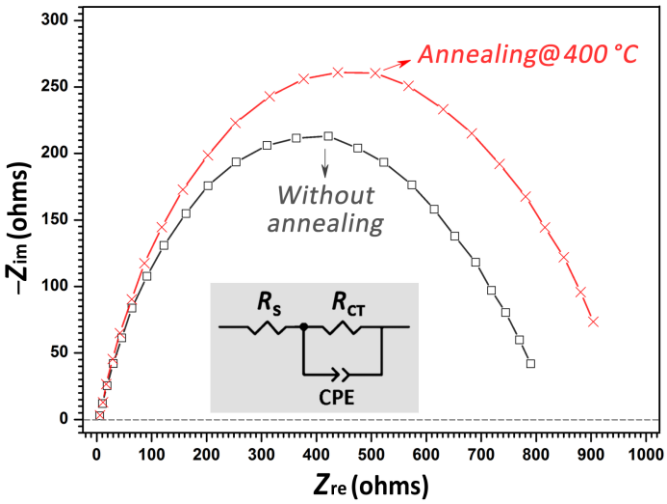

Figure 2.13. Electrochemical impedance spectroscopy (EIS) Nyquist plots of the non-annealed and 400 °C-annealed Ag_3PO_4 film photoanodes. The insert shows the equivalent circuit consisting of a serial resistor (R_S), a resistor–capacitor circuit showing the parallel combination of the interfacial charge transfer resistance (R_{CT}), and constant phase element (CPE) attributed to the interface between the electrode surface and the electrolyte solution.

The substantially improved physicochemical properties with regard to native defects like V_{Ag}, surface precipitation of Ag^0 NPs, and bandgap light absorption of the Ag_3PO_4 microcrystalline films obtained after vacuum annealing, together with their intrinsically high photoactivity, suggest the possibility towards improved stability and efficiency of PEC water oxidation. Figure 2.11a summarizes the dependency of photocurrent density minus dark current density ($J_{light} - J_{dark}$) on applied potential. It is obvious that the same variation in [$J_{light} - J_{dark}$] *vs.* E curves are found as the light absorption profiles, *i.e.* 400 ºC > 500 ºC > 300 ºC > 200 ºC > non-annealed > 100 ºC-annealed microcrystalline film photoanode, indicating that light absorption, especially the bandgap absorption could be

the dominant factor to the PEC performance of these Ag_3PO_4 film photoanodes. Figure 2.12 compares the photocurrent density *vs.* dark current density of all the photoanodes, confirming that the current density of these Ag_3PO_4 microcrystalline film photoanodes is mainly originated from the photocatalytic effect under light irradiation, instead of the electrocatalytic effect.

Particularly, much improved PEC water oxidation stability (Figure 2.11b) as well as efficiency of the 400 ºC-annealed Ag_3PO_4 film photoanode are demonstrated compared to the non-annealed Ag_3PO_4 film, suggesting that the methodology of vacuum annealing

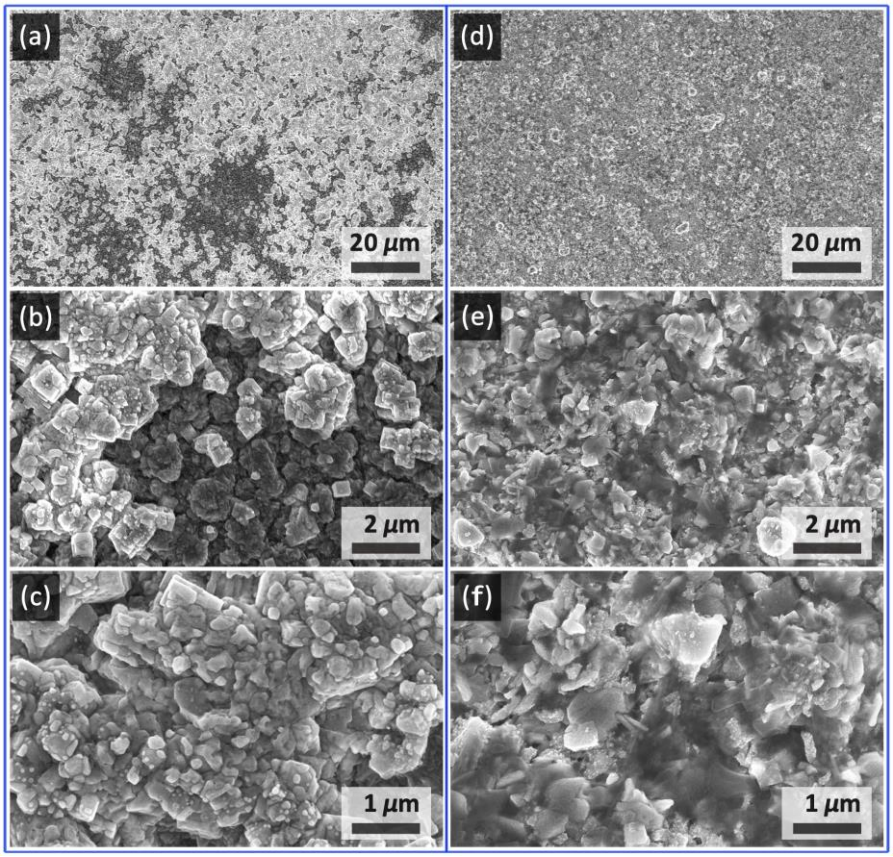

Figure 2.14. SEM images of different magnifications showing the surface morphology after the stability test of the photoanodes fabricated from (a−c) non-annealed and (d−f) 400 °C-annealed Ag_3PO_4 microcrystalline films.

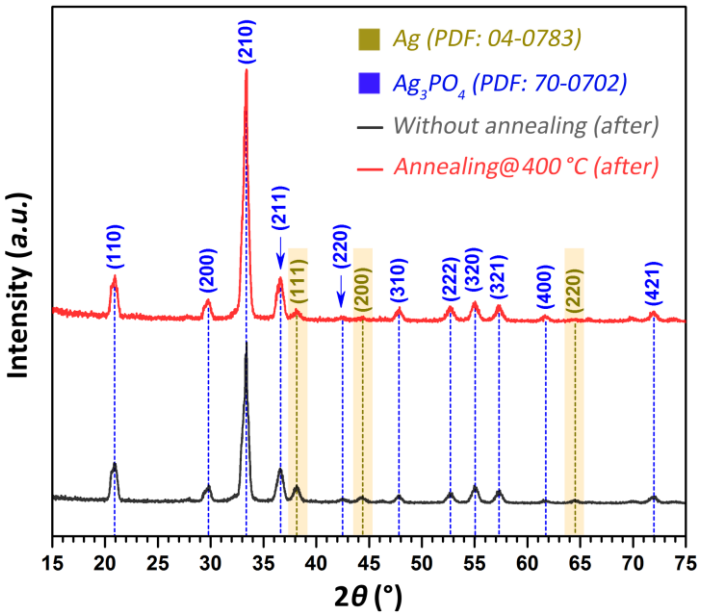

Figure 2.15. XRD patterns of the photoanodes fabricated from the non-annealed and 400 °C-annealed Ag_3PO_4 microcrystalline films after the stability test.

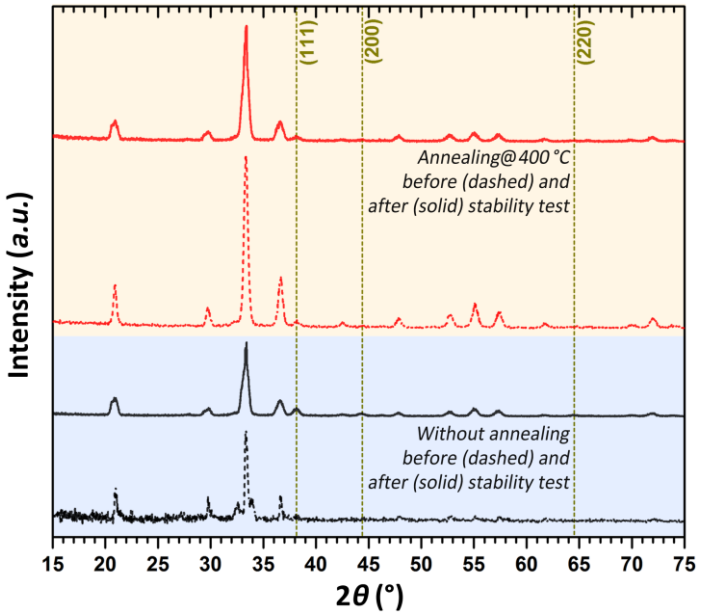

Figure 2.16. Representative XRD patterns of the non-annealed (*i.e.* blue-background part) and 400 °C-annealed (*i.e.* orange-background part) Ag_3PO_4 microcrystalline film photoanode before (*i.e.* dashed curves) and after (*i.e.* solid curves) the stability test. The dark yellow dashed lines indicate the peak positions of metallic Ag^0 phase.

could be useful for improving the PEC performance of the Ag_3PO_4 microcrystalline film photoanodes because of its ability to reduce the native defects like V_{Ag}, remove the Ag^0 NPs precipitated on the surface, and also increase the bandgap light absorption of these Ag_3PO_4 microcrystalline films. The significantly decreased amount of defects in the 400 ºC-annealed Ag_3PO_4 microcrystalline film photoanode, meanwhile, can also be known from its obviously shifted onset potential to a more negative value, as shown in the inset of Figure 2.11a.[53–55]

Electrochemical impedance spectroscopy (EIS) analytical technique is a strong tool to study the charge transfer process at the SEJ interface of PEC water oxidation reaction. In the derived Nyquist plots, the arch at the high frequency stands for the process of charge transfer, and its diameter indicates the charge carrier mobility; *i.e.* the smaller diameter the semicircle has, the faster charge carriers can transfer.[56] Herein, Figure 2.13 displays the slightly decreased interfacial charge transfer rate from the non-annealed Ag_3PO_4 microcrystalline film photoanode to the 400 ºC-annealed one. This is rational considering that defects are well recognized to be favorable for the conductivity,[57] nevertheless such a slight decrease in conductivity of the annealed microcrystalline Ag_3PO_4 film photoanodes should have minor influence on the PEC water oxidation efficiency (*i.e.* expressed as the photocurrent density) when compared with the distinctly improved light absorption.

Specifically, the much improved PEC water oxidation stability, as could be known from Figure 2.11b, can be understood from the following two aspects: For one thing, the surface erosion of the non-annealed Ag_3PO_4 microcrystalline film photoanode is much stronger than the 400 ºC-annealed one (Figure 2.14); For another, the decomposition of

Ag_3PO_4 into metallic Ag^0 in stability test of the 400 ºC-annealed microcrystalline film is less serious as well, as witnessed by the characteristic diffraction peaks corresponding to the metallic Ag^0 phase in the XRD patterns displayed in Figure 2.15 and Figure 2.16. Both points indicate less loss of the active material of Ag_3PO_4 in the 400 ºC-annealed microcrystalline film photoanode than the non-annealed one. Overall, it can be deduced that the reduced defects in the lattice of Ag_3PO_4, as well as the strong interaction among adjacent Ag_3PO_4 crystallites after annealing,[3] have together inhibited the precipitation of metallic Ag^0 NPs on the surface, and dissolution of Ag^+ from Ag_3PO_4 into aqueous solution, and finally contributed to the enhanced stability for PEC water oxidation.

2.4. Conclusions

In this chapter, solution-processed large-area Ag_3PO_4 microcrystalline films are first prepared *via* a room-temperature, air-exposed immersion reaction. The post-treatment of vacuum annealing at different temperatures (*i.e.* 100, 200, 300, 400 and 500 °C) has been investigated as a strategy for solving the problem of native defects and low light absorption of Ag_3PO_4. It is found that below 400 ºC is the |Recovery| stage for Ag_3PO_4 microcrystals when defect amount decreases and therefore crystallinity increases. From 400 ºC, the |Recrystallization| stage and also precipitation of Ag_3PO_4 bulk crystals start, and afterwards till 500 ºC is the |Recrystallization + Grain growth| stage for Ag_3PO_4, when more faceted and larger bulk crystals of Ag_3PO_4 precipitate extensively. In this series of Ag_3PO_4 film photoanodes, the same variation in $[J_{light} - J_{dark}]$ *vs.* E curves are found as the light absorption profiles, *i.e.* 400 ºC > 500 ºC > 300 ºC > 200 ºC > non-annealed > 100 ºC-annealed Ag_3PO_4 film, indicating that light absorption,

especially the bandgap absorption could be the dominant factor to the PEC performance. Particularly, much improved PEC water oxidation stability and efficiency of the 400 ^{o}C-annealed Ag_3PO_4 film photoanode are demonstrated compared with the non-annealed Ag_3PO_4 film, suggesting that the methodology of vacuum annealing could be utilized for improving the PEC performance of Ag_3PO_4 film photoanodes because of its ability to reduce the native defects like V_{Ag}, remove the Ag^0 NPs on the surface, and increase the bandgap light absorption of these Ag_3PO_4 microcrystalline films.

References

[1] Sulaeman, U.; Hermawan, D.; Andreas, R.; Abdullah, A. Z.; Yin, S. Native Defects in Silver Orthophosphate and Their Effects on Photocatalytic Activity under Visible Light Irradiation. *Appl. Surf. Sci.* **2018**, *428*, 1029–1035.

[2] Zhai, H.; Yan, T.; Wang, P.; Yu, Y.; Li, W.; You, J.; Huang, B. Effect of Chemical Etching by Ammonia Solution on the Microstructure and Photocatalytic Activity of Ag_3PO_4 Photocatalyst. *Appl. Catal., A* **2016**, *528*, 104−112.

[3] Yan, T.; Guan, W.; Xiao, Y.; Tian, J.; Qiao, Z.; Zhai, H.; Li, W.; You, J. Effect of Thermal Annealing on the Microstructures and Photocatalytic Performance of Silver Orthophosphate: The Synergistic Mechanism of Ag Vacancies and Metallic Ag. *Appl. Surf. Sci.* **2017**, *391*, 592–600.

[4] Yan, T.; Guan, W.; Tian, J.; Wang, P.; Li, W.; You, J.; Huang, B. Improving the Photocatalytic Performance of Silver Phosphate by Thermal Annealing: Influence of Acetate Species. *J. Alloy Compd.* **2016**, *680*, 436−445.

[5] Zhang, S.; Gu, X.; Zhao, Y.; Qiang, Y. Effect of Annealing Temperature and Time on Structure, Morphology and Visible-Light Photocatalytic Activities Ag_3PO_4 Microparticles. *Mater. Sci. Eng., B* **2015**, *201*, 57−65.

[6] Chong, R.; Cheng, X.; Wang, B.; Li, D.; Chang, Z.; Zhang, L. Enhanced Photocatalytic Activity of Ag_3PO_4 for Oxygen Evolution and Methylene Blue Degeneration: Effect of Calcination Temperature. *Int. J. Hydrogen Energy* **2016**, *41*, 2575−2582.

[7] Dong, P.; Hou, G.; Liu, C.; Zhang, X.; Tian, H.; Xu, F.; Xi, X.; Shao, R. Origin of Activity and Stability Enhancement for Ag_3PO_4 Photocatalyst after Calcination. *Materials* **2016**, *9*, 968.

[8] Ahn, K.-S.; Lee, S.-H.; Dillon, A. C.; Tracy, C. E.; Pitts, R. The Effect of Thermal Annealing on Photoelectrochemical Responses of WO_3 Thin Films. *J. Appl. Phys.* **2007**, *101*, 093524.

[9] Roiz, J.; Oliver, A.; Munoz, E.; Rodriguez-Fernandez, L.; Hernandez, J. M.; Cheang-Wong, J. C. Modification of the Optical Properties of Ag-Implanted Silica by Annealing in Two Different Atmospheres. *J. Appl. Phys.* **2004**, *95*, 1783−1791.

[10] Krasnok, A.; Caldarola, M.; Bonod, N.; Alu, A. Spectroscopy and Biosensing with Optically Resonant Dielectric Nanostructures. *Adv. Opt. Mater.* **2018**, *6*, 1701094.

[11] Weber-Bargioni, A.; Schwartzberg, A.; Schmidt, M.; Harteneck, B.; Ogletree, D. F.; Schuck, P. J.; Cabrini, S. Functional Plasmonic Antenna Scanning Probes Fabricated by Induced-Deposition Mask Lithography. *Nanotechnology* **2010**, *21*, 065306.

[12] Cheng, Y.-F.; Cao, Q.; Zhang, J.; Wu, T.; Che, R. Efficient Photodegradation of Dye Pollutants Using a Novel Plasmonic AgCl Microrods Array and Photo-Optimized Surface-Enhanced Raman Scattering. *Appl. Catal., B* **2017**, *217*, 37−47.

[13] Dong, R.; Tian, B.; Zeng, C.; Li, T.; Wang, T.; Zhang, J. Ecofriendly Synthesis and Photocatalytic Activity of Uniform Cubic Ag@AgCl Plasmonic Photocatalyst. *J. Phys. Chem. C* **2013**, *117*, 213–220.

[14] Pettinger, B.; Bao, X.; Wilcock, I.; Muhler, M.; Schlogl, R.; Ertl, G. Thermal Decomposition of Silver Oxide Monitored by Raman Spectroscopy: From AgO Units to Oxygen Atoms Chemisorbed on the Silver Surface. *Angew. Chem. Int. Ed.* **1994**, *33*, 85–86.

[15] Epling, W. S.; Hoflund, G. B.; Salaita, G. N. Surface Characterization Study of the Thermal Decomposition of Ag_2CO_3. *J. Phys. Chem. B* **1998**, *102*, 2263–2268.

[16] Waterhouse, G. I. N.; Bowmaker, G. A.; Metson, J. B. The Thermal Decomposition of Silver (I, III) Oxide: A Combined XRD, FT-IR and Raman Spectroscopic Study. *Phys.*

Chem. Chem. Phys. **2001**, *3*, 3838–3845.

[17] Aspromonte, S. G.; Mizrahi, M. D.; Schneeberger, F. A.; Lopez, J. M. R.; Boix, A. V. Study of the Nature and Location of Silver in Ag-Exchanged Mordenite Catalysts. Characterization by Spectroscopic Techniques. *J. Phys. Chem. C* **2013**, *117*, 25433−25442.

[18] Zhang, M.; Efremov, M. Y.; Schiettekatte, F.; Olson, E. A.; Kwan, A. T.; Lai, S. L.; Wisleder, T.; Greene, J. E.; Allen, L. H. Size-Dependent Melting Point Depression of Nanostructures: Nanocalorimetric Measurements. *Phys. Rev. B* **2000**, *62*, 10548−10557.

[19] Sun, J.; Ma, D.; Zhang, H.; Liu, X.; Han, X. W.; Bao, X.; Weinberg, G.; Pfander, N.; Su, D. Toward Monodispersed Silver Nanoparticles with Unusual Thermal Stability. *J. Am. Chem. Soc.* **2006**, *128*, 15756−15764.

[20] Asoro, M. A.; Damiano, J.; Ferreira, P. J. Size Effects on the Melting Temperature of Silver Nanoparticles: *In-situ* TEM Observations. *Microsc, Microanal.* **2009**, *15*, 706−707.

[21] Chiu, C.-W.; Hong, P.-D.; Lin, J.-J. Clay-Mediated Synthesis of Silver Nanoparticles Exhibiting Low-Temperature Melting. *Langmuir* **2011**, *27*, 11690−11696.

[22] Ren, J.; Eckert, H. Anion Distribution in Superionic Ag_3PO_4−AgI Glasses Revealed by Dipolar Solid-State NMR. *J. Phys. Chem. C* **2013**, *117*, 24746–24751.

[23] Machida, N.; Nishida, S.; Shigematsu, T.; Sakai, H.; Tatsumisago, M.; Minami, T. Mechano Chemical Synthesis of a Silver Ion Conductor in the System AgI-Ag_3PO_4. *Solid State Ionics* **2000**, *136*, 381−386.

[24] Zhang, S.; Zhang, S.; Song, L. Super-High Activity of Bi^{3+} Doped Ag_3PO_4 and Enhanced Photocatalytic Mechanism. *Appl. Catal., B* **2014**, *152*, 129−139.

[25] Ma, J.; Zou, J.; Li, L.; Yao, C.; Zhang, T.; Li, D. Synthesis and Characterization of Ag_3PO_4 Immobilized in Bentonite for the Sunlight-Driven Degradation of Orange II. *Appl. Catal., B* **2013**, *134*, 1−6.

[26] Farra, R.; Garcia-Melchor, M.; Eichelbaum, M.; Hashagen, M.; Frandsen, W.; Allan, J.; Girgsdies, F.; Szentmiklosi, L.; Lopez, N.; Teschner, D. Promoted Ceria: A Structural, Catalytic, and Computational Study. *ACS Catal.* **2013**, *3*, 2256−2268.

[27] Marrocchelli, D.; Bishop, S. R.; Kilner, J. Chemical Expansion and Its Dependence on the Host Cation Radius. *J Mater. Chem. A* **2013**, *1*, 7673−7680.

[28] Chen, L.; Fleming, P.; Morris, V.; Holmes, J. D.; Morris, M. A. Size-Related Lattice Parameter Changes and Surface Defects in Ceria Nanocrystals. *J. Phys. Chem. C* **2010**, *114*, 12909–12919.

[29] Ma, X.; Lu, B.; Li, D.; Shi, R.; Pan, C.; Zhu, Y. Origin of Photocatalytic Activation of Silver Orthophosphate from First-Principles. *J. Phys. Chem. C* **2011**, *115*, 4680−4687.

[30] Reunchan, P; Umezawa, N. Native Defects and Hydrogen Impurities in Ag_3PO_4. *Phys. Rev B* **2013**, *87*, 245205.

[31] Martin, D. J.; Umezawa, N.; Chen, X.; Ye, J.; Tang, J. Facet Engineered Ag_3PO_4 for Efficient Water Photooxidation. *Energy Environ. Sci.* **2013**, *6*, 3380–3386.

[32] Bi, Y.; Ouyang, S.; Umezawa, N.; Cao, J.; Ye, J. Facet Effect of Single-Crystalline Ag_3PO_4 Sub-Microcrystals on Photocatalytic Properties. *J. Am. Chem. Soc.* **2011**, *133*, 6490−6492.

[33] Tang, C.; Liu, E.; Wan, J.; Hu, X.; Fan, J. Co_3O_4 Nanoparticles Decorated Ag_3PO_4 Tetrapods as an Efficient Visible-Light-Driven Heterojunction Photocatalyst. *Appl. Catal., B* **2016**, *181*, 707−715.

[34] Hsieh, M.-S.; Su, H.-J.; Hsieh, P.-L.; Chiang, Y.-W.; Huang, M. H. Synthesis of Ag_3PO_4 Crystals with Tunable Shapes for Facet-Dependent Optical Property, Photocatalytic Activity, and Electrical Conductivity Examinations. *ACS Appl. Mater. Interfaces* **2017**, *9*, 39086−39093.

[35] Martin, D. J.; Liu, G.; Moniz, S. J. A.; Bi, Y.; Beale, A. M.; Ye, J.; Tang, J. Efficient Visible Driven Photocatalyst, Silver Phosphate: Performance, Understanding and Perspective. *Chem. Soc. Rev.* **2015**, *44*, 7808–7828.

[36] Yogi, P.; Tanwar, M.; Saxena, S. K.; Mishra, S.; Pathak, D. K.; Chaudhary, A.; Sagdeo, P. R.; Kumar, R. Quantifying the Short-Range Order in Amorphous Silicon by Raman Scattering. *Anal. Chem.* **2018**, *90*, 8123–8129.

[37] Kubacka, A.; Si, R.; Michorczyk, P.; Martinez-Arias, A.; Xu, W.; Hanson, J. C.; Rodriguez, J. A.; Fernandez-Garcia, M. Tungsten as an Interface Agent Leading to Highly Active and Stable Copper-Ceria Water Gas Shift Catalyst. *Appl. Catal., B* **2013**, *132*, 423−432.

[38] Botelho, G.; Sczancoski, J. C.; Andres, J.; Gracia, L.; Longo, E. Experimental and Theoretical Study on the Structure, Optical Properties, and Growth of Metallic Silver Nanostructures in Ag_3PO_4. *J. Phys. Chem. C* **2015**, *119*, 6293–6306.

[39] Cao, Q.; Yu, J.; Yuan, K.; Zhong, M.; Delaunay, J.-J. Facile and Large-Area Preparation of Porous Ag_3PO_4 Photoanodes for Enhanced Photoelectrochemical Water Oxidation. *ACS Appl. Mater. Interfaces* **2017**, *9*, 19507−19512.

[40] Rosenburg, F.; Ionescu, E.; Nicoloso, N.; Riedel, R. High-Temperature Raman Spectroscopy of Nano-Crystalline Carbon in Silicon Oxycarbide. *Materials* **2018**, *11*, 93.

[41] Yang, C. C.; Li, S. Size-Dependent Raman Red Shifts of Semiconductor Nanocrystals. *J. Phys. Chem. B* **2008**, *112*, 14193–14197.

[42] Mroczkowska, M.; Nowinski, J. L.; Zukowska, G. Z.; Mroczkowska, A.; Garbarczyk, J. E.; Wasiucionek, M.; Gierlotka, S. Micro Raman, FT-IR/PAS, XRD and SEM Studies on Glassy and Partly Crystalline Silver Phosphate Ionic Conductors. *J. Power Sources* **2007**, *173*, 729–733.

[43] Umezawa, N.; Ouyang, S.; Ye, J. Theoretical Study of High Photocatalytic Performance of Ag_3PO_4. *Phys. Rev. B* **2011**, *83*, 035202.

[44] Liu, J. J.; Fu, X. L.; Chen, S. F.; Zhu, Y. F. Electronic Structure and Optical Properties of Ag_3PO_4 Photocatalyst Calculated by Hybrid Density Functional Method. *Appl. Phys. Lett.* **2011**, *99*, 191903.

[45] Tian, Y.; Tatsuma, T. Mechanisms and Applications of Plasmon-Induced Charge Separation at TiO_2 Films Loaded with Gold Nanoparticles. *J. Am. Chem. Soc*. **2005**, *127*, 7632−7637.

[46] Guan, X.; Guo, L. Cocatalytic Effect of $SrTiO_3$ on Ag_3PO_4 toward Enhanced Photocatalytic Water Oxidation. *ACS Catal.* **2014**, *4*, 3020–3026.

[47] Bi, Y.; Hu, H.; Ouyang, S.; Jiao, Z.; Lu, G.; Ye, J. Selective Growth of Metallic Ag Nanocrystals on Ag_3PO_4 Submicro-Cubes for Photocatalytic Applications. *Chem.-Eur. J.* **2012**, *18*, 14272−14275.

[48] Nakamura, I.; Negishi, N.; Kutsuna, S.; Ihara, T.; Sugihara, S.; Takeuchi, E. Role of Oxygen Vacancy in the Plasma-Treated TiO_2 Photocatalyst with Visible Light Activity for NO Removal. *J. Mol. Catal., A* **2000**, *161*, 205−212.

[49] Tan, H.; Zhao, Z.; Zhu, W.-B.; Coker, E. N.; Li, B.; Zheng, M.; Yu, W.; Fan, H.; Sun, Z. Oxygen Vacancy Enhanced Photocatalytic Activity of Pervoskite $SrTiO_3$. *ACS Appl. Mater. Interfaces* **2014**, *6*, 19184–19190.

[50] Li, Q.; Huang, Z.; Guan, P.; Su, R.; Cao, Q.; Chao, Y.; Shen, W.; Guo, J.; Xu, H.; Che, R. Simultaneous Ni Doping at Atom Scale in Ceria and Assembling into Well-Defined Lotuslike Structure for Enhanced Catalytic Performance. *ACS Appl. Mater. Interfaces* **2017**, *9*, 16243–16251.

[51] Li, C.; Sun, Z.; Song, A.; Dong, X.; Zheng, S.; Dionysiou, D. D. Flowing Nitrogen

Atmosphere Induced Rich Oxygen Vacancies Overspread the Surface of TiO_2/Kaolinite Composite for Enhanced Photocatalytic Activity within Broad Radiation Spectrum. *Appl. Catal., B* **2018**, *236*, 76−87.

[52] Safaei, J.; Ullah, H.; Mohamed, N. A.; Noh, M. F. M.; Soh, M. F.; Tahir, A. A.; Ludin, N. A.; Ibrahim, M. A.; Isahak, W. N. R. W.; Teridi, M. A. M. Enhanced Photoelectrochemical Performance of Z-Scheme g-C_3N_4/$BiVO_4$ Photocatalyst. *Appl. Catal., B* **2018**, *234*, 296−310.

[53] Sivula, K.; Le Formal, F.; Grätzel, M. Solar Water Splitting: Progress Using Hematite (α–Fe_2O_3) Photoelectrodes. *ChemSusChem* **2011**, *4*, 432–449.

[54] Li, W.; Da, P.; Zhang, Y.; Wang, Y.; Lin, X.; Gong, X.; Zheng, G. WO_3 Nanoflakes for Enhanced Photoelectrochemical Conversion. *ACS Nano* **2014**, *8*, 11770−11777.

[55] Wang, Y.; Zhang, Y.-Y.; Tang, J.; Wu, H.; Xu, M.; Peng, Z.; Gong, X.-G.; Zheng, G. Simultaneous Etching and Doping of TiO_2 Nanowire Arrays for Enhanced Photoelectrochemical Performance. *ACS Nano* **2013**, *7*, 9375−9383.

[56] Huang, G; Shi, R; Zhu, Y. Photocatalytic Activity and Photoelectric Performance Enhancement for $ZnWO_4$ by Fluorine Substitution. *J. Mol. Catal., A* **2011**, *348*, 100−105.

[57] Yuan, K.; Cao, Q.; Lu, H.-L.; Zhong, M.; Zheng, X.; Chen, H.-Y.; Wang, T.; Delaunay, J.-J.; Luo, W.; Zhang, L.; Wang, Y.-Y.; Deng, Y.; Ding, S.-J.; Zhang, D. W. Oxygen-Deficient WO_{3-x}@TiO_{2-x} Core–Shell Nanosheets for Efficient Photoelectrochemical Oxidation of Neutral Water Solutions. *J. Mater. Chem. A* **2017**, *5*, 14697−14706.

3. Porous microcrystalline Ag_3PO_4 film photoanodes with improved light absorption and surface area for PEC water oxidation

3.1. Supplementary introduction

Microcrystalline film-based photoelectrodes generally exhibit better stability than nanocrystalline powder-deposited photoelectrodes.[1] Nevertheless, the increase in the particle/crystallite size of the active semiconductor material of the photocatalyst would unfortunately result in the decrease of active surface areas, and consequently reduce the photocurrent densities of the photoelectrodes. Hence in view of this, introducing porous structures into the microcrystalline semiconductor film photoelectrodes seems to be an efficient strategy to realize both improved photoactivity and stability. Recently, porous structures have been demonstrated to be able to improve the PEC performance of the photocathode materials such as NiO,[2] and Cu_2ZnSnS_4,[3] and also a lot of photoanode materials such as α-Fe_2O_3,[4] WO_3,[5] and fluorine-doped rutile TiO_2.[6]

In this chapter, we have prepared large-area (4.5 × 4.5 cm^2) and solution-processed Ag_3PO_4 microcrystalline films with tunable porosity controlled by the reaction time as novel photoanodes for PEC water oxidation. Enhanced PEC water oxidation activity as well as stability were displayed by the Ag_3PO_4 porous films with the optimized porosity obtained for extended reaction times (≥ 20 h), suggesting great potential of these porous Ag_3PO_4 photoanodes to support efficient solar-to-fuel energy conversion and other PEC applications.

3.2. Experimental details

The as-purchased silver foils (99.98%, 0.1 mm thick, Nilaco) were first cut into pieces (4.5×4.5 cm^2) and cleaned by dilute nitric acid solution (Sigma-Aldrich) and acetone (≥ 99.5%, Wako), respectively. Briefly, an aqueous solution was first prepared by mixing 7.2 g of sodium phosphate monobasic (NaH_2PO_4, ≥ 99.0%, Sigma-Aldrich), 103.8 g of hydrogen peroxide (H_2O_2, 30.0−35.5%, Sigma-Aldrich) and 10 g of polyvinylpyrrolidone (PVP, M_W ≈ 55,000, Sigma-Aldrich) in distilled water (380 mL) under stirring at room temperature till the solution became transparent. A piece of Ag foil was then immersed into the mixture solution and kept for different times varied from 1 h to 24 h. Afterwards, the foil was taken out of the solution and rinsed with anhydrous ethanol (≥ 99.5%, Wako) and distilled water thoroughly and dried in air naturally for fabrication into photoanodes.

For materials characterization, the scanning electron microscope (SEM) images were recorded using a field-emission SEM (FE-SEM, S4700, Hitachi, Japan). X-ray diffraction (XRD) data were acquired on a Rigaku Miniflex II-MW (Japan) X-ray diffractometer working with Cu-Kα radiation (1.5406 Å). X-ray photoelectron spectroscopy (XPS) analysis was carried out with a PHI 5000 VersaProbe spectrometer (ULVAC-PHI, Japan) using an Al-Kα X-ray source (1486.6 eV). The electron analyzer was operated at the pass energy of 23.5 eV for the narrow scans. Raman spectra were collected on a laser confocal Raman micro-spectrometer (in*Via* reflex, Renishaw, UK) equipped with an integrated optical microscope (DM-2500, Leica, Germany). The excitation light source of a 632.8 nm He−Ne laser, laser power of 1.7 mW (10% × 17 mW), grating of 1800 1/mm, exposure time of 5.0 s, and accumulation of three times

were applied for all Raman measurements. UV−visible diffuse-reflectance spectra (DRS) were obtained on a JASCO V-670 (Japan) spectrophotometer equipped with an integrating sphere.

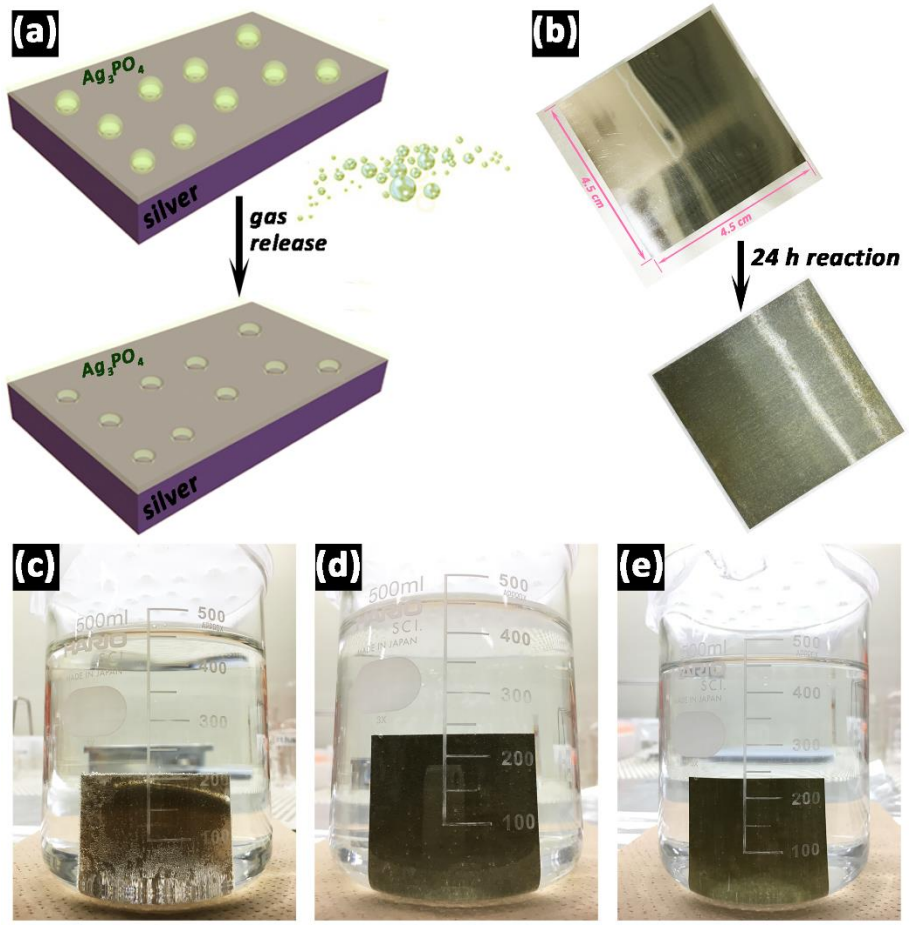

Figure 3.1. (a) Schematic illustration for the gas bubbles release-induced etching into porous structures during the preparation of microcrystalline Ag_3PO_4 films; (b) Digital photography image of the original silver foil substrate (4.5 × 4.5 cm^2) and the finally obtained Ag_3PO_4 film grown on silver after 24 h of the reaction; (c–e) Digital photography images of the chemical reaction phenomena after immersing the silver foil into the mixture solution for 5 min (c), 5 h (d) and 24 h (e), respectively.

For evaluation of the PEC performance, all measurements were carried out in a

three-electrode cell. The as-fabricated Ag_3PO_4 photoanodes, a Pt wire, an Ag/AgCl electrode, and the aqueous solution of Na_3PO_4 (0.02 M, pH ≈ 11.3) were utilized as the working electrode, counter electrode, reference electrode and electrolyte, respectively. Potential of working electrode was controlled with a VersaSTAT-4 potentiostat (Princeton Applied Research). Before each measurement, the electrolyte solution was stirred and purged with high-purity nitrogen gas for above 20 min. During measurements, the Ag_3PO_4 working electrodes were illuminated with a 500 W xenon lamp delivering an irradiance of 285 mW/cm^2. The scan rate was 10 mV/s for collecting each current density−potential (*J*−*E*) curve from negative to positive bias. The electrochemical impedance spectroscopy (EIS) data were acquired using the same electrochemical measurement system under dark conditions at an applied potential of 0.1 V *vs.* Ag/AgCl varying the frequency between 100,000 and 1 Hz of a sinusoidal perturbation with 10 mV amplitude.

3.3. Results and discussion

The Ag_3PO_4 microcrystalline films were grown on silver foil substrates *via* a facile room-temperature and air-exposed solution process without any post-treatment process (*e.g.*, annealing). Figure 3.1 shows a schematic illustration of the origin of the porosity of the Ag_3PO_4 films — induced by the release of H_2 bubbles. Briefly in the reaction, pieces of 4.5 × 4.5 cm^2 Ag substrates were immersed into a mixture solution containing NaH_2PO_4 as the PO_4^{3-} source and H_2O_2 as the oxidation agent. Ag_3PO_4 was then generated on the substrate from the chemical reaction described as follows:

$$2\ NaH_2PO_4 + 2\ H_2O_2 + 6\ Ag \rightarrow 2\ Ag_3PO_4 + 2\ NaOH + 2\ H_2O + H_2\uparrow$$

Figure 3.1c–e show the gas release phenomenon at the time points of 5 min, 5 h as well as 24 h during the reaction. Overall, it can clearly be observed that as the reaction proceeded, a large amount of H_2 bubbles were generated from the reaction and released from the surface of the substrates. Specifically, at the initial stage of the reaction (*i.e.* 5 min), the size of the gas bubbles turned out to be quite large, suggesting that the reaction was rather violent at this time due to the strong oxidation activity of hydrogen peroxide. As the time reached 5 h, the size of the bubbles decreased obviously, making it look more like mist rather than bubbles, indicating that the reaction became milder at this stage owing to the decreased concentration of reactants. Finally, the amount of the mist-like bubbles released from the surface of the substrate decreased when the reaction time reached 24 h as can be understood from the gradual exhaustion of reactants.

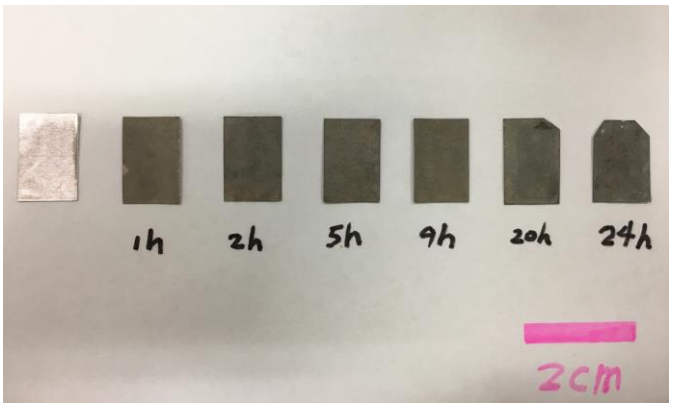

Figure 3.2. Digital micrographs of the Ag_3PO_4 microcrystalline samples obtained with different reaction times on as-purchased silver foils (the most left one). All Ag_3PO_4 samples were 4.5 × 4.5 cm^2 (as shown in Figure 3.1b) and were cut into 1.0 × 1.5 cm^2 to fabricate the photoanodes.

The digital micrographs in Figure 3.1b reveal that after the reaction, the color of as-obtained Ag_3PO_4 films were close to dark yellow, revealing their possibly good

photoactivity when serving as photoelectrodes. The digital micrographs of all samples are shown in Figure 3.2, demonstrating the color change more completely.

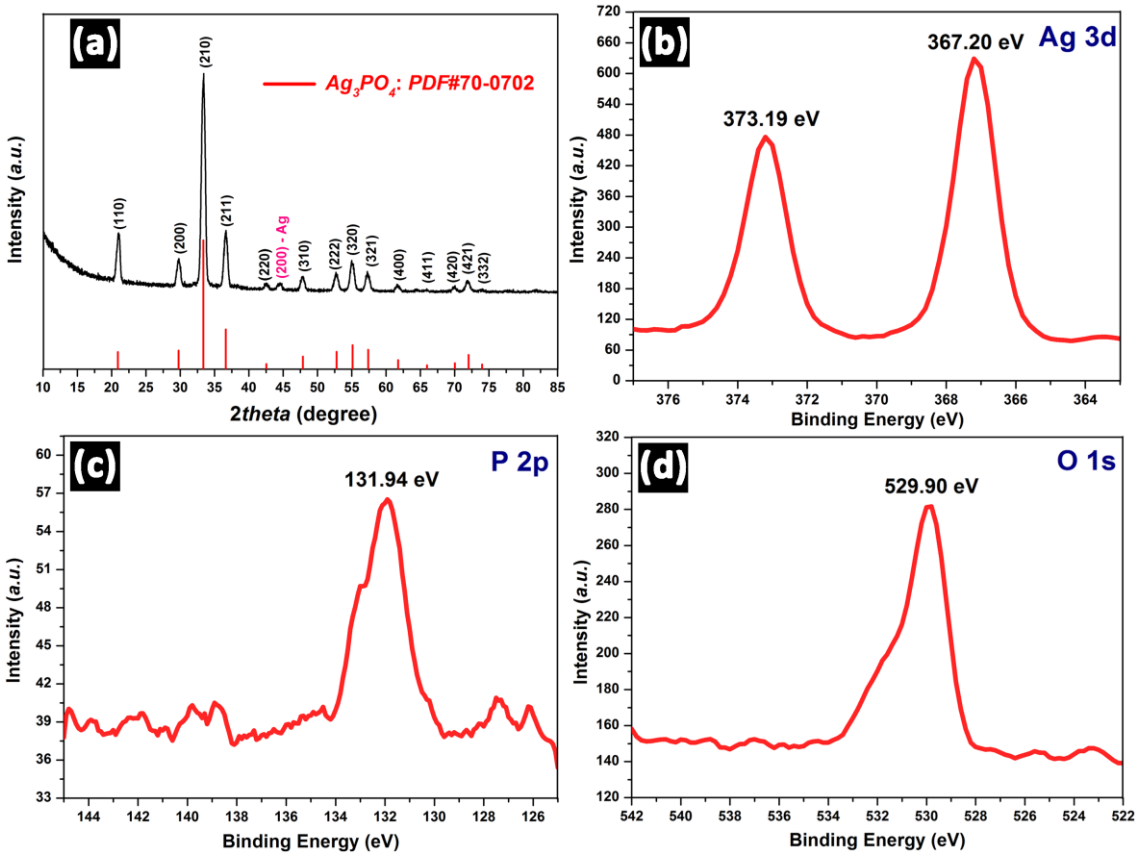

Figure 3.3. Representative (a) XRD pattern and (b–d) XPS spectra of Ag 3d (b), P 2p (c) and O 1s (d) region of the obtained porous microcrystalline Ag_3PO_4 films. The binding energy in panels (b–d) is calibrated by using the contaminant C 1s peak at 284.8 eV as the reference. All data are shown using the 20-h Ag_3PO_4 microcrystalline film sample.

To determine the component and phase purity of the obtained porous films on the silver substrates, the XRD pattern and XPS spectra of the samples were recorded, as exhibited in Figure 3.3. It is clear in Figure 3.3a that except the small diffraction peak at $2\theta \approx 44.3°$ corresponding to the (200) crystal plane of silver (Ag, PDF#04-0783) which should come from the silver substrate, all distinct diffraction peaks could be well

indexed to the cubic *P*(–4)3*n* phase of silver phosphate (Ag_3PO_4, PDF#70-0702). High crystallinity of the obtained photoanode material could be deduced from the distinct shapes and high intensities of the characteristic diffraction peaks in Figure 3.3a. Besides the XRD analysis, XPS narrow scans have also been performed to verify the chemical environment of the different elements. The XPS spectra of Ag 3d, P 2p and O 1s regions are shown in Figure 3.3b–d, and all binding energies have been calibrated by using the contaminant C 1s peak at 284.8 eV as the reference. In Figure 3.3b, the Ag $3d_{3/2}$ and Ag $3d_{5/2}$ peaks could be observed at 373.19 and 367.20 eV of binding energy, respectively, suggesting the presence of Ag^+ in as-synthesized porous microcrystalline films. In Figure 3.3c–d, the peak of P 2p at around 131.94 eV and O 1s at 529.90 eV should be originated from the crystal lattice of P^{5+} and O^{2-} in PO_4^{3-} units according to literature reports.[7–8]

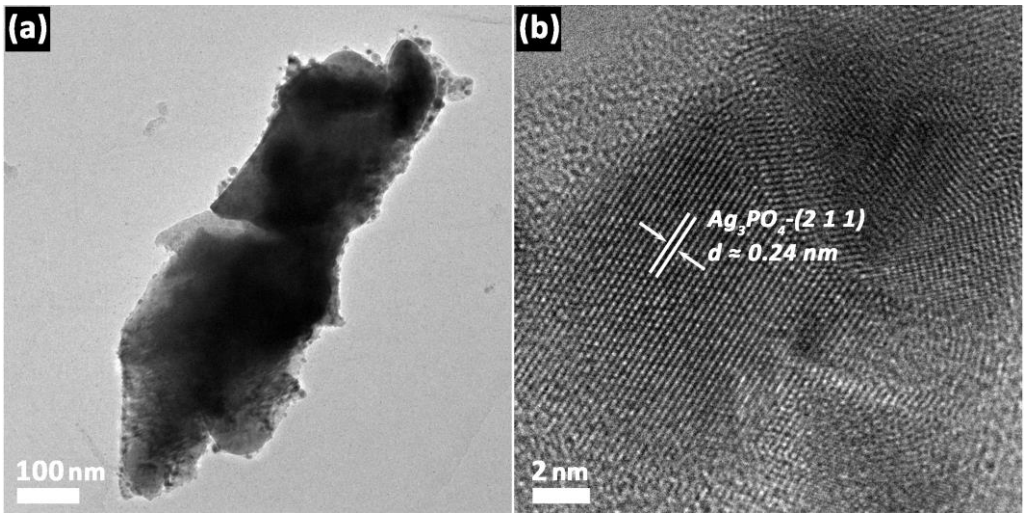

Figure 3.4. (a) TEM and (b) HRTEM images of a fragment obtained from as-prepared 1-h Ag_3PO_4 film by scratching, grinding and sonification. The fine particles in the surroundings [*i.e.* panel (a)] came mainly from the electron beam-induced precipitation of silver nanoparticles, which is a common phenomenon in Ag_3PO_4 nanomaterials.[9]

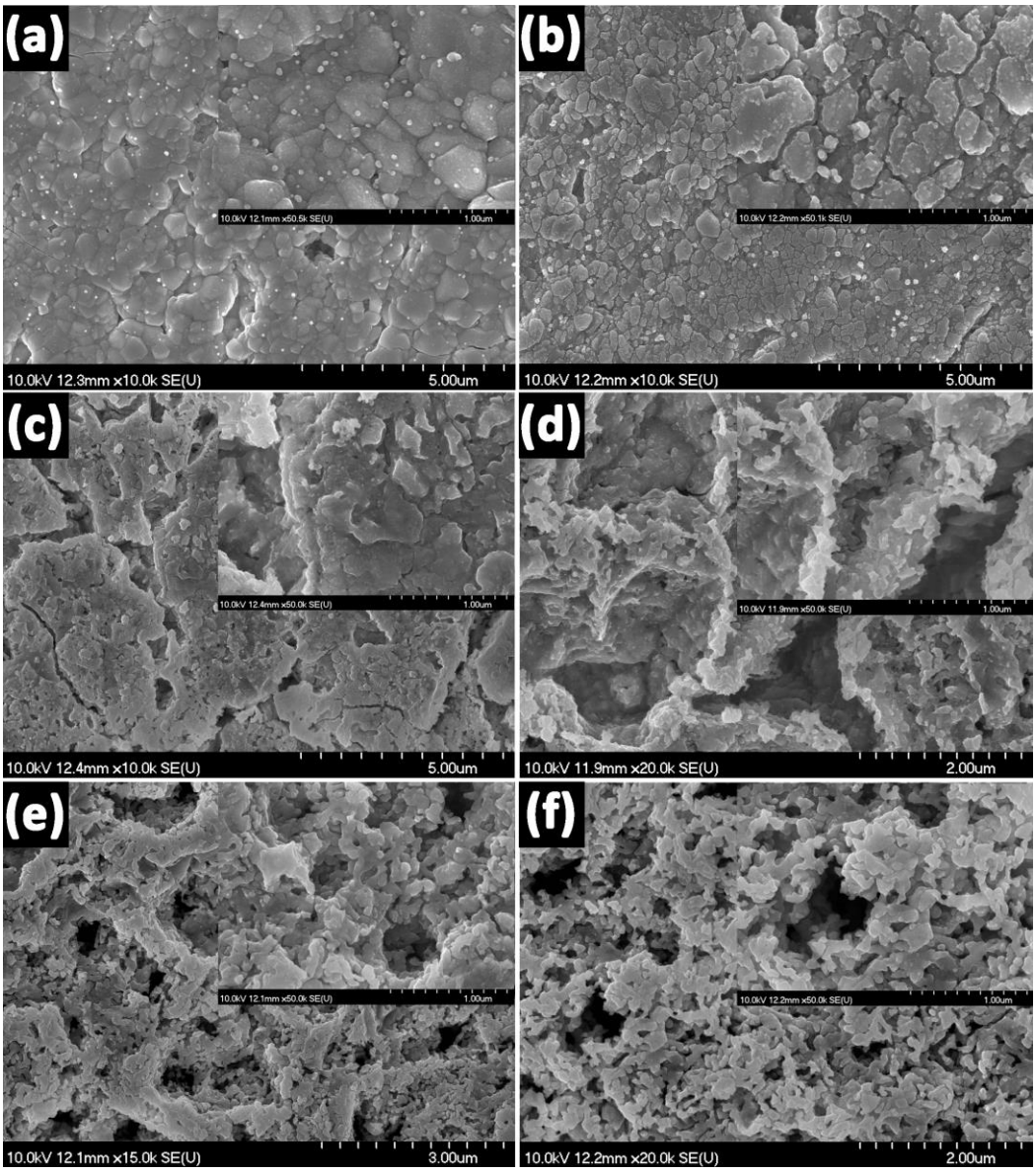

Figure 3.5. SEM images of the obtained porous Ag_3PO_4 photoanodes after (a) 1 h, (b) 2 h, (c) 5 h, (d) 9 h, (e) 20 h and (f) 24 h of the reaction. Inserts in each panel are SEM images recorded at a higher magnification for each sample.

Moreover, the HRTEM image of as-obtained sample, as shown in Figure 3.4b, in which the (211) crystal plane of Ag_3PO_4 could be clearly identified, together with the above-discussed XRD and XPS results, proves that the pure phase Ag_3PO_4 was formed successfully on the silver substrate.

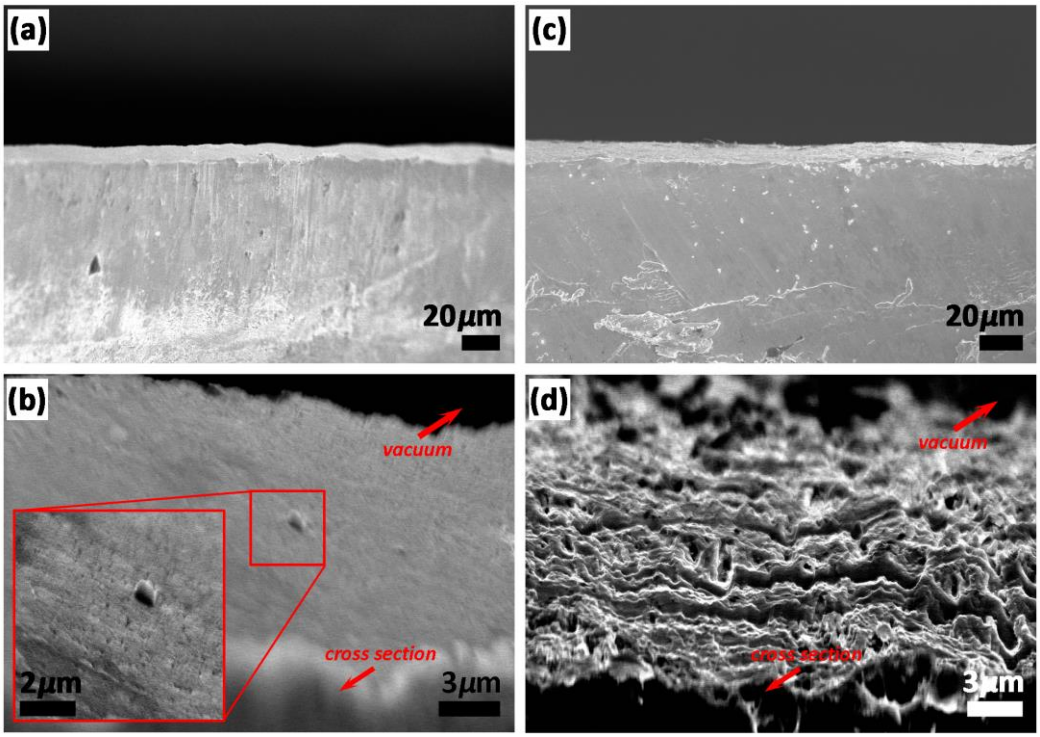

Figure 3.6. Cross-sectional SEM images of the (a−b) nearly non-porous 1-h Ag_3PO_4 microcrystalline film and (c−d) highly porous 20-h Ag_3PO_4 film. The insert in panel (b) shows an enlarged image of the area marked by the red box. The high-resolution SEM images in panels (b) and (d) were both recorded with a 30 °-tilt angle. The thicknesses of the Ag_3PO_4 layers of these two samples are both estimated to be around 10 μm.

The morphologies of the obtained Ag_3PO_4 films on silver substrates are revealed by the SEM images of Figure 3.5 and Figure 3.6. Typically, the appearance of the Ag_3PO_4 film obtained after 1 h of the reaction (Figure 3.5a) looks similar to other previously reported solution-processed semiconductor microcrystalline electrodes like α-Fe_2O_3[10] and Cu_2O[11] with hardly no porous structures on the surface being identified. However, as the reaction proceeded till 2 h long, the surface of Ag_3PO_4 became much rougher. This roughness was ascribed to the etching effect of the H_2 gas bubbles released (Figure 3.5b). Further, when the reaction time was extended to 5 h, 9 h, 20 h and finally 24 h,

distinct interconnected porous structures could clearly be distinguished from the SEM images of the samples (Figure 3.5c−f). The porous structures might be resulted from the continuous formation and release of H_2 bubbles during the chemical reaction generating Ag_3PO_4 from the Ag substrate and PO_4^{3-} in the solution. Cross-sectional SEM images displayed in Figure 3.6 of the nearly non-porous 1-h Ag_3PO_4 film and highly porous 20-h sample further help to confirm the porosity degree of the films. Besides, from the cross-sectional SEM images, it is also found that the thickness of the Ag_3PO_4 film grown on silver foils was almost independent with the reaction time when it was longer than 1 h, as the thicknesses of both the 1-h and 20-h Ag_3PO_4 films were just similar to each other. According to the recorded cross-sectional SEM images shown in Figure 3.6, the nearly non-porous 1-h Ag_3PO_4 microcrystalline film and the highly porous 20-h Ag_3PO_4 film exhibit the similar thickness of ~10 μm. Therefore, it is assumed that when the reaction time was longer than 1 h, the thickness of as-formed Ag3PO4 film would hardly grow, and hence was almost independent with the reaction time. Based on this, it is further assumed that the growing process of Ag_3PO_4 films can be described roughly as the following 2 different stages:

1. The 1st stage ($0 \leq$ reaction time ≤ 1 h): In this stage, because the film was initially quite thin and kept growing thicker gradually, the position where the H_2 bubbles drastically generated was still quite near the top surface of the film. Therefore, these bubbles were likely to be released quickly from the top surface of Ag_3PO_4. Meanwhile, according to our observation, the generated Ag_3PO_4 was not enough to cover everywhere on the silver foil in this stage and there were still a lot of exposed silver surfaces, as illustrated in Figure 3.7b. In this case, the bubbles were more likely to be released from the Ag_3PO_4–Ag foil interfaces on the silver side, and therefore would

have less influence on the formed Ag_3PO_4 film. In addition, the millimeter-sized H_2 bubbles in this stage may be too large to introduce micrometer- or even nanometer-sized pores, as revealed by the SEM images of the porous Ag_3PO_4 photoanodes (Figure 3.5). Therefore, there are almost no pores being observed in the 1-h sample. In fact, it could be seen from Figure 3.7a that if the reaction time was further decreased to 20 min (*i.e.* < 1 h), the produced Ag_3PO_4 microcrystalline film would be more faceted. Nevertheless, these samples are not included and discussed in this chapter since the as-formed Ag_3PO_4 film at this stage could not cover the whole surface of the Ag foil substrate.

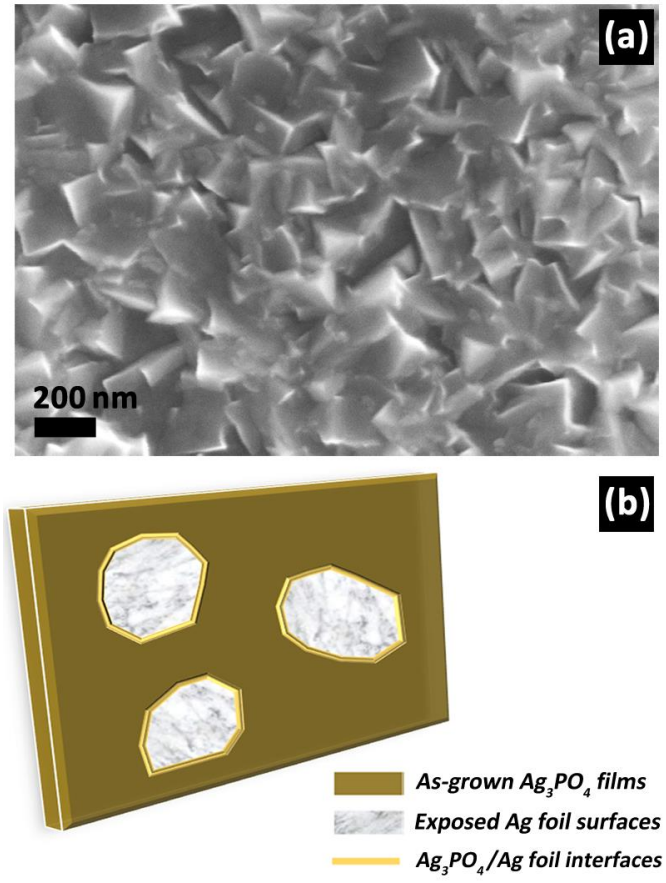

Figure 3.7. (a) SEM image of the obtained Ag_3PO_4 microcrystalline film after 20 min of the reaction; (b) Schematic illustration of the coverage of the generated Ag_3PO_4 film on the silver foil during the first reaction stage ($0 \leq$ the reaction time ≤ 1 h).

2. The 2nd stage (reaction time ≥ 1 h): As the reaction proceeded into this stage, the as-formed Ag_3PO_4 film was already quite thick and had covered the whole silver foil substrate. Meanwhile, the size of the bubbles also decreased as the reaction became milder. In this stage, due to the gradual exhaustion of the reactants, the film thickness might grow only a little. In this situation, the small H_2 bubbles could diffuse slowly from the Ag–Ag_3PO_4 interfaces at the bottom, to the upper surface of the Ag_3PO_4 film, and bring about large numbers of of pores during this process.

The small nanoparticles (*i.e.* brighter white dots) which could be observed in Figure 3.5a–b might be the precipitation of silver from Ag_3PO_4 taking place during the violent chemical reaction at this stage. As the reaction became milder for longer reaction times, the amount of such white dots being observed on the surface seems to decrease, as seen in Figure 3.5c–f. The precipitation of silver nanoparticles did not come from the silver foil substrate which was covered by as-formed thick Ag_3PO_4 film, but was from the decomposition of the Ag_3PO_4 on the surface. It is well known that silver based semiconductors (*e.g.*, Ag_3PO_4 and AgI) are important fast ionic conductors.[12–14] Intrinsically, the ionic mobility of Ag^+ in such materials is fairly higher than the other anions. Particularly in Ag_3PO_4, the ionic mobility of Ag^+ is higher than PO_4^{3-},[15] and the mobility of electrons is higher than holes as well.[16]

In the synthetic experiment, because the amount of the reactants gradually decreased as time went by, it is reasonable that the chemical reaction was more drastic during the initial and early periods than later periods, resulting in the phenomenon that the gas generation and release were also more drastic initially. There were plenty of electrons transferring between silver species and hydrogen species during the redox reaction, and

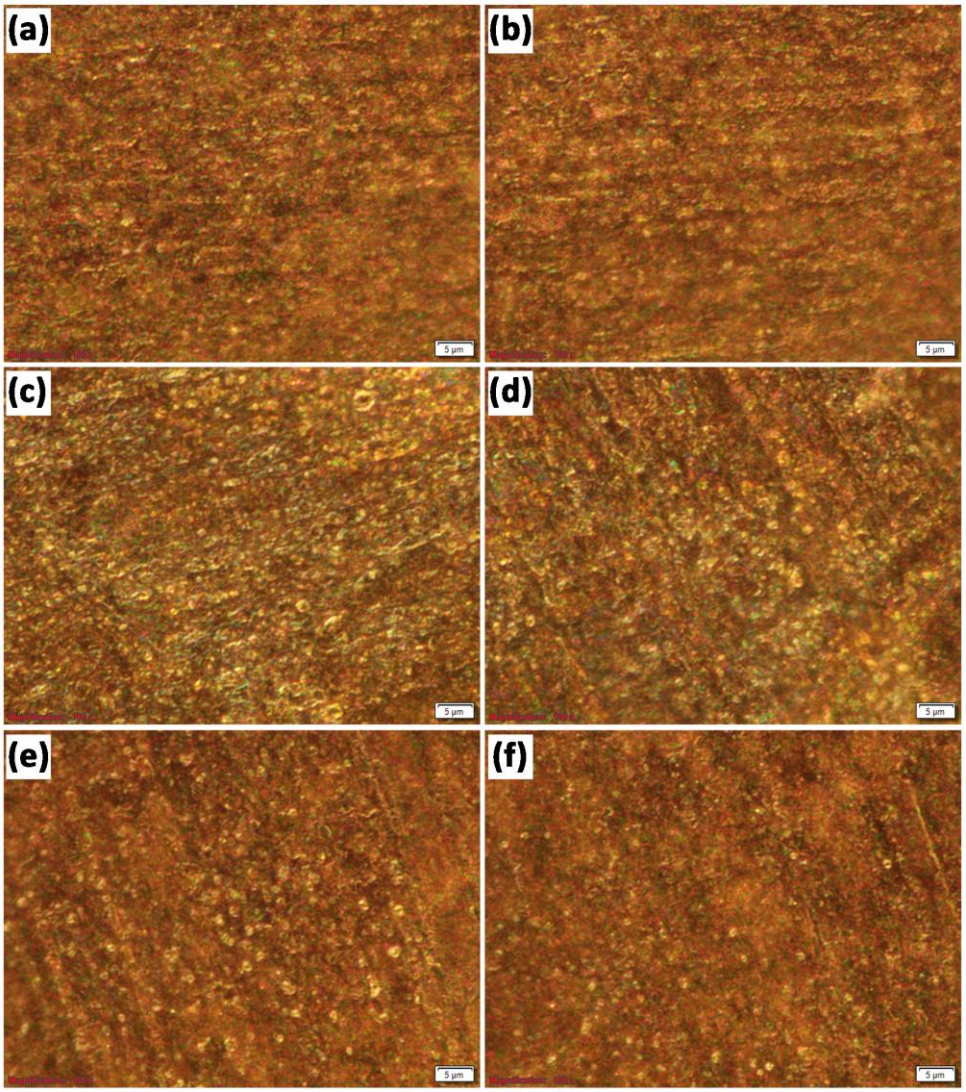

Figure 3.8. Images recorded with an optical scattering (dark field) microscope of the as-synthesized Ag_3PO_4 microcrystalline films with different reaction times varied from (a) 1 h, (b) 2 h, (c) 5 h, (d) 9 h, (e) 20 h, to (f) 24 h.

the dominant reaction was the formation of Ag_3PO_4 solid film and H_2 from NaH_2PO_4, H_2O_2 and Ag, as described in the chemical equation. However, in consideration of the higher ionic mobility of Ag^+ than PO_4^{3-}, and easy transport of electrons in as-formed Ag_3PO_4 solid, it is also rational that in such a high-concentration flow of the electrons during the redox reaction, a part of the Ag^+ in Ag_3PO_4 might be reduced by electrons.

As a result, Ag^0 NPs were precipitated. Afterwards, as the reaction became milder for longer reaction times, the amount of Ag^0 precipitation tended to decrease as well, due to the decrease of the electron flow in Ag_3PO_4 in milder redox reactions. In fact, the reduction of Ag^+ in Ag_3PO_4 by electrons, and consequent precipitation of Ag^0 NPs could be regarded as a common phenomenon in Ag_3PO_4-based materials. The reduction of Ag^+ in Ag_3PO_4 into Ag^0 NPs by the strong electron beam irradiation during the TEM characterization can also be regarded as an indirect evidence, as exhibited in Figure 3.4. This phenomenon of the surface precipitation of Ag^0 NPs on as-prepared Ag_3PO_4 films could also be identified using the dark-field scattering microscopy technique, as shown in Figure 3.8 (*i.e.* white dots in the dark-field images).

In summary, the highly porous structures of the Ag_3PO_4 microcrystalline films obtained with relatively longer reaction times (*i.e.* 9 h, 20 h and 24 h) should have the potential to increase the active surface areas and, hence, enhance the light absorption and subsequent PEC water oxidation activity.

On the other hand, it should also be noted that the generation of such distinct porous structure also depends greatly on the addition of oxidation agent H_2O_2 and surfactant. If H_2O_2 was added drop by drop, no highly porous structures could be formed even after 8 h of the reaction, as revealed in Figure 3.9. This indicates that the initial supersaturation condition which can be realized by adding H_2O_2 once at the same time is necessary for the generation of porous films. Meanwhile, the surfactant of PVP has also played an important role for the generation of high-quality Ag_3PO_4 surfaces. It is clear in Figure 3.10 that PVP of $M_W \approx 40{,}000$, instead of PVP of $M_W \approx 55{,}000$, is not enough to protect the Ag_3PO_4 microcrystals to get defined and clean surfaces.

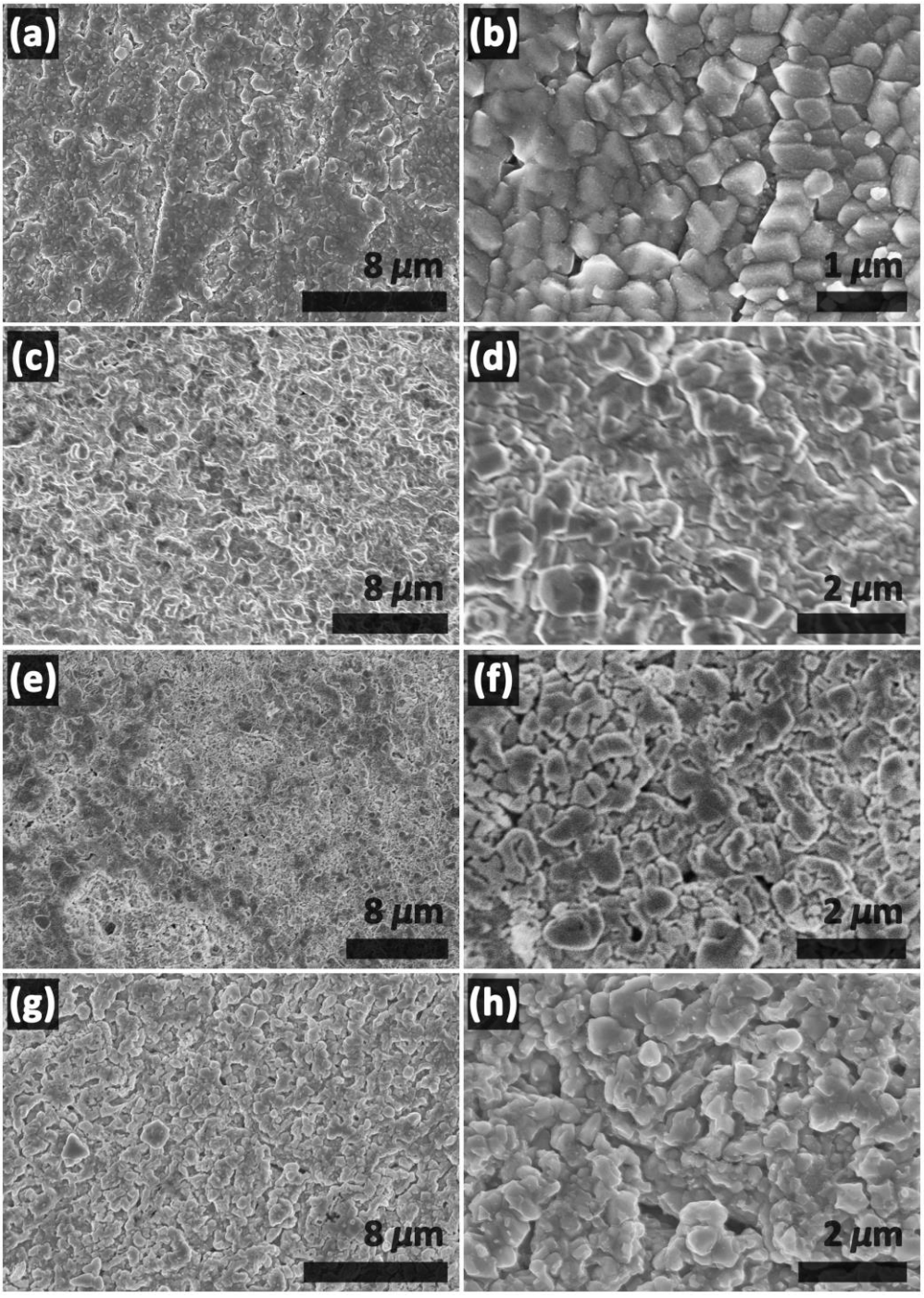

Figure 3.9. SEM images of the Ag_3PO_4 microcrystalline films prepared by adding the oxidation agent H_2O_2 drop by drop, and after the reaction time of (a−b) 1 h, (c−d) 2 h, (e−f) 5 h and (g−h) 8 h, respectively.

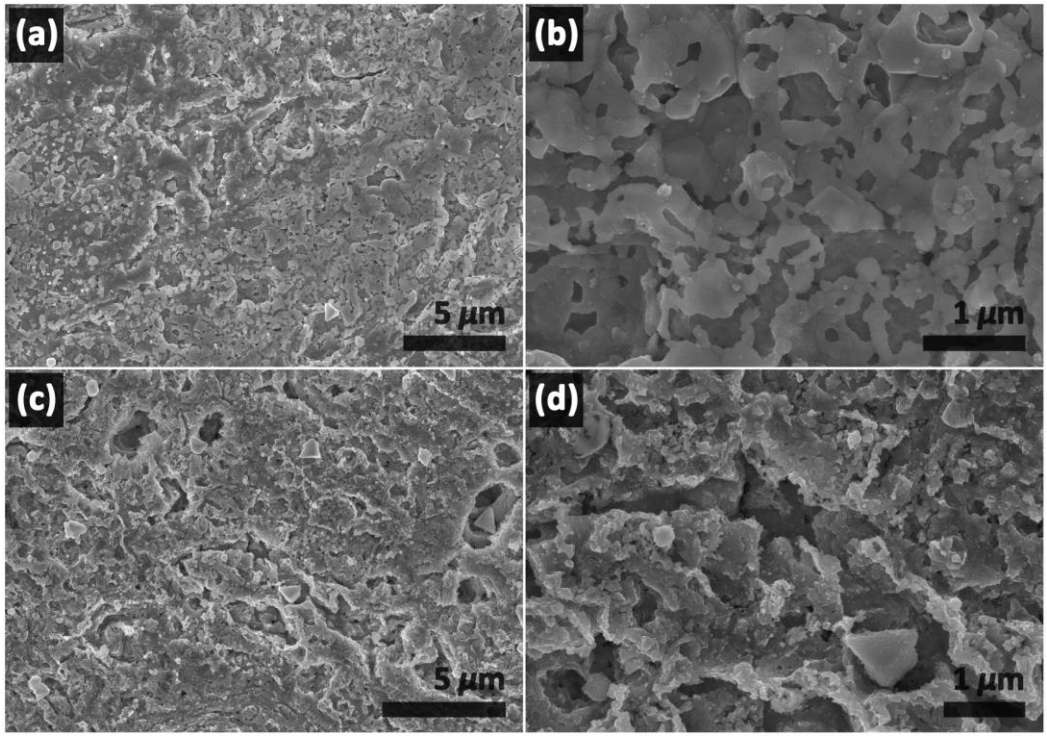

Figure 3.10. SEM images of the Ag_3PO_4 microcrystalline films prepared by utilizing the PVP of $M_W \approx 40{,}000$ as the surfactant, and after the reaction time of (a−b) 2 h and (c−d) 9 h, respectively.

Raman spectra of the samples, as displayed in Figure 3.11, confirm the existence of $[PO_4]$ units and O−P−O bonds in the sample materials. Specifically, seven characteristic Raman scattering peaks could be experimentally identified at the Raman shifts of around 147, 238, 416, 561, 718, 910 and 1003 cm^{-1}. These peak positions could be assigned to the Raman-active vibration modes of rotation and translation of $[PO_4]$ units (147 and 238 cm^{-1}), symmetric bending (416 cm^{-1}) and asymmetric bending (561 cm^{-1}) of $[PO_4]$ units, symmetric stretching (718 and 910 cm^{-1}), and asymmetric stretching (1003 cm^{-1}) of O−P−O bonds, respectively.[9] The observation of multiple resonant Raman peaks indicates that the synthesized Ag_3PO_4 films possessed favorable optical quality.[17] In addition, the slightly increased intensities of the characteristic Raman

peaks of the samples obtained with extended reaction times suggest a gradual improvement of the crystallinity of Ag_3PO_4 as the reaction proceeded.

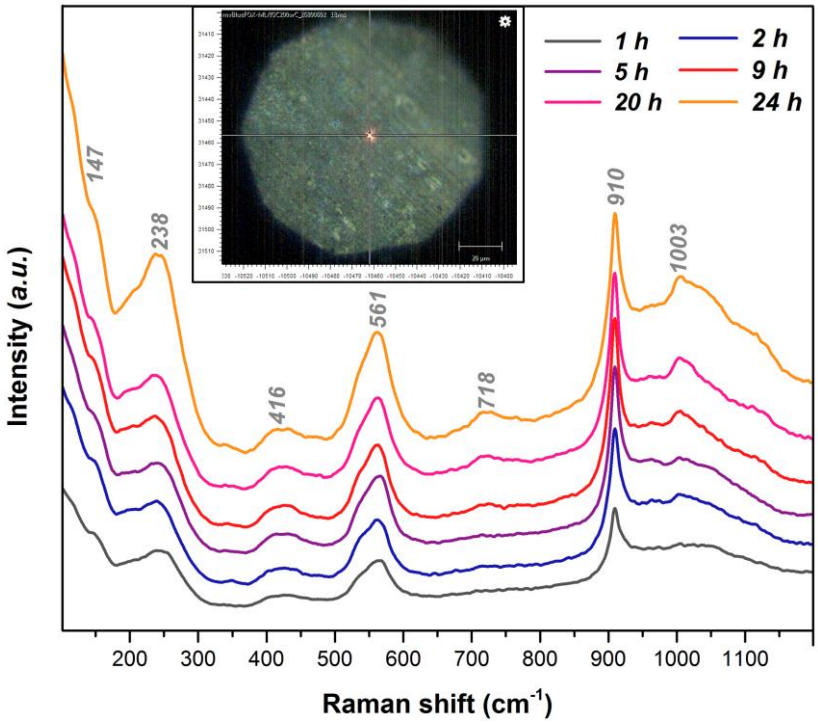

Figure 3.11. Room-temperature Raman spectra of the porous Ag_3PO_4 microcrystalline photoanodes obtained with different reaction times. Insert displays a representative optical micrograph image of the measured area on the Ag_3PO_4 surface during the micro-Raman characterization.

DRS spectra of the obtained Ag_3PO_4 films, as shown in Figure 3.12, indicate that as the extended reaction time brought about promoted porosity, the Ag_3PO_4 films grown on silver substrates demonstrated decreased reflectance and hence increased absorption over the whole ultraviolet–visible light band. This might be attributed to the enhanced light confinement within the interconnected pores of the obtained Ag_3PO_4 films,[18] and consequently lead to improved light capture capability for PEC water splitting. The

absorption edges of all Ag_3PO_4 samples turn out to be close to each other at around 530 nm, which is consistent with the standard value.

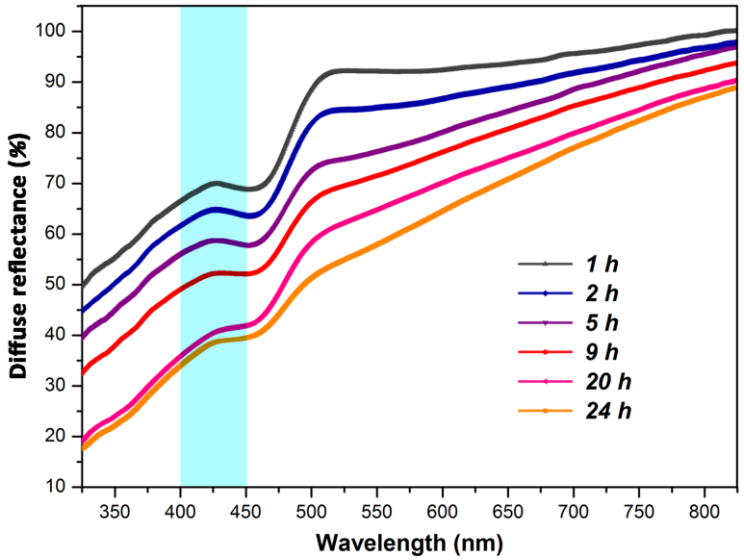

Figure 3.12. UV–visible DRS spectra of the synthesized Ag_3PO_4 microcrystalline films grown on silver substrates with different reaction times.

In addition, a small peak can be seen in the wavelength range of 400−450 nm, as indicated in blue background in Figure 3.12. This small contribution may come from the scattering of precipitated Ag^0 NPs. It seems that as the reaction time increases from 1 h to 24 h, the intensity of this peak decreases slightly. This phenomenon has also been confirmed by the optical scattering microscopy of the Ag_3PO_4 films (Figure 3.8) since the number of the blue–green scattering dots originating from Ag^0 NPs decreases in the samples obtained with longer reaction times. These results imply that when longer reaction times were used, less Ag^0 NPs would be precipitated on the surface of Ag_3PO_4 during the reaction, which is consistent with the SEM observation results (Figure 3.5). The enhanced light absorption of the obtained porous Ag_3PO_4 films together with their intrinsically high photoactivity suggest the potential of the porous films as highly

efficient photoanodes for PEC water oxidation.

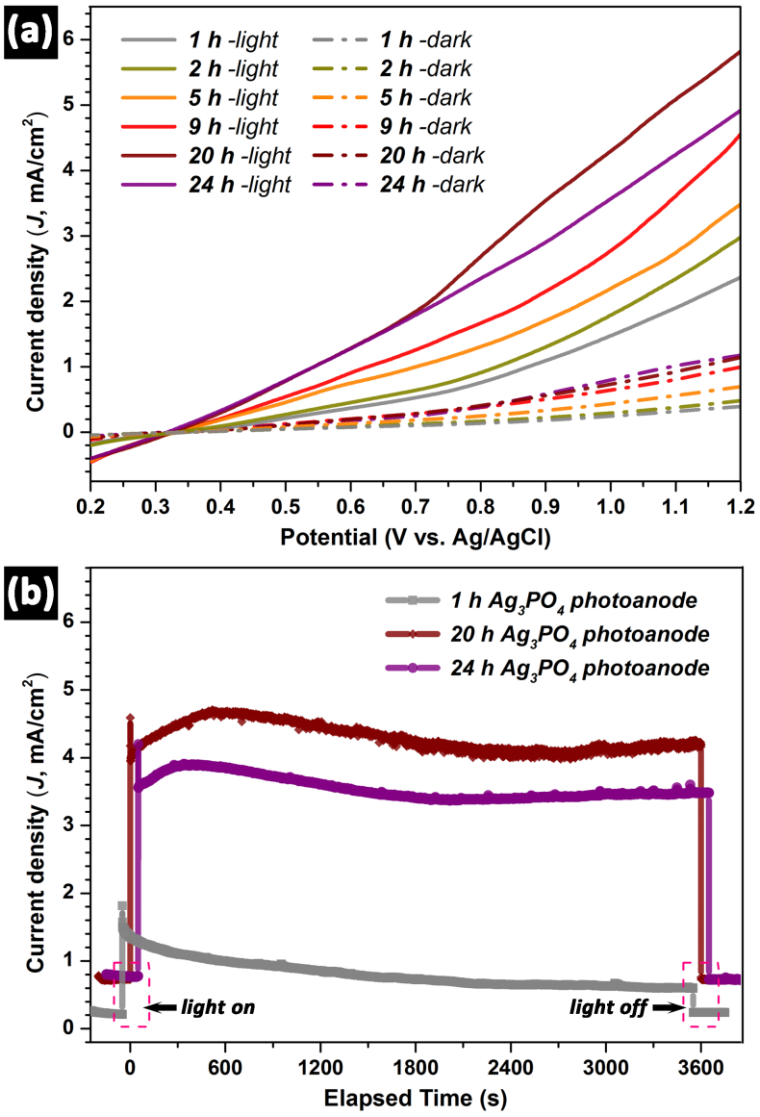

Figure 3.13. PEC water oxidation performance of the obtained Ag_3PO_4 photoanodes: (a) LSV curves of all the photoanodes fabricated using Ag_3PO_4 films obtained at different reaction times. The solid lines and dashed lines stand for the photocurrent densities and dark current densities, respectively; (b) Current density−time (*J*–*t*) curves of the porous Ag_3PO_4 photoanodes fabricated using 1 h, 20 h and 24 h reaction times recorded during 1-h continuous PEC water splitting tests at an applied potential of 1.0 V *vs.* Ag/AgCl.

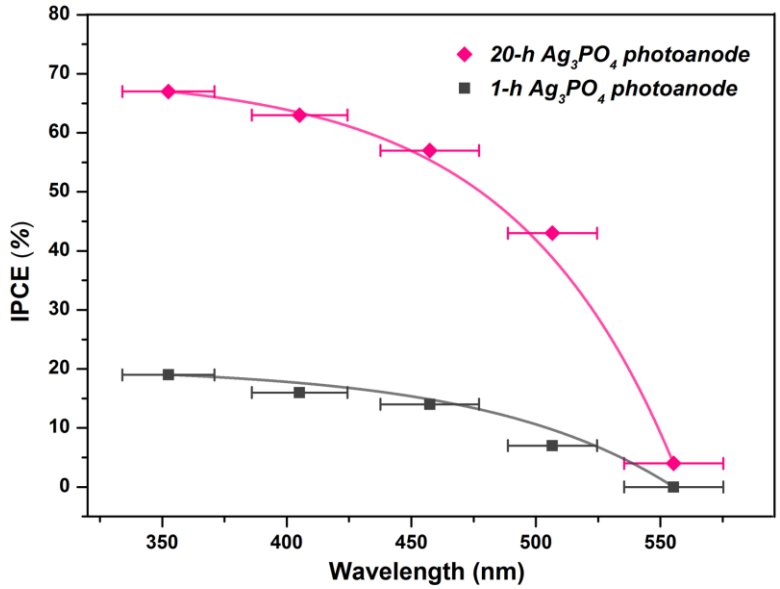

Figure 3.14. Monochromatic incident photon-to-electron conversion efficiency (IPCE) profiles of the obtained nearly non-porous 1-h Ag_3PO_4 photoanode and highly porous 20-h Ag_3PO_4 photoanode measured at 1 V *vs.* Ag/AgCl.

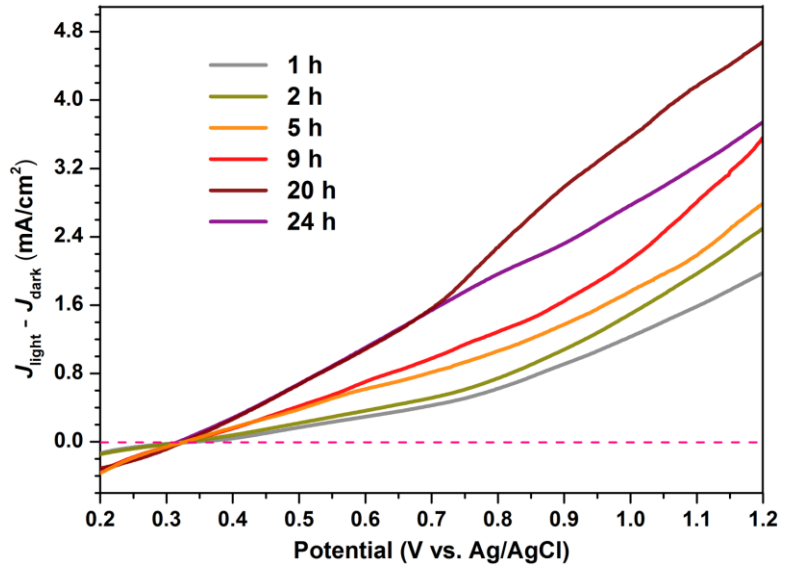

Figure 3.15. The dependence of $J_{light} - J_{dark}$ (*i.e.* photocurrent density – dark current density) on the applied bias for all the porous Ag_3PO_4 microcrystalline photoanodes obtained after different reaction times. These curves are derived from Figure 3.13a.

Figure 3.13a displays the applied bias-dependent photocurrent densities of all the fabricated Ag_3PO_4 photoanodes together with the dark current densities. It is clear that as the reaction time increased from 1 h to 20 h, the photocurrent densities of the Ag_3PO_4 photoanodes increased. The 20-h Ag_3PO_4 photoanodes presented a photocurrent density of about 4.32 mA/cm^2 at 1 V *vs.* Ag/AgCl, which is almost three times higher than that of the 1-h Ag_3PO_4 photoanode (1.48 mA/cm^2). This enhancement could be attributed to the boosted active surface areas and also light capture ability of the highly porous samples than non-porous samples. The higher incident photon-to-electron conversion efficiency (IPCE) profiles of the 20-h Ag_3PO_4 photoanode than 1-h Ag_3PO_4 photoanode, as shown in Figure 3.14, suggest the higher external quantum efficiencies (EQEs) of the porous photoanodes than non-porous ones, which have made contributions to the higher photocurrent densities in Figure 3.13a. As has been discussed before, the decrease in the amount of Ag^0 NPs on the surface of Ag_3PO_4 as the reaction time increased may also have a positive effect on the photocurrent density. The Ag^0 NPs at Ag_3PO_4/electrolyte interfaces could easily attract photoelectrons due to their superior electron affinity and serve as the recombination centers for the photogenerated electron/hole pairs and, therefore, lead to the loss of photoholes entering water oxidation reaction.

It could be observed from Figure 3.13a that the dark current densities of Ag_3PO_4 photoanodes also increased gradually together with the photocurrent densities. This phenomenon suggests that Ag_3PO_4 also have electrocatalytic activity. Therefore, the dependences of $J_{light} - J_{dark}$ values (*i.e.* photocurrent density minus dark current density) on the applied bias for all the Ag_3PO_4 photoanodes have been calculated to verify the contribution of photocatalytic activity in the as-recorded photocurrent densities. Figure 3.15 shows that the $J_{light} - J_{dark}$ values of different Ag_3PO_4 photoanodes give the same

trend as that of Figure 3.13a, thus confirming that photocatalytic effect has indeed played a dominant role in generating the photocurrent. The slight decrease in the photocurrent density from the 20-h to 24-h Ag_3PO_4 photoanodes might be originated from the increased interfacial charge transfer impedance between Ag_3PO_4 surfaces and the electrolyte solution. This effect is evidenced by the EIS Nyquist plots exhibited in Figure 3.16. On one hand, the relatively low interfacial charge transfer resistance (R_{CT}) and thus high conductivity of all these Ag_3PO_4 photoanodes could be regarded as one reason for the high current densities observed in Figure 3.13a. On the other hand, the increased interfacial R_{CT} derived from the increased porosity induced an increase in the density of non-conductive voids in the Ag_3PO_4 films obtained with longer reaction time might have resulted in the decreased photocurrent density from the 20-h to 24-h Ag_3PO_4 porous photoanodes.

Besides the high photocurrent density, it is notable that the porous Ag_3PO_4 photoanodes obtained with prolonged reaction times ($\geq$ 20 h) also demonstrated better stability than non-porous ones, which could be known clearly from a 1-h successive PEC water splitting test carried out at 1 V *vs.* Ag/AgCl (Figure 3.13b). The promotion in stability of the porous Ag_3PO_4 photoanodes may be caused by the pores inside the Ag_3PO_4 layer because the porous structures could help to release the stress at the near-surface region so that could help to keep them more stable than non-porous Ag_3PO_4 according to previous reports.[19–21] SEM images of the 1-h and 20-h Ag_3PO_4 photoanodes after experiencing the 1-h PEC water splitting tests, shown in Figure 3.17, clearly confirm that the continuous water oxidation reaction on the surface of the 1-h photoanode has caused a strong surface erosion of the originally non-porous Ag_3PO_4 film (Figure 3.17a–b), leading to a non-negligible loss of active materials and decrease

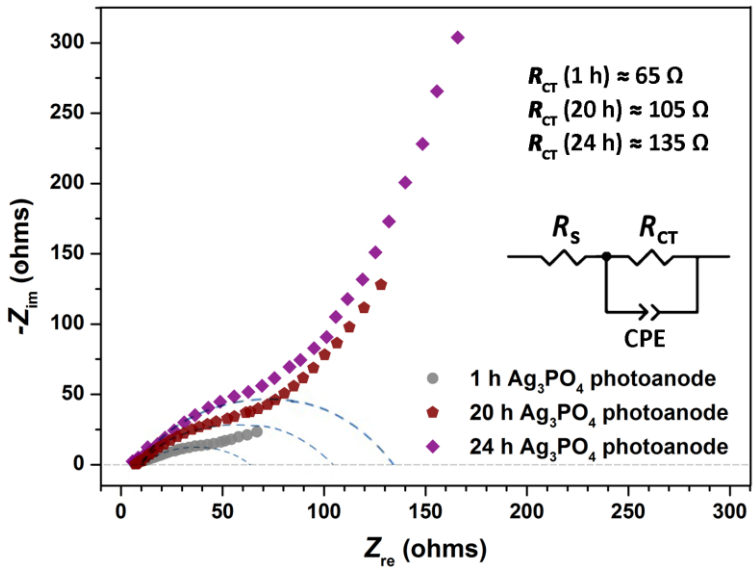

Figure 3.16. Nyquist plots of electrochemical impedance spectroscopy (EIS) recorded under dark conditions of the fabricated 1-h, 20-h and 24-h Ag_3PO_4 microcrystalline photoanodes. The insert shows the equivalent circuit which consists of a serial resistor (R_S) and a resistor–capacitor circuit. The resistor–capacitor circuit models the parallel combination of the interfacial charge transfer resistance (R_{CT}) and the constant phase element (CPE), attributed to the interface between the surface of photoanode and the electrolyte.

of the photocurrent density. However, the highly porous structure of the 20-h Ag_3PO_4 photoanode (Figure 3.17c–d), on the contrary, remained essentially the same after the 1-h stability test, ensuring the maintenance of the high photocurrent density. The 20-h porous Ag_3PO_4 photoanode, moreover, displayed considerable stability even when the stability test was further extended to 5 h, with its surface morphology, phase purity, and chemical surface state maintaining essentially unchanged (Figure 3.18). The Faradaic efficiencies of the 5-h successive water splitting reaction using the 20-h porous Ag_3PO_4 film as the photoanode are all calculated to be ~100% based on the H_2 evolution amount

detected using a gas chromatography (GC) setup (Figure 3.19), which further confirm the stability of the 20-h porous Ag_3PO_4 photoanode in relatively long-time reactions.

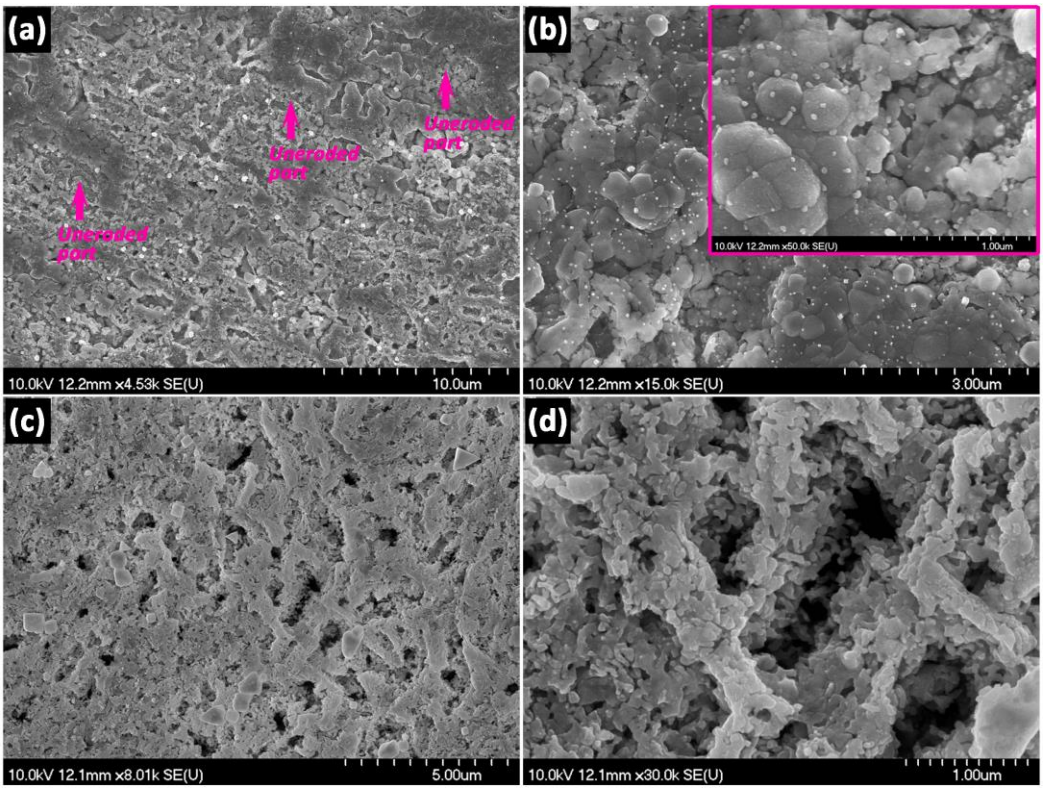

Figure 3.17. Top-view SEM images for the (a–b) 1-h as well as the (c–d) 20-h Ag_3PO_4 photoanodes after experiencing 1-h continuous PEC water splitting tests at an applied bias of 1.0 V *vs.* Ag/AgCl. The insert in panel (b) shows an enlarged view of the surface of the 1-h Ag_3PO_4 sample after the stability test.

Regarding the curve shape in Figure 3.13b, it can be known that the photocurrent densities of both the 20-h and 24-h Ag_3PO_4 porous microcrystalline film photoanodes first increase and then decrease during the stability test (*i.e.* the brown and purple curves). Possibly, there are two reasons which might have resulted in this slight increase at first:

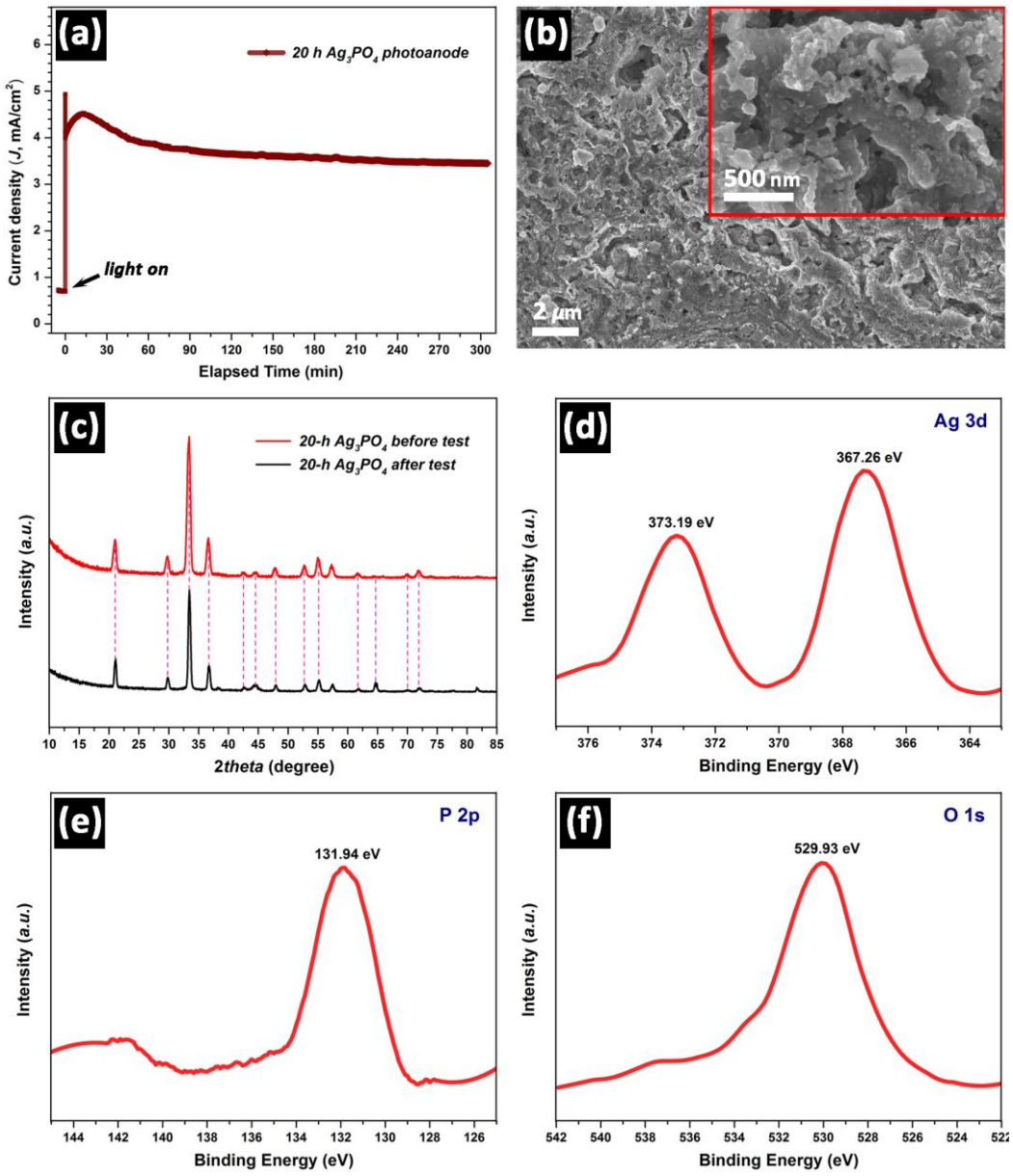

Figure 3.18. (a) Current density−time (*J*−*t*) curve recorded in the 5-h successive PEC water splitting test using the 20-h porous Ag_3PO_4 photoanode at 1.0 V *vs.* Ag/AgCl, and representative SEM image (b), XRD pattern (c), and XPS spectra of Ag 3d (d), P 2p (e) and O 1s (f) region of the 20-h Ag_3PO_4 photoanode after the 5-h stability test. The binding energy in panels (d–f) is calibrated by using the contaminant C 1s peak at 284.8 eV as the reference.

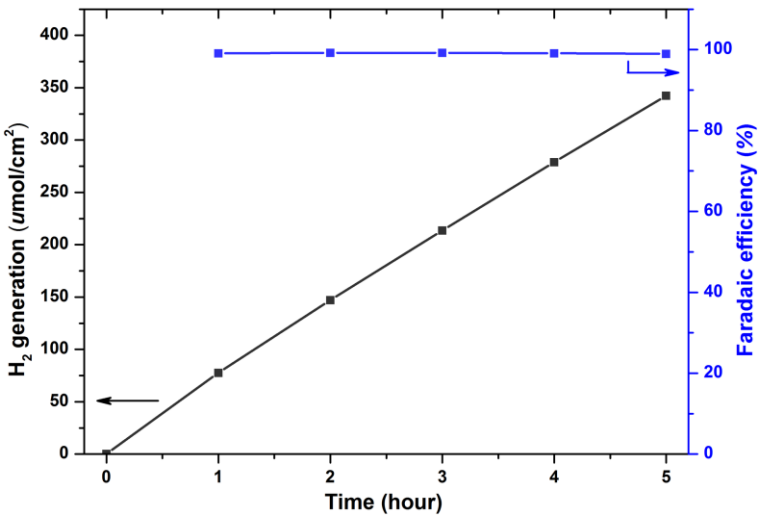

Figure 3.19. Gas chromatography collection of the H_2 gas generated during the 5-h successive stability test (Figure 3.18a) using the 20-h porous Ag_3PO_4 microcrystalline photoanode at an applied bias of 1.0 V *vs.* Ag/AgCl, and the correspondingly calculated Faradaic efficiencies.

1. This increase in partial photocurrent density might be caused by photoexcitation and photoactivation of the porous Ag_3PO_4 photoanodes and the subsequent participation of photoexcited holes in the anodic water oxidation reaction at the interface.[22]

2. Considering that Ag_3PO_4 is an *n*-type semiconductor with both a direct bandgap of ~2.43 eV and an indirect bandgap of ~2.36 eV, it is possible that the indirect bandgap excitation of Ag_3PO_4 may have caused non-negligible thermal effect induced by the lattice vibration. As a result, the slight increase of the local temperature at the surface of the photoanode might also have brought about the promotion in catalytic activity, and thus the photocurrent density.

However, in the case of the nearly non-porous 1-h Ag_3PO_4 photoanode, in spite of these favorable effects, the non-negligible loss of active materials revealed by the SEM

images (Figure 3.17a–b) has still played a dominant role in causing the decrease in the photocurrent density, and thus no increase in the photocurrent density could be observed (*i.e.* the gray curve in Figure 3.13b). Overall, the high photocurrent density as well as improved stability manifested by the 20-h Ag_3PO_4 photoanodes suggest great potential for highly efficient PEC energy conversion.

3.4. Conclusions

In this chapter, we prepared large-area (4.5 × 4.5 cm^2) and solution-processed Ag_3PO_4 microcrystalline films with tunable porosity controlled by the reaction time as novel photoanodes for PEC water splitting. Enhanced light absorption was demonstrated for the microcrystalline Ag_3PO_4 films with an optimized porosity obtained for a prolonged reaction time (≥ 20 h). This enhanced light absorption results in improved water oxidation performance of the Ag_3PO_4–based photoanodes. Particularly, the highly porous 20-h Ag_3PO_4 photoanode presented a photocurrent density of around 4.32 mA/cm^2 at 1.0 V *vs.* Ag/AgCl, which is nearly three times higher than that of the non-porous 1-h Ag_3PO_4 photoanode (1.48 mA/cm^2). In addition, superior stability of the 20-h porous Ag_3PO_4 photoanode was revealed by the 1-h successive PEC water splitting experiment. Based on these results, it is believed these porous Ag_3PO_4 microcrystalline photoanodes hold great potential to support efficient solar-to-fuel energy conversion and many other PEC applications.

References

[1] Li, C.; Hisatomi, T.; Watanabe, O.; Nakabayashi, M.; Shibata, N.; Domen, K.; Delaunay, J.-J. Positive Onset Potential and Stability of Cu_2O-Based Photocathodes in Water Splitting by Atomic Layer Deposition of a Ga_2O_3 Buffer Layer. *Energy Environ. Sci.* **2015**, *8*, 1493–1500.

[2] Hu, C. Y.; Chu, K.; Zhao, Y. H.; Teoh, W. Y. Efficient Photoelectrochemical Water Splitting over Anodized *p*-Type NiO Porous Films. *ACS Appl. Mater. Interfaces* **2014**, *6*, 18558−18568.

[3] Wen, X.; Luo, W. J.; Zou, Z. G. Photocurrent Improvement in Nanocrystalline Cu_2ZnSnS_4 Photocathodes by Introducing Porous Structures. *J. Mater. Chem. A* **2013**, *1*, 15479−15485.

[4] Brillet, J.; Grätzel, M.; Sivula, K. Decoupling Feature Size and Functionality in Solution-Processed, Porous Hematite Electrodes for Solar Water Splitting. *Nano Lett.* **2010**, *10*, 4155–4160.

[5] Liu, Y.; Zhao, L.; Su, J. Z.; Li, M. T.; Guo, L. J. Fabrication and Properties of a Branched $(NH_4)_xWO_3$ Nanowire Array Film and a Porous WO_3 Nanorod Array Film. *ACS Appl. Mater. Interfaces* **2015**, *7*, 3532−3538.

[6] Fang, W. Q.; Huo, Z. Y.; Liu, P. R.; Wang, X. L.; Zhang, M.; Jia, Y.; Zhang, H. M.; Zhao, H. J.; Yang, H. G.; Yao, X. D. Fluorine-Doped Porous Single-Crystal Rutile TiO_2 Nanorods for Enhancing Photoelectrochemical Water Splitting. *Chem.-Eur. J.* **2014**, *20*, 11439−11444.

[7] Zhang, S.; Zhang, S.; Song, L. Super-High Activity of Bi^{3+} Doped Ag_3PO_4 and Enhanced Photocatalytic Mechanism. *Appl. Catal., B* **2014**, *152*, 129−139.

[8] Ma, J.; Zou, J.; Li, L.; Yao, C.; Zhang, T.; Li, D. Synthesis and Characterization of Ag_3PO_4 Immobilized in Bentonite for the Sunlight-Driven Degradation of Orange II. *Appl. Catal., B* **2013**, *134*, 1−6.

[9] Botelho, G.; Sczancoski, J. C.; Andres, J.; Gracia, L.; Longo, E. Experimental and Theoretical Study on the Structure, Optical Properties, and Growth of Metallic Silver Nanostructures in Ag_3PO_4. *J. Phys. Chem. C* **2015**, *119*, 6293–6306.

[10] Sivula, K.; Formal, F. L.; Grätzel, M. Solar Water Splitting: Progress Using Hematite (α-Fe_2O_3) Photoelectrodes. *ChemSusChem* **2011**, *4*, 432−449.

[11] Paracchino, A.; Mathews, N.; Hisatomi, T.; Stefik, M.; Tilley, S. D.; Grätzel, M. Ultrathin Films on Copper(I) Oxide Water Splitting Photocathodes: A Study on Performance and Stability. *Energy Environ. Sci.* **2012**, *5*, 8673–8681.

[12] Makiura, R.; Yonemura, T.; Yamada, T.; Yamauchi, M.; Ikeda, R.; Kitagawa, H.; Kato, K.; Takata, M. Size-Controlled Stabilization of the Superionic Phase to Room Temperature in Polymer-Coated AgI Nanoparticles. *Nat. Mater.* **2009**, *8*, 476–480.

[13] Ren, J.; Eckert, H. Anion Distribution in Superionic Ag_3PO_4−AgI Glasses Revealed by Dipolar Solid-State NMR. *J. Phys. Chem. C* **2013**, *117*, 24746–24751.

[14] Zhang, H.; Tsuchiya, T.; Lang, C.; Terabe, K. Size-Controlled AgI/Ag Heteronanowires in Highly Ordered Alumina Membranes: Superionic Phase Stabilization and Conductivity. *Nano Lett.* **2015**, *15*, 5161–5167.

[15] Yu, H.; Jiao, Z.; Jin, B.; Feng, C.; Lu, G.; Bi, Y. Facile Synthesis of Porous Ag_3PO_4 Photocatalysts with High Self-Stability and Activity. *RSC Adv.* **2016**, *6*, 56166–56169.

[16] Ma, X.; Lu, B.; Li, D.; Shi, R.; Pan, C.; Zhu, Y. Origin of Photocatalytic Activation of Silver Orthophosphate from First-Principles. *J. Phys. Chem. C* **2011**, *115*, 4680−4687.

[17] Cao, Q.; Che, R. Tailoring Au–Ag–S Composite Microstructures in One-Pot for Both

SERS Detection and Photocatalytic Degradation of Plasticizers DEHA and DEHP. *ACS Appl. Mater. Interfaces* **2014**, *6*, 7020−7027.

[18] Cao, Q.; Liu, X.; Yuan, K.; Yu, J.; Liu, Q.; Delaunay, J.-J.; Che, R. Gold Nanoparticles Decorated Ag(Cl,Br) Micro-necklaces for Efficient and Stable SERS Detection and Visible-Light Photocatalytic Degradation of Sudan I. *Appl. Catal., B* **2017**, *201*, 607−616.

[19] Cheng, H.-E.; Chen, C. C. Morphological and Photoelectrochemical Properties of ALD TiO_2 Films. *J. Electrochem. Soc.* **2008**, *155*, D604−D607.

[20] Dang, H. X.; Lin, Y.-M.; Klavetter, K. C.; Cell, T. H.; Heller, A.; Mullins, C. B. Lithium Insertion/Deinsertion Characteristics of Nanostructured Amorphous Tantalum Oxide Thin Films. *ChemElectroChem* **2014**, *1*, 158−164.

[21] Lim, W. F.; Quah, H. J.; Hassan, Z.; Radzali, R.; Zainal, N.; Yam, F. K. Porous Quaternary $Al_{0.1}In_{0.1}Ga_{0.8}N$ Film Formation *via* Photoelectrochemical Etching in HF:C_2H_5OH Electrolyte. *J. Am. Ceram. Soc.* **2016**, *99*, 2395−2401.

[22] Roy, N.; Hirano, Y.; Kuriyama, H.; Sudhagar, P.; Suzuki, N.; Katsumata, K.-I.; Nakata, K.; Kondo, T.; Yuasa, M.; Serizawa, I.; Takayama, T.; Kudo, A.; Fujishima, A.; Terashima, C. Boron-Doped Diamond Semiconductor Electrodes: Efficient Photoelectrochemical CO_2 Reduction through Surface Modification. *Sci. Rep.* **2016**, *6*, 38010.

4. Overall summaries

In this thesis, solution-processed large-area (4.5 × 4.5 cm^2) Ag_3PO_4 microcrystalline films are first prepared *via* a room-temperature, air-exposed immersion reaction. The multiple effects of the native defects in Ag_3PO_4, *i.e.* V_{Ag}, Ag_i, and surface precipitation of Ag^0 NPs, are first demonstrated experimentally. By varying the addition amount of the oxidation agent H_2O_2 during the synthetic reaction, Ag_3PO_4 microcrystalline films with different amounts of Ag^0 NPs on the surface are obtained. It is found that despite the favorable superior conductivity and plasmonic effect having improved the interfacial charge transfer and light absorption of the Ag_3PO_4 film photoanode, the defective film with the largest amount of Ag^0 NPs on the surface finally exhibits the lowest current density, due to the disadvantageous effects involving the decreased crystalline quality, easier decomposition of active material of Ag_3PO_4, decreased electrochemical surface area with Ag^0 NPs on the surface serving as the recombination centers. As a result, even the Ag_3PO_4 microcrystalline film having achieved the highest photocurrent density fails to demonstrate considerable stability. These results further highlight the significance of fundamentally reducing the native defects of Ag_3PO_4 towards enhanced water oxidation stability and efficiency of the microcrystalline film photoanodes.

Typically, the post-treatment of vacuum annealing at different temperatures (*i.e.* 100, 200, 300, 400 and 500 °C) has been investigated as a strategy for solving the problem of native defects and low light absorption of Ag_3PO_4. It is found that below 400 ºC is the |Recovery| stage for Ag_3PO_4 microcrystals when defect amount decreases and therefore crystallinity increases. From 400 ºC, the |Recrystallization| stage and also precipitation of Ag_3PO_4 bulk crystals start, and afterwards till 500 ºC is the |Recrystallization + Grain

growth| stage for Ag_3PO_4, when more faceted and larger bulk crystals of Ag_3PO_4 precipitate extensively. In this series of Ag_3PO_4 film photoanodes, the same variation in [$J_{light} - J_{dark}$] *vs. E* curves are found as the light absorption profiles, *i.e.* 400 ºC > 500 ºC > 300 ºC > 200 ºC > non-annealed > 100 ºC-annealed Ag_3PO_4 film, indicating that light absorption, especially the bandgap absorption could be the dominant factor to the PEC performance. Particularly, much improved PEC water oxidation stability and efficiency of the 400 ºC-annealed Ag_3PO_4 film photoanode are demonstrated compared with the non-annealed Ag_3PO_4 film, suggesting that the methodology of vacuum annealing could be utilized for improving the PEC performance of Ag_3PO_4 film photoanodes because of its ability to reduce the native defects like V_{Ag}, remove the Ag^0 NPs on the surface, and increase the bandgap light absorption of these Ag_3PO_4 microcrystalline films.

Next, from the viewpoint of advanced structural design, in consideration that the usage of microcrystalline film photoanode may cause the problem of decreased active surface area despite its relatively higher stability than nanocrystalline powder-deposited photoanode, the possibility of introducing porous structures into these microcrystalline Ag_3PO_4 film photoanodes is also investigated towards further improved photoactivity and stability. Particularly, it is demonstrated that the porous degree of the as-obtained Ag_3PO_4 films could be tuned by changing the reaction time from 1 h to 2 h, 5 h, 9 h, 20 h and 24 h, with the usage of specific reaction parameters. These porous Ag_3PO_4 films, in spite of leaving the native defects not recovered and Ag^0 NPs on the surface not removed, finally could demonstrate improved surface areas and light absorption, owing to which improved PEC performance has also been achieved. Particularly, the optimized highly porous 20-h Ag_3PO_4 microcrystalline film photoanode shows superior water oxidation efficiency with a photocurrent density of 4.32 mA/cm^2 which is almost three

times higher than that of non-porous 1-h film (1.48 mA/cm^2) at 1.0 V *vs.* Ag/AgCl, and is also higher than the 400 °C-annealed non-porous film photoanode.

Overall, it could be concluded that: a) The instability of the Ag_3PO_4 microcrystalline films is originated from the native defects involving V_{Ag} and Ag^0 NPs precipitated on the surface, thus the methodology of vacuum annealing, typically at 400 °C, turns out to be more favorable for improved stability because it can fundamentally solve, or at least mitigate the various problems induced by native defects; b) Light absorption is a crucial factor to the PEC performance, whereas the surface area which largely determines the final process of PEC water oxidation – surface redox reaction is also important, thus the porous Ag_3PO_4 microcrystalline film photoanodes can achieve higher efficiency in spite of leaving the defect and absorption issues not solved; c) Trying to make a combination of these two techniques, *i.e.* taking both the fundamental properties of the material (*e.g.*, defects and absorption) and the advanced structural design (*e.g.*, larger surface area) into concern, may provide further possibility towards more stable and efficient Ag_3PO_4 film photoanodes for PEC water oxidation.

List of publications

[1] C. Li[†], **Q. Cao**[†], F. Wang[†], Y. Xiao, Y. Li, J.-J. Delaunay[*], H. Zhu, Engineering graphene and TMDs based van der Waals heterostructures for photovoltaic and photoelectrochemical solar energy conversion, ***Chem. Soc. Rev.***, 2018, vol. 47, 4981−5037. ([†] co-first author) [Impact factor = 40.18]

[2] **Q. Cao**, J. Yu, K. Yuan, M. Zhong, J.-J. Delaunay[*], Facile and large-area preparation of porous Ag_3PO_4 photoanodes for enhanced photoelectrochemical water oxidation, ***ACS Appl. Mater. Interfaces***, 2017, vol. 9, 19507−19512. [Impact factor = 8.10]

[3] **Q. Cao**, X. Liu, K. Yuan, J. Yu, Q. Liu, J.-J. Delaunay, R. Che, Gold nanoparticles decorated Ag(Cl,Br) micro-necklaces for efficient and stable SERS detection and visible-light photocatalytic degradation of Sudan I, ***Appl. Catal. B – Environ.***, 2017, vol. 201, 607−616. [Impact factor = 11.70]

[4] **Q. Cao**, K. Yuan, J. Yu, J.-J. Delaunay, R. Che, Ultrafast self-assembly of silver nanostructures on carbon-coated copper grids for surface-enhanced Raman scattering detection of trace melamine, ***J. Colloid Interf. Sci.***, 2017, vol. 490, 23−28. [Impact factor = 5.09]

[5] K. Yuan[†], **Q. Cao**[†], H.-L. Lu, M. Zhong, X. Zheng, H.-Y. Chen, T. Wang, J.-J. Delaunay, W. Luo, L. Zhang, Y.-Y. Zhang, Y. Deng, S.-J. Ding, D. W. Zhang, Oxygen-deficient WO_{3-x}@TiO_{2-x} core-shell nanosheets for efficient photoelectrochemical oxidation of neutral water solutions, ***J. Mater. Chem. A***, 2017, vol. 5, 14697−14706. ([†] co-first author) [Impact factor = 9.93]

[6] J. Yu, **Q. Cao**, B. Feng, C. Li, J. Liu, J. K. Clark, J.-J. Delaunay[*], Insights into the efficiency and stability of Cu-based nanowires for electrocatalytic oxygen evolution, ***Nano***

Res., 2018, vol. 11, 4323–4332. [Impact factor = 7.99]

[7] M. H. Mirfasih, C. Li, A. Tayyebi, **Q. Cao**, J. Yu, J.-J. Delaunay*, Oxygen-vacancy induced photoelectrochemical water oxidation by platelike tungsten oxide photoanodes prepared under acid-mediated hydrothermal treatment conditions, ***RSC Adv.***, 2017, vol. 7, 26992−27000. [Impact factor = 2.94]

[8] **Q. Cao**, J.-J. Delaunay*, *et al*, Unusual effects of vacuum annealing boosting light absorption and water oxidation stability of novel microcrystalline Ag_3PO_4 film photoanodes, 2018, *to be submitted*.

[9] **Q. Cao**, J.-J. Delaunay*, *et al*, Modulating surface precipitation of silver nanoparticles on Ag_3PO_4 microcrystalline films towards improved photoelectrochemical water oxidation, 2018, *to be submitted*.

[10] **Q. Cao**, J.-J. Delaunay*, *et al*, Direct nanoimprinting of a submicron-hole array onto microcrystalline Ag_3PO_4 film photoanode for enhanced visible-light water oxidation, 2018, *in preparation*.

[11] J. Yu, **Q. Cao**, J.-J. Delaunay*, *et al*, Defect-rich $NiCeO_x$ electrocatalyst with ultrahigh stability and low overpotential for water oxidation, 2018, *submitted* to ***ACS Catalysis***.